A STUDY ON THE HADROPRODUCTION OF HEAVY RESONANCES IN ATLAS EXPERIMENT AT THE LHC

EUROPEAN PH. D. THESIS

Presented by **Juan Luis Domenech-Garret**

Depto. de Física Atómica Molecular y Nuclear

Universidad de Valencia

May 10-th, 2001

Agradecimientos

Llegados ya al fin de este trabajo, es de recibo (y un placer) el reconocimiento a las personas que, de una manera u otra, han contribuído a que estas hojas, inicialmente blancas, se hayan llenado.

En primer lugar a Miguel Angel Sanchis Lozano, que consintió en su día en dirigirme esta tesis: gracias por su amistad y los buenos ratos que hemos pasado. Por haberme contagiado su entusiasmo por el tema de las resonancias pesadas y sus múltiples aplicaciones fenomenológicas. Por haber refinado en mi persona la prudencia científica y por enseñarme el recomendable arte del "provando e riprovando", que día a día hemos puesto en práctica. Por su paciencia; por esa científica amplitud de miras con la que ha escuchado todas mis reflexiones (las más y las menos acertadas), por la cantidad de horas pasadas revisando el texto y haciendo su inglés mas inteligible, y por la ingente cantidad de cosas relacionadas con este apasionante tema que me ha enseñado.

Mi co-directora de tesis Victoria Castillo Giménez, que ya en su día me dirigió la tesina: por su ayuda e interés, por haber seguido este trabajo, por las horas de corrección, y por haber demostrado ser una amiga.

Al Departamento de Física Atómica, Molecular y Nuclear y al grupo TICAL de Valencia, especialmente a Emilio Higón y Antonio Ferrer por haberme financiado los viajes y demás veleidades relacionadas con esta tesis; y por su amistad.

A Juano Valls, por haberme facilitado el acceso a los datos del “RUNIb” de CDF, y sus consejos referentes a PYTHIA. A Paco Camarena por habernos ayudado a conseguir los datos de eficiencias del detector ATLAS. A Javier Sanchez y Amparo Lacruz por ayudarme a solventar mil y un problemas informáticos. A Amparo y Enrique, de la secretaría del departamento y a las secretarias del IFIC por ayudarme a salir de los laberintos administrativos.

Al B-physics Working Group de la colaboración ATLAS, especialmente S. Baranov, P. Eerola, N. Ellis, y M. Smizanska por su interés, comentarios y sugerencias. Aparte, tambien agradecerles, por idénticos motivos, a M. Kraemer, F. Maltoni, y Y. Tsipolitis.

A mis amigo/as de la facultad y de fuera de ella, cuya lista de nombres ocuparía un espacio desmesurado, además sería redundante (y en algunos casos irreverente), mencionarlos aquí, puesto que ellos ya saben quienes son. Gracias a ellos por todos los buenos ratos que hemos pasado en desayunos, almuerzos, comidas, meriendas, cenas, ágapes, francachelas, tertulias y eventos de muy variopinta naturaleza y calado. Aprovecho la ocasión para desearles a todos una feliz existencia.

A todos los que haya olvidado mencionar y merecieran de alguna forma figurar en esta lista.

Por último, mi familia: no cabe decir mucho, porque es evidente todo lo que tengo que agradecerles; mis tias, mis hermanos, y mis padres.

Contents

Introducción

Este Trabajo está dedicado al estudio de la hadroproducción de resonancias pesadas (RP) y otras cuestiones físicas relacionadas con ellas tales como el estudio de la Cromodinámica Cuántica, tanto en sus aspectos perturbativo y no perturbativo. Desde el descubrimiento de de las partículas J/ψ por Aubert, Ting et al. (1974), y Υ por Innes et al. (1977), se ha desatado en este campo una considerable actividad, tanto experimental como teórica, que aún continua. El estudio de las RP implica un sinfín de desafios para los físicos que han ido proponiendo soluciones a medida que se han presentado, como por ejemplo: La identificación y clasificación de los diferentes miembros de las familias charmonio y botomonio; la solución del problema del déficit teórico de las tasas de producción de RP respecto de las experimentales, etc. Actualmente una de las principales cuestiones en liza es la polarización del J/ψ, cuyo mecanismo aún no está del todo comprendido. Además está el problema del tratamiento teórico de la parte no perturbativa en los procesos de producción y aniquilación, y otras cuestiones que entroncan directamente con los fundamentos de la Cromodinámica Cuántica (denotada con el acrónimo inglés QCD).

En la última década la hadroproducción de RP ha suscitado mucha atención con la explicación de la discrepancia entre el llamado modelo singlete de color (CSM, en inglés) y los datos experimentales, suponiendo esta diferencia alrededor de un factor 50 para la hadroproducción directa de J/ψ en Tevatrón. Como solución se introdujo el llamado mecanismo octete de color (COM, en inglés). Este mecanismo puede considerarse una generalización (relativista) del CSM, e intoduce de una manera natural la explicación del inesperado superávit de RP. No obstante al aplicar el COM a otros mecanismos de producción, como la fotoproducción en HERA, se han levantado dudas iniciales acerca de la validez de este modelo, aunque ultimamente se han realizado muchos progresos para una mejor comprensión del problema. Además, los resultados recopilados en Tevatrón sobre la polarización de J/ψ (siendo ésta transversal una de las principales predicciones del COM) parecen indicar fallos de una aplicación demasiado "ingenua" de los mecanismos de produción de color para charmonio [1]. Para dilucidar la cuestión, que puede calificarse de confusa en el presente, son precisos pues, test de RP más restrictivos.

En el presente trabajo, debido a la vastedad del área que cubre la hadroproducción de RP, hemos preferido centrarnos únicamente en el estudio de la familia $\Upsilon(nS)$ $(n = 1, 2, 3)$, por debajo del umbral de la produccion abierta de bottom, debido al interés que actualmente suscita. Básicamente lo que se ha hecho es analizar algunas cuestiones relevantes en la mencionada familia, usando un generador de sucesos Monte Carlo llamado PYTHIA, introduciendo aquellos cambios oportunos (en la menor medida posible) en el programa original, con el fin de adaptarlo a nuestros propósitos, es decir, una mejor reproducción de la física del Υ.

Por otra parte es preciso decir que este estudio se mantendrá dentro del llamado "nivel de partícula" (*particle level*), esto es, ocupándose únicamente de los procesos físicos de las partículas sin considerar los ulteriores efectos de detección; aunque en algunas partes, por necesidad, se harán estimaciones de dichos efectos. La razón es, de nuevo, la extensión del campo cubierto, permaneciendo a este nivel de partícula. La cantidad adicional de análisis que supone considerar los efectos de detector, es suficiente para justificar por si mismo otro trabajo de igual longitud a éste. Por lo tanto, hemos decido posponer este objetivo para futuros estudios.

La Tesis comienza con un capítulo dedicado a algunas cuestiones experimentales suscitadas al considerar la hadroproducción de RP. Aquí se resalta el papel esencial que un complejo detector del futuro LHC (ATLAS), debido a sus singulares características, puede desempeñar, usándose éste en solitario o conjuntamente con otros detectores de LHC. Así pues se empieza con una descripción del detector ATLAS; después se discute acerca de algunos aspectos experimentales de la producción de botomonio (Υ's). El capítulo termina con una exposición de la física de "jets" en este detector y sus implicaciones en nuestra posterior propuesta para la medida de la densidad de gluones en el protón usando la hadroproducción de Υ:

Aunque el acelerador LHC tiene como principal objetivo la búsqueda y el estudio de física mas allá del llamado Modelo Estándar, las altas tasas esperadas de producción del quark bottom lo hace especialmente interesante para el previsto programa sobre física del B en el proyecto LHC. De hecho hay previsto un experimento específico (*LHCb*) para esta clase de física, además se dispondrá de otros experimentos de propósito general (ATLAS y CMS), que cuentan con periodos especialmente dedicados a esta física.

Entre la física de sabores pesados, la producción de quarkonio pesado (es decir, las RP) ha desempeñado un papel histórico en el desarrollo y prueba de la QCD como la mejor candidata para la descripcción de la dinámica de la interacción fuerte, y posiblemente continua mantiniendo esa posición sobresaliente en esta tarea.

El capítulo 2 tiene como principal fin revisar algunos aspectos teóricos de la producción de botomonio, empezando con una descripción del quarkonio pesado desde el punto de vista del modelo quark. Después se hace un breve repaso a los modelos de produccion de RP más relevantes, como el CSM, el modelo de evaporación de color, y -especialmente- el COM; aquí se destacan aspectos importantes de esos modelos que luego tendrán su reflejo en este trabajo. Debido a la importancia que el COM tendrá, aquí anticiparemos que este mecanismo de producción esta basado en la formación de un estado coloreado (no observable) intermedio durante la interacción partónica, evolucionando de forma no perturbativa hacia una RP física en el estado final, de acuerdo a ciertas probabilidades gobernadas por la llamada QCD no relativista (NRQCD).

El capítulo 3 está dedicado a la exposición de las principales técnicas empleadas en este estudio, asi como una descripcción de las modificaciones y nuevas incorporaciones en el programa original de PYTHIA: fuentes de producción de las RP, discusión de los parámetros a escoger, inclusión de los efectos de orden superior de QCD como: la radiación inicial, incorporación de los efectos de la evolución Altarelli-Parisi del gluón que se fragmenta dando lugar a la resonancia en la simulación montecarlo, etc. Después se describe la inclusión del COM en el programa original de PYTHIA. Para acabar el capítulo, se explican los procedimientos para el ajuste de los elementos de matriz de NRQCD y algunos detalles adicionales. En resumen, todo el bagaje necesario para el análisis de la hadroproducción de la resonancias $\Upsilon(nS)$.

El capítulo 4 esta centrado en el análisis de la información disponible sobre hadroproducción de Υ. Este estudio está basado en los datos tomados en la serie "Run IB" de la colaboración CDF de Tevatrón en Fermilab. Esto supone un significativo aumento de la estadística respecto a los anteriores datos del "Run IA" de la misma colaboración. Primero, sirviéndonos de éstos, analizamos las secciones eficaces diferenciales, extrayendo de ahí los elementos de matriz de NRQCD más importantes, ocupándonos del problema de la factorización de la seción eficaz. Después analizamos las fuentes de producción directa de $\Upsilon(1S)$ contrastándolas con las obtenidas experimentalmente; también nos ocupamos de los valores de las secciones eficaces totales, de $\Upsilon(nS)$, etc.

En el capítulo 5 mostramos predicciones sobre la hadroproducción de bottomonia a las futuras energías y condiciones del LHC, considerando sus características más importantes. Para hacer esas predicciones, extrapolamos la información obtenida en el capítulo anterior a partir de los resultados de Tevatrón: valores esperados de las secciones eficaces diferenciales e integradas para todas las resonancias $\Upsilon(nS)$, además de cocientes de secciones eficaces. No obstante, éstas no son las únicas predicciones sobre LHC que se hacen:

En el capítulo 6 presentamos una propuesta para medir la densidad de gluones en el protón, usando la hadroproducción de Υ en el marco del modelo octete de color (COM). La determinación experimental de estas densidades es actualmente uno de los grandes objetivos para comprender mejor la física de los hadrones. Aparte de la propuesta en sí, se aportan detalles adicionales para su puesta en marcha y cuestiones que van surgiendo con el propio desarrollo.

Es preciso añadir, que nuestra propuesta debe contemplarse junto con otros métodos de estudio de las distribuciones de gluones en hadrones como aquellos basados en sucesos con dos jets (di-jet), producción de pares de leptones y producción de fotones "tempranos" (prompt). También hay que dejar bien sentado que esta propuesta descansa en la dominancia de un mecanismo de producción en la zona de alto p_T (el de COM), que predice una producción esencialmente a través de la fragmentación de gluones. A pesar de que nuestra propuesta está sustentada sobre ésta y de otras hipótesis (como la validez de la factorización de la sección eficaz), creemos que las colaboraciones de LHC deben mantener una mente abierta a esta posibilidad. En esta propuesta radica el por qué de las predicciones de las secciones eficaces de producción que se hacen en el capítulo precedente (y también en éste), pues es preciso asegurarse que la cantidad de botomonio producido sea suficiente para permitir la medida de dicha densidad de gluones.

Para acabar solo hay que añadir que, con el fin de hacer mas cómoda la lectura de este trabajo, algunos detalles de índole más “técnica” han sido separados del cuerpo principal del texto, y llevados a los apéndices A, B, y C, remitiéndose a ellos oportunamente.

Introduction

This work is devoted to the study of the hadroproduction of heavy resonances and related topics. The discovery of the J/ψ and Υ resonances by Aubert, Ting et al. (1974) and by Innes et al. (1977), respectively, triggered both experimental and theoretical intense activities in this field (currently still continuing), posing at lot of challenges which provided clever solutions. For instance: classifying the members of either ψ or Υ family, solving the problem of the theoretical deficit of heavy quarkonium production with respect to the experiments, etc. Currently, one of the most striking issues of heavy quarkonia physics is the J/ψ unexpected (un)polarization, clearly indicating that the production mechanism is still imprecise. Aside, there is the problem of how to deal with the nonperturbative part of the heavy resonances production (annihilation) mechanisms, and other subjects that link with the grounds of the Quantum Chromodynamics (QCD).

Over the last decade, hadroproduction of heavy quarkonia has received a lot of attention from both theoretical and experimental viewpoints, to explain the discrepancy between the so-called colour-singlet model (CSM) and the experimental data, amounting to a factor of about 50 for direct J/ψ hadroproduction at the Tevatron. In particular, the colour-octet mechanism (COM) can be viewed as the (relativistic) generalization of the CSM and hence the most natural explanation for the unexpected surplus of heavy resonance hadroproduction. Nevertheless, when applied to other production processes like photoproduction at HERA, problems initially arose which cast doubts on the validity of the COM, although recent progress has been done allowing for a better understanding of the situation. Furthermore, results from Tevatron on charmonia polarization (one of the foremost predictions of the COM) seem to indicate even the failure of a naive application of the colour production mechanisms for charmonia [1]. More astringent tests of heavy quarkonia production are thus required to enlighten the situation, which can be qualified as rather confusing at present.

In this work, due to the wide area that the hadroproduction of heavy resonances covers, we preferred to focus only on the $\Upsilon(nS)$ $(n = 1, 2, 3)$ family, below open bottom production, since its current interest. Mainly what we did is to analyze some relevant subjects for such family using a Montecarlo physics generator, PYTHIA, introducing (as less as possible) changes in the original software in order to reach a better reproduction of the Υ physics. It must be pointed out that we keep our event generation at *particle level*. The additional amount of challenges which the introduction of detector effects poses is enough to justify another study by itself. Therefore we decided to postpone this goal to future works.

The study begins with a chapter that analyzes some experimental issues on heavy quarkonia production, pointing out the important role that the ATLAS detector at LHC can play in this regard. First, we describe the general features and characteristics of the ATLAS detector. Subsequently an outline on experimental aspects of the Υ production is presented. The chapter ends with a brief description on jets physics in this detector, since this kind of measures will be very important in our proposal to probe gluon densities in the proton using Υ hadroproduction.

Although the main goal of the LHC machine is the search for and the study of the physics beyond the Standard Model, the expected huge rates of bottom quark production make especially interesting the foreseen B physics programme for the LHC project. In fact a specific experiment (LHCb) will focus on B physics, while the two general-purpose experiments ATLAS and

CMS will dedicate special periods for data taking to this aim. Among heavy flavour physics, heavy quarkonia production and decays have historically played a very important role in the development and test of QCD as the best candidate to account for the strong interaction dynamics, and likely will continue keeping an outstanding position in this task.

The main goal of chapter 2 is revising some theoretical aspects on bottomonia production, beginning with an overview on heavy quarkonia from the quark model picture. Some relevant heavy quarkonia production models as CSM, colour-evaporation model, and -especially - COM are visited later, pointing out the most relevant features involved in this work. Due to the importance of the latter, here we anticipate that basically, such a production mechanism is based on the formation of an intermediate coloured state during the hard partonic interaction, evolving non-perturbatively into physical heavy resonances in the final state with certain probabilities governed by non-relativistic QCD (NRQCD).

Later, chapter 3 describes the most relevant techniques used in order to generate the $\Upsilon(nS)$ family, as well as a description on the changes and new implementations in the original software of PYTHIA: Production sources, a discussion about the choice of parameters, introduction of higher order QCD effects as initial radiation, how Altarelli-Parisi evolution of the fragmenting gluon effects are incorporated in the software, and more; later we found details about the implementation of the colour-octet mechanism in PYTHIA, and procedures followed fitting $\Upsilon(nS)$ NRQCD matrix elements, and more topics. In summary, all the tools that we needed when carrying out the bottomonia hadroproduction analysis.

In chapter 4 we focused on the study of the information available on Υ production, basing our analysis of bottomonia inclusive production on the results from Run IB of the CDF collaboration at the Fermilab Tevatron. This means significantly more statistics than the data sample from Run IA: We analyze the differential $\Upsilon(nS)$ cross sections, extracting some relevant

NRQCD matrix elements, paying attention to the problem concerning the factorization of the cross section; and also we extend our concern to analyze $\Upsilon(1S)$ production sources, comparing them with the experimental data, the $\Upsilon(nS)$ integrated cross sections etc.

In chapter 5 we make some predictions on bottomonium hadroproduction at the forthcoming LHC energies and kinematic conditions. To carry out this programme we extrapolated the information obtained in the preceding chapter: We show the expected differential and integrated cross section for all $\Upsilon(nS)$ resonances, as well as ratios of these integrated cross sections.

However these are not the only predictions on LHC that this works provides: In chapter 6 we present a proposal to probe gluon densities in the proton using Υ hadroproduction, within the framework of the colour-octet mechanism. The experimental determination of these densities currently is one of the big goals for a better understanding of the hadronic physics. Aside the proposal, we included predicted production rates, and details that arose during the development of the idea.

It must be stressed, that our proposal should be viewed along with other related methods of constraining the gluon distribution in hadrons like di-jet, lepto-pair and prompt photon production. We must clearly state that it relies on the dominance of a particular production mechanism at high p_T (the COM) predicting a dominant contribution from gluon fragmentation. In spite of this and other assumptions (such as the validity of the factorization of the cross section), our feeling is that LHC collaborations should keep an open mind on all the possibilities offered by the machine, thereby exploring the feasibility of this proposal. For all these and other physical reasons, it is worth to estimate, as a first step, the foreseen production rate of bottomonium resonances at the LHC and this constitutes one of the goals of this work.

Finally, just to add that, in order to help the reading of this work, a lot of technical details have been separated from the main body of the text, gathering them in the appendices A-B-C that will be duly cited.

Chapter 1

Heavy Quarkonia: An experimental overview

The forthcoming Large Hadron Collider (LHC) represents a new frontier in particle physics due to its higher collision energies compared to the existing accelerators. LHC is a proton-proton collider with 14 TeV center of mass energy and optimum design luminosity $\mathcal{L} = 10^{34}\ cm^{-2}\ s^{-1}$. This challenging project has as one of its main goals the search for and the study of new physics. Nevertheless, taking into account that in the low luminosity period ($\mathcal{L} = 10^{32}\ cm^{-2}\ s^{-1}$), it is expected around 10^{11} bottom quark events per year; the attention of the physics community is focused also on the possibilities on B physics. Aside the LHCb, that is a specific experiment for B physics, ATLAS, as a general-purpose detector, will be also used for this kind of physics.

Moreover, QCD processes will be studied at the LHC: Its predictions will be tested, and precision measurements will be performed, allowing additional constraints to be established; for instance, on distributions of partons in the proton, or providing of accurate measurements of the strong coupling constant at different scales. Topics concerning heavy quarkonia are one of the most useful ways to develop and test QCD. Thus, it is worth to enlighten

the role of heavy quarkonia experiments.
Along this chapter some outlines about experimental issues, mainly focused on ATLAS [2], related to this work are presented; the two main topics that will be treated are the ability of the powerful LHC experiments in order to take data about bottomonia hadroproduction, and their feasibility to test the gluon density in protons from heavy quarkonia inclusive hadroproduction.

Nevertheless, here we will attempt to offer only some features that have to be taken into account in working experimentally on this matter, rather than a detailed work. First of all, an ATLAS presentation in order to describe the tasks of the different sub-detectors.

1.1 The Atlas detector: Requirements and structure

Due to the fact that ATLAS must be very sensitive to a variety of final-state signatures that label the particles to be detected, the following general features are required [3], changing its priority when LHC will evolve from low to high luminosity:

- Very good electromagnetic calorimetry for electrons and photons identification and measurements complemented by hermetic jet and missing E_T calorimetry.
- Efficiency tracking at high luminosity for lepton momentum measurements, b-quark tagging, as well as heavy-flavour vertexing and reconstruction capability.
- Efficiency tracking at low luminosity and secondary vertex identification of heavy-flavours.
- Good measurement in an independent way of the muon-momentum from low up to high luminosity.

- Very low-P_t trigger capability at lower luminosity.
- Triggering and measurements of particles at low p_t thresholds.
- Large acceptance in pseudorapidity η coverage[1].

Essentially ATLAS is a cylinder composed of shells, each one being an independent detector with specific(s) role(s), but working in group, reaching in this way the best results.

ATLAS is a 7000 tons detector consisting, as can be seen in the Figure 1.1, from in to out of:

- Inside, an **inner superconducting solenoid** around the inner detector cavity that provides a magnetic field of 2 T.
- A **calorimetry area** consisting in a **Liquid Argon electromagnetic calorimeter**, that also shares the solenoid cryostat, and an **hadronic calorimeter**, consisting in one barrel and two extended barrel cylinders on each side. The whole calorimeter system contributes to the very good jet and E_T^{miss} performance of the detector (see Figure 1.3).
- The **muon spectrometer**, having an air-core toroid system and two toroidal end caps (see Figure 1.4).

The whole system has an extremely complicate read-out data system that is organized in three trigger levels [3, 4].

1.1.1 The Inner Detector

This detector has as a main goal the momentum measurements of charged particles, to contribute to the tracking and to optimize the electron identification. It consist in 1.15 m radius cylinder of a 6.8 m long (see Figure 1.2).

---

[1] $\eta = -\log(\tan\theta/2)$ where θ is the polar angle of the direction of the particle with respect to the beam axis.

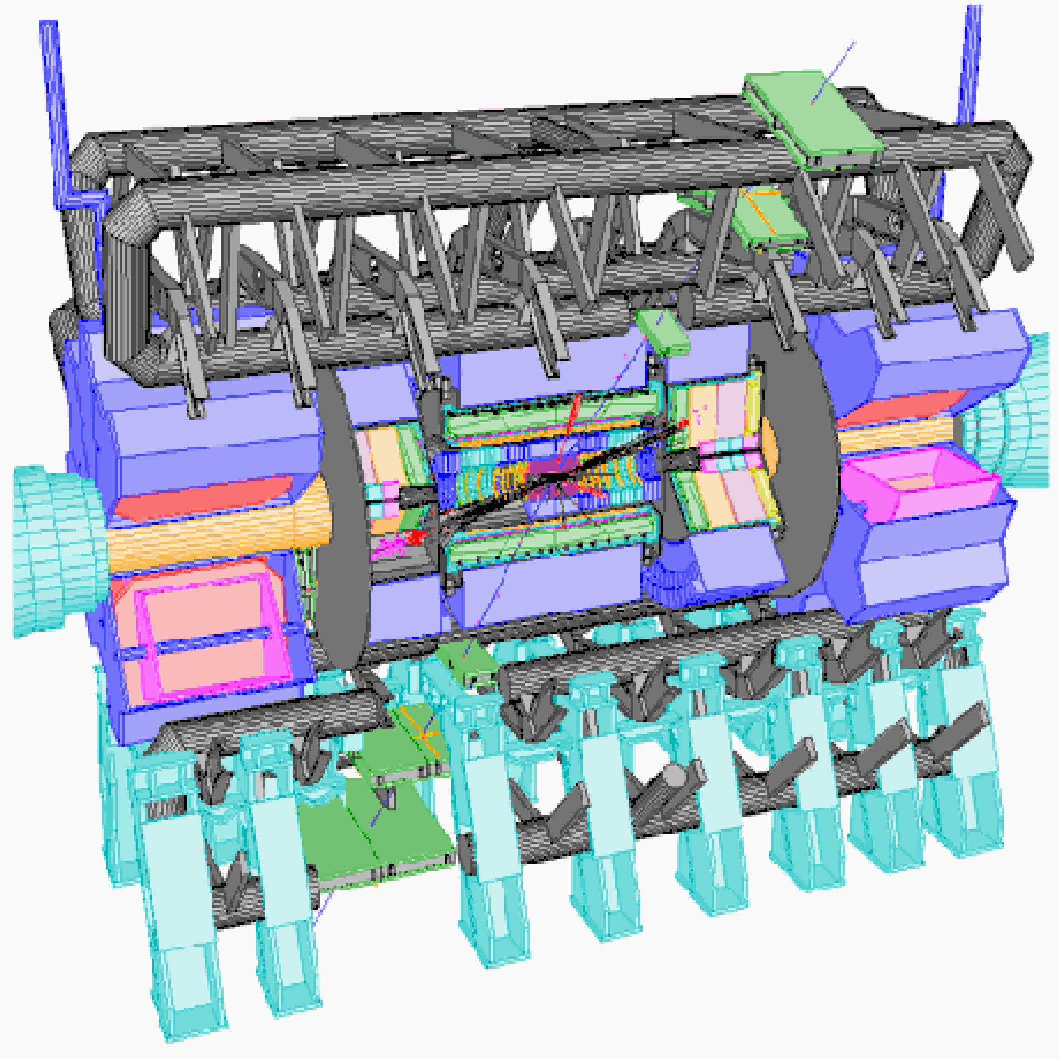

Figure 1.1: *A general view of ATLAS detector.*

Its design takes into account the high radiation level that it will suffer.

In the cylinder central zone, there are the semiconductor silicon trackers (SCT), formed by silicon bands and Ga-As cells. Its construction takes into consideration that it must be an appropriate number of surfaces and granularity enough in order to have a good tracking at high luminosity and a good jet reconstruction at low luminosity.

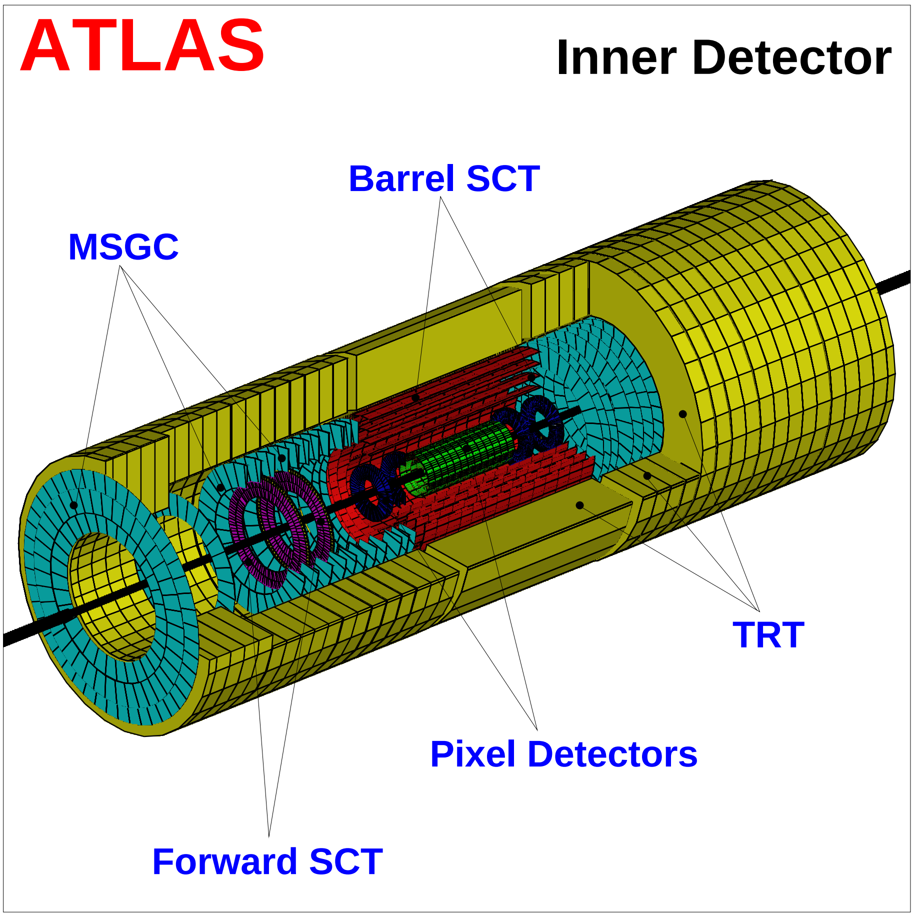

Figure 1.2: *View of the Inner detector.*

Following the SCT there are the transitional radiation trackers (TRT), their job is mainly to act as a particle identifier, and also as a tracker, by measuring continuous tracks with a transversal momentum greater than 0.5 GeV. Essentially consists in a couple of drift tubes following the beam axis with an emission environment where the transition radiation is produced, allowing for instance to detect the X-ray produced when an ultrarrelativistic particle reaches the detector.

1.1.2 The Calorimetry

ATLAS calorimetry is devoted to two complementary purposes: Electromagnetic calorimetry and hadronic calorimetry, as can be seen in the Figure 1.3. The former system is lodged inside the second one. In the electromagnetic calorimeter the solenoid is merged in a liquid Argon environment as an active medium, and surrounded by a cryostat; the whole is closed by the hadronic calorimeter.

It must be noticed that there are some requirements in order to have a good electromagnetic calorimetry:

In a wide transversal energy range it must be able to identify photons and electrons. The longitudinal and transversal segmentation of the calorimeter allows to reconstruct the structure of the shower and to reject jets, the main background of photons and electrons.

It is mandatory to optimize the granularity $\triangle\eta \times \triangle\phi$, therefore an agreement between resolution, electronic background and pile-up of the signals is required.

A minimal depth of 26.5 X_0 and 28 X_0 (X_0 is the Radiation Length) for the barrel and its extension respectively, is enough to avoid leakages of showers.

The electromagnetic calorimeter is shared out in three main layers. The first one, plays the role of a preshower, that is preceded by a presampler in the barrel zone, in order to preserve the energetic resolution and path of the particles in crossing the solenoid and the cryostat. The last layer is devoted to improve the transversal energetic resolution.

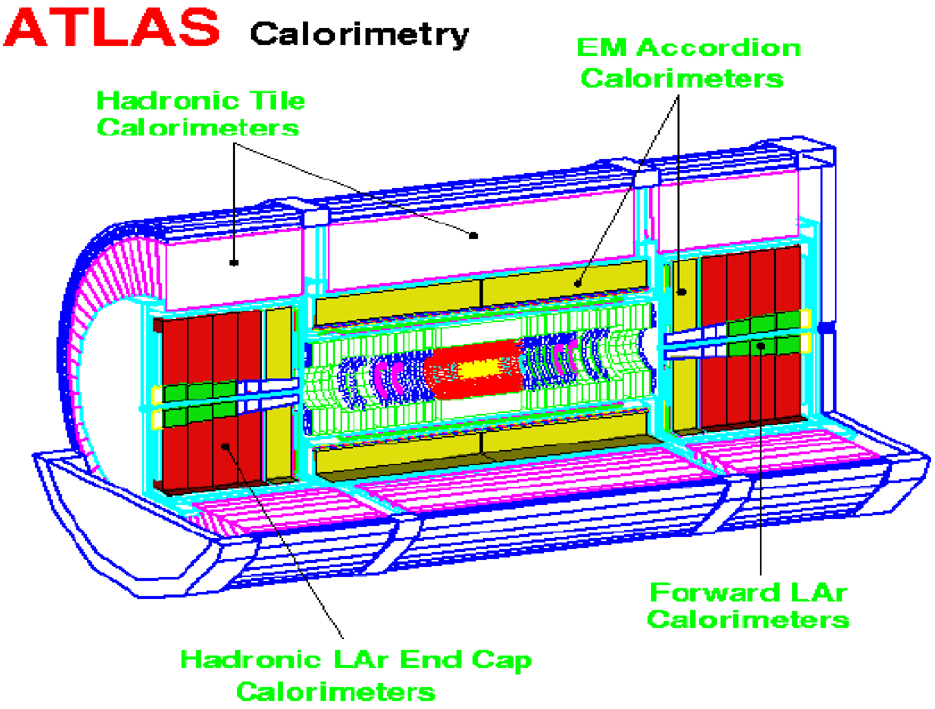

Figure 1.3: *A general view of TILECAL and LIQUID ARGON calorimeters.*

The hadronic calorimeter TILECAL [4], consists in a central barrel and two extensions, one at each side. Essentially this Tile Calorimeter is a sampling device made out of steel and scintillating tiles, as absorber and active material respectively, placed in a highly periodic structure forming modules in the radial direction with respect to the beam axis; this periodicity allows the construction of a large detector (currently TILECAL has 500000 tiles). As a read-out system, each tile is coupled with the wavelength-shift (WLS) optical fibres, along the two outside faces, each WLS fibre is coupled to an specific photomultiplier providing an exact view of the detection point. Thus, this system provides a projective geometry for triggering and energy reconstruction by the definition of tridimensional cells from a mapping of each tile-fibres-photomultiplier setup. Due to the importance of this system in order to have a good energy reconstruction, it is not so odd that the whole optical system (tiles, fibres and photomultipliers) has to be constructed upon severe requirements [4].

The hadronic calorimeter, has as a main role to reconstruct the jet energies produced in the pp collisions. On the other hand, some series of requirements are made for this detector:

- A good efficiency along a dynamical range of energies from a few GeV up to some TeV.
- Ability to resolve physical events over a background of 21 events minimum bias for each beam-cross (soft-scattering events that overlaps in the bunch-crossing), this requires a fine granularity and a quick feedback.
- The system has to be highly resistant to the high radiation level, taking into account the flux rates expected along its operation time (10 years).
- It is expected an intrinsic resolution of

  $$\triangle E/E = 50\%/\sqrt{E} \oplus 3\%$$

  with a segmentation $\triangle\eta \times \triangle\phi = 0.1 \times 0.1$.
- Good energetic resolution for all η intervals.

- Good linearity along all of the energy range and good hermeticity.
- Uniformity in ϕ and η.

1.1.3 The Muon Spectrometer

The ATLAS muon spectrometer (see Figure 1.4) is a system of superconducting air-core toroidal magnets that surrounds the other detectors. This detector consists in a central part of 26 m length and 19.5 m external diameter, and two end-caps of 5.6 m length and 10.7 external diameter. Each toroid has 8 coils along the beam axis.

The requirements for this detector are:

A good p and p_T resolution and good angular acceptance. This detector must work even without the other detectors, and even having pile-up signal problems must reconstruct correctly the muon tracks.

In the case of great precision measurements they will be used two different chambers: Monitored Drift Tubes (two multilayers of three or four planes of pressurized thin-wall aluminium drift tubes), and Cathode Strip Chambers (a series of fast multiwire proportional chambers). There are also the Resistive Plate Chambers (that combine the spatial resolution of the multiwires devices with the time resolution of the scintillating counters) and Thin Gap Chambers (multiwire chambers working in saturation mode).

1.2 Global parton analysis and kinematics at LHC

In this section, we present a brief discussion on the role that could be done by LHC, focusing on the ATLAS experiments, in the determination of parton distribution functions. This determination arises from the study of several processes. Although, this point in relation with the experiments on

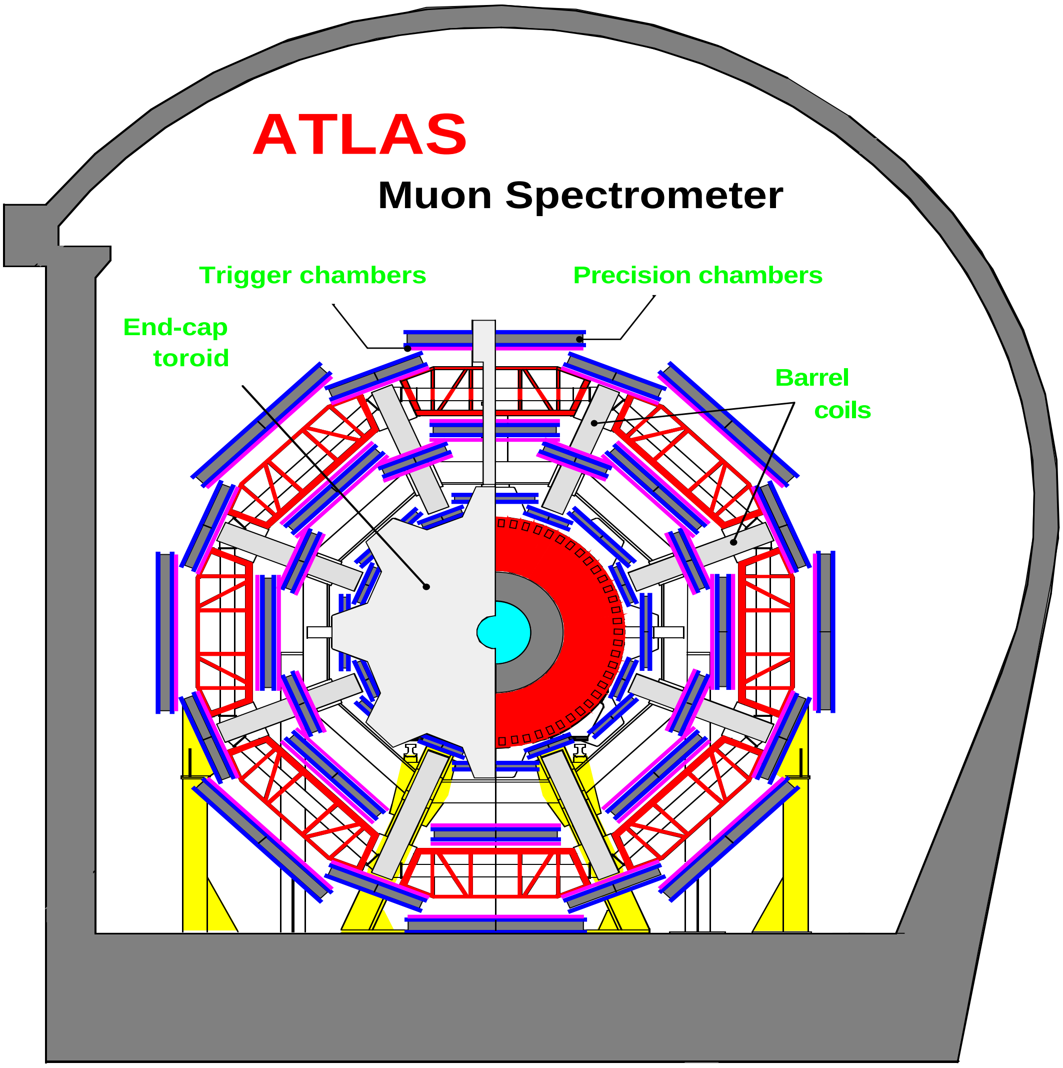

Figure 1.4: *Schematic view of the Muon Spectrometer.*

bottomonia hadroproduction will be treated later separately.

The calculation of the production cross section at the LHC, for interesting physics processes and their backgrounds, relies upon a precise knowledge of the momentum fraction x distribution of the partons in the proton inside the relevant kinematic range. These parton distribution functions (PDFs) are determined by means of global fits to data from deep inelastic scattering (DIS), Drell-Yan (DY) processes, jet and direct photon production at current energy ranges.

ATLAS measurements of DY (including W and Z) processes, direct photon and jet production will be extremely useful in determining such PDFs. These data can be input to the global fitting programs, where they can serve to either confirm or constrain those PDFs in the kinematic range of the LHC [2]. DY production will provide information on the quark and antiquark distributions, both for valence quarks and sea quarks:

The knowledge of the exact role of the sea quarks in such interactions actually is an important source of uncertainty -besides α_s- in determining PDFs. In addition, direct photon and jet production processes will provide information about the gluon distribution (through the measurement of the sea distribution), whose behaviour is yet still imprecise, especially at low x; here, the gluon behaviour is strongly model dependent, needing thus an improvement on the experimental uncertainties at those x ranges in order to discern among models.

Another possibility that was suggested [5] is to directly determine parton-parton luminosities, and not the parton distributions per se, by measuring well-know processes such as W/Z production. This technique would not only determine the product of PDF in the relevant range but would also eliminate the difficult measurement of the proton-proton luminosity.

1.3 Atlas and Quarkonia

This section points out the exciting role that the ATLAS detector can play in order to make feasible a wide list of experimental studies (also together with other LHC experiments as CMS and LHCb) around the bottomonia states. Among these, here is outlined an experimental outlook about bottomonia hadroproduction, separation of Υ production sources, and the experimental procedures in a possible use of botomonia hadroproduction to test the gluon densities inside the hadrons.

1.3.1 Υ production cross section measurements

The study of bottomonia production in hadron colliders should permit a stringent test of the colour-octet production mechanism, particularly regarding the predicted [6] (mainly transverse) polarization of the resonance at high-p_T, whereas other approaches, like the colour evaporation model (see chapter 2), predict no net polarization; indeed, LHC experiments will cover a wider range of transverse momentum than at the Tevatron, allowing to explore the region $p_T^2 >> 4m_b^2$, where m_b denotes the bottom quark mass.

From an experimental point of view, the Υ detection can be done either through its muonic decay $\Upsilon(nS) \to \mu^+\mu^-$, or through the e^+e^- channel, analyzing whatever desired feature, as the differential cross section versus p_T; thus the role of the muon spectrometer comes out: More statistics for p_T distributions can be provided to improve the current data available from the Run-1b CDF data [7].

Once data are obtained, the determination of the differential cross section can be done using the following expression:

$$\frac{d^2\sigma}{dp_T dy}\,|_{y_0} \times BR(\Upsilon \to \mu^+\mu^-) = \frac{N_{fit}}{A\ \epsilon\ \int \mathcal{L}dt\ \ \triangle\, p_T \triangle\, y}$$

where N_{fit} is the number of signal events for each p_T, A is the product of the detector acceptance and the level trigger efficiency, ϵ stands for the product of all reconstruction efficiencies, $\int \mathcal{L}dt$ is the integrated luminosity, $\triangle p_T$ is the uncertainty of p_T (i.e. the width of the p_T bin) and $\triangle y$ is the rapidity range.

In addition, Υ decays -as well as J/ψ and Z ones- can serve to make checks on the symmetry of the muon trigger and reconstruction efficiencies for positive and negative leptons in order to control the experimental systematic uncertainties. On the other hand, the possibility of using an electron-tagged sample gives to ATLAS a way of controlling the experimental uncertainties related to muon tags.

1.3.2 Υ production sources measurement

Another question is the separation between different Υ production sources. As we shall see, for bottomonia production one can distinguish between direct production and the indirect one from the feed-down of higher resonances. For instance in the $\Upsilon(1S)$ case there is direct production plus contributions from the strong and electromagnetic decays of the Υ(2S) and (3S), and electromagnetic decays from χ_{bJ} resonances.

Currently, data from the PDG and from CDF-Run1b are available, but the errors could be reduced: For instance there is an error of $\sim 50\%$ in the BR of the $\chi_{b0}(2P)$ decay to $\Upsilon(2S)$, [8]. Those BR values, as will be shown in chapter 3, are very important in finding the Nonrelativistic QCD matrix elements. Besides, another task still unsettled is the confirmation of the J values for several $\chi_{bJ}(nP)$ states [8]. Also in the case of CDF measurements [9] the accuracy of the values for the Υ production sources can be improved.

Once again the role of Atlas to this work comes out. The Liquid Argon calorimeter can be used to improve the accuracy of the branching ratios of the χ_{bJ} decaying to Υ states, rejecting other photon sources as from η or K_S^0 decays. The hadronic calorimeter (TILECAL) can be used to obtain signatures of strong decays yielding pions.

Just below we can see some examples of Υ channels that, together with the leptonic channels, can be used to identify them.

- $\Upsilon(2S)\to\pi^+\pi^-\Upsilon(1S)$
- $\Upsilon(2S)\to\pi^0\pi^0\Upsilon(1S)$
- $\Upsilon(2S)\to\gamma\chi_{bJ}(1P)\to\gamma\gamma\Upsilon(1S)$

The fraction of $\Upsilon(1S)$ coming from χ_{bJ} decays is usually calculated from data by means of:

$$F_{\chi_{bJ}}^{\Upsilon(1S)} = \frac{N^{\chi_{bJ}}}{N^{\Upsilon}\ A_{\Upsilon}^{\gamma}\ \epsilon^{\gamma}}$$

where $N^{\chi_{bJ}}$, N^{Υ} are the number of reconstructed χ_{bJ} and Υ, A_{Υ}^{γ} is the photon acceptance, and ϵ^{γ} is the efficiency of the isolation cuts.

An advantage in dealing with Υ production, with respect to the charmonia case, is the possibility to reach smaller transverse momenta, due to the experimental selection requirements.

On the other hand, the associated production of an Υ meson together with a W or Z boson has been suggested [10] as an alternative check for different model predictions. The dominant mechanism in this process is expected to be the production of a $b\bar{b}$ pair in a colour-octet state (see chapter 2), binding then to a P-wave state an decaying later into an Υ state. The expected cross section amounts to 44 fb for $\Upsilon+W$ and 7 fb for $\Upsilon+Z$. This channel could also be used to search for heavy particles, decaying into a W or Z boson with a $b\bar{b}$ pair.

1.4 Probe of the gluon density in the proton

One of the goals of the LHC project is to perform precise tests of the Standard Model of strong, weak and electromagnetic interactions and the fundamental constituents of matter. In fact the LHC machine can be viewed as a gluon-gluon collider to some extent. On the other hand, many signatures of physics (and their backgrounds), both within and beyond the Standard Model, involve gluons in the initial state [2]. Therefore an accurate knowledge of the gluon density in protons acquires a special relevance for all these reasons.

Focusing on the role of ATLAS in this issue: As will be seen, in chapter 6 there is a proposal in order to test the shape of Parton Distribution Functions (PDF) through bottomonia hadroproduction. The main goal of this test is to measure *ratios* of cross sections at several p_T values. On the other hand, the theoretical expression that allows this test involves partonic cross section calculations. Then, in principle the knowledge of the non relativistic QCD matrix elements is required (see chapter 2); however the errors of such values are still broad. Nevertheless, performing ratios will allow to remove theoretical uncertainties arising from such matrix elements. Indeed, this proposal can be stretched out beyond: If whenever the theoretical uncertainties of the values of those matrix are enough small, it will be possible not only to test the shape of the PDF, but also this proposal would provide the *direct* knowledge of this PDF itself, essentially through this proposal, but in this case without the need of the ratios.

This test involves the jet production from the additional gluon(s), thus needing of a good definition of such jets. Therefore, the detector must be able to identify them (in joint with the additional signature of a few light hadrons), and a good resolution is required in order to identify back-to-back jets, disentangle them by means of a jet cone algorithm (as will be explained in the following section); here the hadronic calorimeter can play a key role. Also the electromagnetic calorimeter is needed here to reject (or include) the χ_{bJ} contributions involved in the Υ hadroproduction, since this source must be controlled in the test of the PDF. In the following section we will treat on the experimental features of jets. Aside, the statistics required to this proposal can be enhanced adding the channel $\Upsilon(nS)\rightarrow e^+e^-$together with the muonic one. Thus, electron identification using inner detector, and a good electromagnetic calorimetry is again required.

On the other hand the detector effects have to be accurately determined; since from this test we expect, at particle level, that the number of events to be collected, depending on what p_T region we consider, are from about 10^5 down to around 10^2 per year. Those numbers are enhanced by modifying the rapidity condition, and including the channel above mentioned. The detector effects - even though they will dismiss such statistics - from the expected ATLAS efficiencies and acceptances, will not represent a dramatic loss of events, as we shall see in chapter 6, where we estimate the expected statistics taking into account all those factors.

1.5 Some experimental topics on jets

At hadron colliders, the most prominent signature for a hard scattering process to take place is the production of particles with a large total transverse momentum, i.e. the jets. The reconstruction of jets allows to understand those hard scattering processes. Thus, one has to take into account the evolution of the partonic system from the hard scattering to the hadrons in the final state. When the partonic system is evolving, there are parton showers (additional partons with, typically, decreasing transverse momenta), fragmentation of coloured partons to the colourless hadrons, as well as multiple interactions in a single bunch crossing. All those effects will have to be taken into account in our study of gluon density.

The definition of jets depends on their internal structure. Thus it is important to provide direct measurement of it. The measurement will include the study of the jet shape, defined as the fraction of energy inside a cone of radius r ($r < R$) with respect a cone of size R defining the jet.

At the LHC an experimental goal is to select events with mini-jets, (jets with not too large transverse energy). The triggering of these events has to be studied in more detail. In principle, it will be done on the basis of a minimum-bias trigger (at the first level of the ATLAS trigger). Higher level triggers, having access to the full granularity of the subdetectors could enhance the signal by reconstructing jets with low transverse energy. This also implies the need for a good p_T jet tagging at low luminosity.

The occurrence of jets with small transverse momentum poses a challenge to QCD predictions, in particular to this work as has been pointed out above. In order to study the transverse correlation between partons, jets with small transverse momentum have to be selected. At LHC energies, extrapolations predict that up to 50% of all inelastic events contain jets with transverse energies larger than 7 GeV. The understanding of the event structure in terms of jets with small transverse momentum is important in order to use the jet vetoing [2].

The information obtained from a minimum-bias trigger at trigger level 1 - using either random bunch crossing or information from additional dedicated detectors in the forward region- can be used to study the properties of these inelastic events, not only in terms of particle production, but also in terms of the jet with small p_T and their properties. Moreover, as yet explained, the higher level triggers of ATLAS could also provide a surplus in the sample of minimum-bias events with jet activity, by performing a jet reconstruction.

1.5.1 Experimental uncertainties

One important aspect in all jet studies is the relation between the jet transverse energy measured in the detector and the "true" transverse energy of the parton in the hard scattering process. The differences among these two quantities can be due to the following experimental effects that can shift the jet energies measured as well as to smear them:

- Calorimeter response: Deviation from uniform response over the acceptance -due to dead material, gaps, and intercalibration errors-, non linearity in the response to low and high p_T particles, the e/π ratio and the p_T dependence of the jet particle content.

- The effect of the magnetic field in providing a p_T cut-off for particles to reach the calorimeter.
- The effect of the underlying event and/or the contribution of other interactions in the same bunch-crossing.
- Production of neutrinos and muons inside a jet which lead to a smaller energy deposition in the calorimeter.
- Finite size of jet reconstruction volume, this is a problem if it is not modeled correctly by the NLO calculations.

When a mandatory correction of those effects is performed, the following systematic sources of uncertainties arise, needing to be quantified (it is desirable a control of such uncertainties to a precision less than 1% for energies below 1 TeV and to about 10% for E_T of about 3 TeV):

- Determination of the jet energy scales of the calorimeters.
- Control over the jet trigger efficiency.
- Knowledge of the luminosity for the overall normalization.
- Energy resolution for jets.
- Linearity of the calorimeter response at different p_T values.
- Determination of the calorimeter response to hadrons, electrons and photons.

Chapter 2

Heavy Quarkonia hadroproduction: A theoretical introduction

In this chapter the basic theory ideas, underlying the foundations of this work are sketched. But this outline does not attempt to be even a theoretical summary about the monumental work developed by many physicists along the latest 25 years on quarkonia topics; indeed, there are excellent reviews to consult about this startling field (some of which will be duly cited). On the other hand, those aspects related to the later phenomenological analysis will be conveniently stressed.

2.1 Quarkonia: Colour-singlet and Colour-octet

Essentially in a naïve picture, quarkonium consists of a quark and an antiquark placed at distance r one from the other; this distance is supposed to be smaller than the typical size of a hadron $\Lambda_{QCD}^{-1} \sim 1fm$. An estimation of this size can be done [11] assuming one-gluon exchange as potential force among them, hence the Bohr radius of the heavy diquark is $\tilde{r}_0 \simeq 1/c_F\alpha_s(r_0^{-1})\hat{m}_{ij}$, where c_F is the colour factor, α_s is the strong coupling constant and $\hat{m}_{ij}$ stands for the reduced mass of the (Q_iQ_j) system; in the bottomonium case:

$c_F = 4/3$, $m_b \simeq 5$ GeV and thus $\hat{m}_{ij} = m_b/2 \simeq 2.5$ GeV. Since the typical velocity of the bottom quark inside the meson satisfies $v^2 \sim 0.1$, $\alpha_s(r_0^{-1}) \simeq \alpha_s(m_b v) = \alpha_s(1.6\ GeV) = 0.376$ (with 5 flavours). Then $\tilde{r}_0 \simeq 0.2$ fm ; i.e. about 20% of the typical size of a hadron.

Far away from the quark-antiquark pair, at a distance $R >> r$ the chromo-electric field is that of a dipole, obeying to:

$$E_\theta \sim g(R)\,\frac{r\ cos\theta}{R^3} \tag{2.1}$$

the strength of which is governed by means of the QCD coupling constant, $g(R)$, [12] at distance scale of order r. At large distances from the dipole this description in terms of a perturbative vacuum remains no longer valid. When the field strength takes a critical value $\sim \Lambda_{QCD}^2$, the vacuum quickly turns non perturbative, thus the dipole can be described as a perturbative bag inside a non perturbative vacuum. The radius of this bag (R_b) goes as $R_b^3 \sim \Lambda_{QCD}^{-2}\ g(r)$.

In the perturbative vacuum the interquark force is *essentially* dominated by single gluon exchange. If we draw (see figure 2.1) the corresponding Feynman graph of a quark and an antiquark carrying incoming colours j, l, respectively, and i, k after the exchange of a gluon, that carries a (four)momentum q, then the amplitude works as

$$\sim \frac{1}{\vec{q}^2}\sum_a T_{ij}^a T_{kl}^a$$

Since the Fourier transform of $1/\vec{q}^2$ is proportional to $1/r$, the momentum dependence gives rise to a Coulomb-like potential; this fact will play an important role for later applications in this work to phenomenological aspects of resonance hadroproduction. Focusing on the colour factor $T_{ij}^a T_{kl}^a$, where T^a are the generators of $SU(3)_c$ in the fundamental representation, the strength of the interaction depends on the relative colour of the $Q\overline{Q}$ state. Since Q is in the **3** representation of $SU(3)_c$ and $\mathbf{3} \otimes \overline{\mathbf{3}} = \mathbf{1} \oplus \mathbf{8}$, the

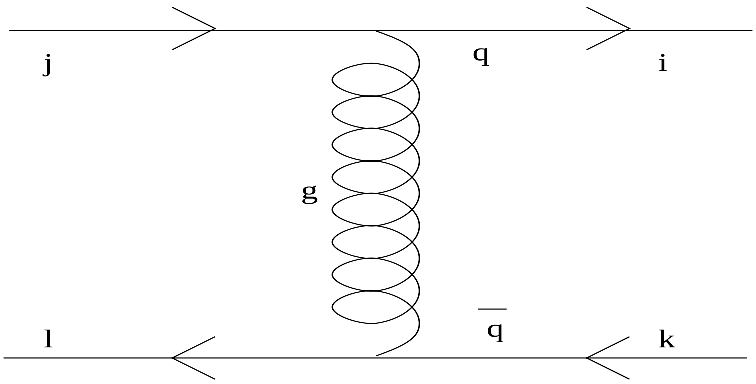

Figure 2.1: Feynman graph corresponding to a single gluon exchange of a quark-antiquark pair.

$Q\overline{Q}$ force is in either of these two channels. To find the **1** and **8** components of the force, we consider the pure states

$$(Q_j\overline{Q}_l)_1 \;\equiv\; \delta_{jl}\;(Q\overline{Q})$$
$$(Q_j\overline{Q}_l)_8 \;\equiv\; Q_j\overline{Q}_l \;-\; \tfrac{1}{3}\delta_{jl}\;(Q\overline{Q})$$

Contracting each state with

$$\sum_a T^a_{ij}\;T^a_{kl} = \;\frac{1}{6}\left[\;3\;\delta_{jl}\;\delta_{ik}\;-\;\delta_{ij}\;\delta_{kl}\;\right]$$

one obtains

$$\begin{aligned}\sum_a T^a_{ij}T^a_{kl}(Q_j\overline{Q}_l)_1 &= \tfrac{8}{6}(Q_i\overline{Q}_k)_1\\ \sum_a T^a_{ij}T^a_{kl}(Q_j\overline{Q}_l)_8 &= -\tfrac{1}{6}(Q_i\overline{Q}_k)_8\end{aligned}$$

It can be seen that the force in the colour octet channel is of opposite sign (repulsive) and weaker than in the colour singlet channel by a factor of 1/8. Thus the quark-antiquark pair in a colour octet configuration comes out to be repulsive, although we shall see that according to the Colour Octet Mechanism the possibility exists for the formation of an intermediate $Q\overline{Q}$ coloured state in the hadronization process leading to a physical quarkonium. The explanation of this apparent paradox is that a state in an octet configuration can bind to a gluon, provided the gluon attraction ($\mathbf{3}\otimes\mathbf{8}$) to both quarks overcomes the repulsion between them. Such states in which the glue state plays a particle-like role in the binding are called hybrids (hybrid of a glueball and a pure quarkonium state).

In QCD the total angular momentum J, the charge conjugation $C = (-1)^{L+S}$, and the parity $P = (-1)^{L+1}$, are exactly conserved numbers. Hence the heavy quarkonia energy eigenstates $|H>$ are usually labeled by means of such numbers J^{PC} (Along this work the labels are: $\Upsilon(nS):1^{--}$ and $\chi_{bJ}(nP):J^{++}$). At leading order $|H>$ is assumed to be a pure quark-antiquark state, $|Q\overline{Q}>$ (according to a non-relativistic potential model), and hence the $Q\overline{Q}$ pair must be in a colour-singlet state and in an angular momentum state ${}^{2S+1}L_J$ that it is consistent with the quantum numbers of the meson. In summary:

$$\text{potential model: } |H(J^{PC})>=|Q\overline{Q}(n^{2S+1}L_J)_1>$$

2.2 Quarkonia: Production mechanisms and Cross sections

The production of quarkonia states below the open charm/bottom presents a particular challenge to QCD. Because of the relatively large quark masses, $c\bar{c}$ and $b\bar{b}$ production are perturbatively calculable; however, the early theoretical predictions on quarkonia hadroproduction gave a deficit w.r.t. the experiments; this disagreement led to alternative models in order to reconcile them, as we shall see.

The differential cross section of heavy-quarkonia inclusive production is given by the factorized expression

$$\begin{aligned} d\sigma[AB \to (Q\overline{Q})X](p_A, p_B) = & \sum_{ab} \int dx_1 \; dx_2 \; f_{a/A}(x_1, \mu_F^2) f_{b/B}(x_2, \mu_F^2) \\ & \times \; d\hat{\sigma}[ab \to (Q\overline{Q})X'](x_1 p_A, x_2 p_B, \mu_F^2, \mu_R^2) \end{aligned} \tag{2.2}$$

where a, b represent the interacting partons, $f_{a/A}(x_a, \mu_F^2)$ and $f_{b/B}(x_b, \mu_F^2)$ stand for their parton distribution functions (PDF) in hadrons A and B respectively, evaluated at momentum fraction x. The short distance cross section $d\hat{\sigma}$ is calculable as a perturbation series in $\alpha_s(\mu_R)$ (the strong coupling evaluated at the renormalization scale μ_R).

This factorization form relies on the grounds of the factorization theorem [13], and requires the introduction of an arbitrary scale μ which separates the large momentum scale from the lower momentum scale. Actually, this factorization is more rigorous in the heavy quarkonia annihilation framework than in inclusive production. The factorization of the cross section can fail if there is connection between the initial and final states besides the propagator in the example of figure 2.2.

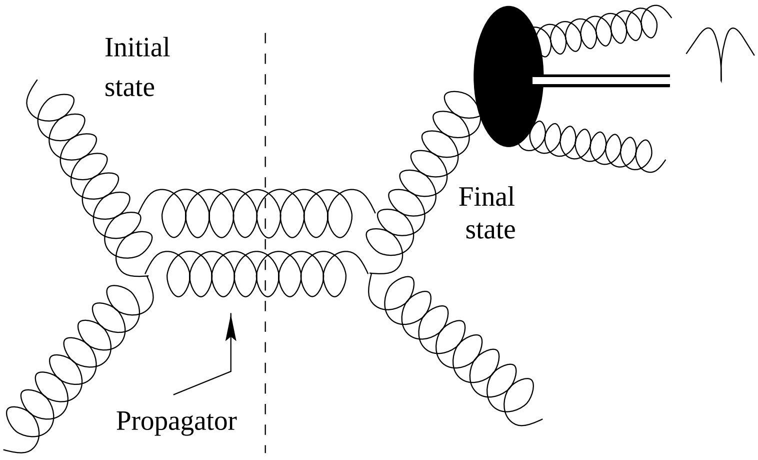

Figure 2.2: Example of Feynman graph illustrating when the factorization of the cross section fails.

It is important to notice that the partonic cross section and the PDFs depend on the arbitrary scale μ_F in such a way that the cross section of heavy-quarkonia production is independent of such scale. However, in (2.2) two scales, μ_R and μ_F are distinguished, that later will be viewed. Nevertheless at this stage it is convenient to say that, in a practical way, both scales are the same, i.e. we can set $\mu_R = \mu_F$.

Besides, there are a lot of uncertainties in (2.2) mainly from four sources

[14] (all will be treated later):

- The heavy-quark mass.
- The size of unknown higher-order corrections.
- Non perturbative effects corresponding to hadronization.
- The value of the QCD scale Λ and the shape of the PDF, both strongly correlated.

From an experimental point of view, heavy quarkonia production (through the predominant colour-octet $Q\overline{Q}$ pairs) reveals that those effects are quite important.

According to the traditional wisdom there are three models of bound state formation: The Colour-singlet Model (CSM), Colour-evaporation Model (CEM), and the one based on the Non-Relativistic QCD, the so called Colour-octet Mechanism (COM).

2.3 Colour-singlet model

In the CSM quarkonium is assumed to be produced at *short distances already in a colour singlet* $Q\overline{Q}$ state with the correct quantum numbers. Hence the cross section is factorized as:

$$\frac{d\sigma[H(J^{PC})](t)}{dt} = F_{nL}\frac{d\sigma[Q\overline{Q}(n^{2s+1}L_J)_1](t)}{dt} \tag{2.3}$$

where $t \equiv x, p_T, ...$ The non perturbative term is F_{nL}, that essentially gives the probability to form the bound state H from the quark pair. The figure 2.3-a) shows the Feynman graph corresponding to the LO quarkonia production from this model. This factor is calculable in terms of the radial wavefunction at the origin or their derivatives, whose values can be obtained from a potential model or from the H decay leptonic widths:

$$F_{nL} \sim \frac{|R_{nL}^{(L)}(0)|^2}{M_H^{3+2L}} \tag{2.4}$$

However, the above cross section (2.3) is dominant only if the relevant momentum scale Q is of the order of the heavy quark mass (as will be seen later). At a larger scale Q, the short distance production is suppressed by a factor $(m/Q)^2$ with respect to production via fragmentation, that we address just below.

At high p_T production one should expect a fall of the cross section of the type $d\sigma/dt \propto 1/p_T^4$ (from very general -dimensional- grounds) pointing out the increasing importance of fragmentation mechanisms (see figure 2.3-b), with respect to $d\sigma/dt \propto 1/p_T^8$ expected according to the colour-singlet fusion mechanism (see figure 2.3-a).

2.3.1 beyond CSM: Fragmentation mechanism

Indeed, fragmentation processes start to dominate $p\overline{p} \to H + X$ at high p_T; then the gluon splitting into a $Q\overline{Q}$ pair becomes important. The kinematic regime for a final state parton, for instance a gluon, hadronizing into heavy quarkonium H occurs when the lab-frame energy E_g of the parton is large but its squared four-momentum is close to the squared mass of the quarkonium $M_H^2 \approx 4m_Q^2$, then

$$\frac{d\sigma[p\overline{p} \to H + X](p_T)}{dp_T} = \int_0^1 dz\, \frac{d\sigma[p\overline{p} \to g(p_T/z) + X](p_T, \mu_R)}{dp_T}\, D_{g\to H}(z, \mu_R, m_Q) \tag{2.5}$$

$D_{g\to H}(z, \mu, m_Q)$ stands for the gluon fragmentation function, and specifies the probability for a parton to hadronize into H as a function of its longitudinal momentum fraction z relative to g; these functions can be evolved through the evolution equations from their "input" scale $\mu_0 = m_Q$ (i.e. evaluated at the energy corresponding to the heavy quark mass; up to the scale

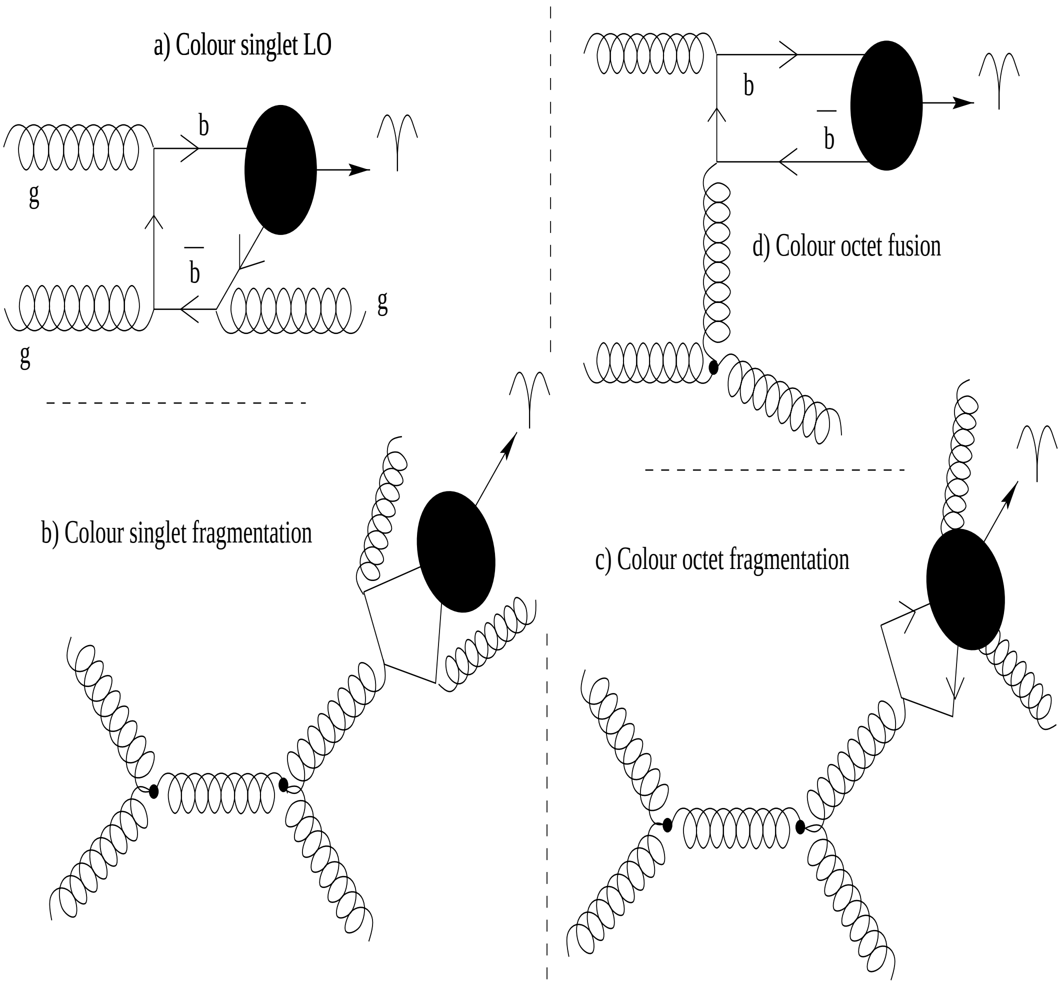

Figure 2.3: Feynman graphs corresponding to the main gg processes in bottomonia production.

μ_R, hence we shall write $D_{g\to H}(z, m_Q, m_Q) \equiv D^{(0)}_{g\to H}(z))$. In the colour-singlet fragmentation mechanism the fragmentation function can be summed in terms of $\alpha_s(m_Q)$ assuming the factorized form as (2.3).

As it has been pointed out previously, in the production differential cross section there are involved, actually, up to three arbitrary scales: The factorization scale μ_F, the renormalization scale μ_R, and the fragmentation scale

μ_{Fr}: The former cancels between the parton distribution and the partonic cross section; μ_{Fr} cancels between the partonic cross section and fragmentation functions; μ_R is the renormalization scale for the running coupling constant. Here, only two are considered: μ_F, μ_R; the practical recipe is to take $\mu_R = \mu_F = m_Q$, where m_Q is the heavy quark mass.

For the case of S-wave resonances, the fragmentation function is

$$D^{(0)}_{g\to\psi_Q}(z) = \left(\frac{\alpha_s(m)}{m}\right)^3 |R_{nS}(0)|^2 f(z) + H.O. \tag{2.6}$$

where $f(z)$ is a calculable function. Figure 2.3-b) shows a Feynman graph corresponding to the colour-singlet fragmentation process in bottomonia production.

However, in the case of the $\underline{P-wave\ resonances(\chi_{QJ})}$ the fragmentation function presents troubles because there is an infrared divergence associated with the soft limit of the final-state gluon. This feature is introduced by means a lower cutoff ϵ_0. We can write in a schematic way this function as

$$D^{(0)}_{g\to\chi_{QJ}}(z) = K_{nP} \times \left[f_1(z) + ln\left(\frac{m}{\epsilon_0}\right)\delta(1-z)\right] \tag{2.7}$$

where K_{nP} is a factor, involving $R'_{nP}(0)$, and $f_1(z)$ denotes calculable functions. An explicit form can be found in [14]. The presence of the infrared term spoils the factorization assumption, then in order to maintain this factorization at least a second non perturbative term must be introduced [15].

$$D^{(0)}_{g\to\chi_{QJ}}(z) = d_1^{(J)}(z,\lambda)\ O_1 + d_8(z)\ O_8(\lambda) \tag{2.8}$$

The first term describes the emission of a perturbative gluon with energy above some cutoff, λ; this cutoff is included keeping the infrared scale ϵ_0. The expressions for d_1, O_1, d_8, O_8 can be found in [14, 15]. In a schematic form

$$\begin{aligned} O_1 &\propto |R'_{nP}(0)|^2 \\ d_1^{(J)}(z,\lambda) &= factor \times \left[f_1(z) + ln\left(\frac{m}{\lambda}\right)\delta(1-z)\right] \end{aligned} \tag{2.9}$$

again $f_1(z)$ stands for calculable functions. The second term contains the infrared scale ϵ_0, showing that actually O_8 has to be considered an additional non perturbative parameter besides $R'_{nP}(0)$.

$$\begin{aligned} O_8(\lambda) &= f(H_1) \times \; ln\left(\frac{\lambda}{\epsilon_0}\right) \\ d_8^{(J)}(z) &\propto \delta(1-z) \end{aligned} \tag{2.10}$$

where $f(H_1)$ essentially is a non perturbative long distance factor associated with the colour singlet mechanism. These results improving the P-wave factorization together with the S-wave one, were compared with the experimental data in charmonia production revealing that this model has discrepancies with the data by a factor ranging from 30 down to 3 at the best (i.e. when the O_8 fragmentation contribution was thought, too optimistically, as the solution to the puzzle of the high production rates). However, a disagreement between CSM rates in bottomonia production and data was found again.

Therefore, since even with the best choice of the P-wave factorization sets the prediction below the data, one must conclude that in the case of S-wave the factorization following the equations (2.3, 2.5) is too naïve. A more generalized factorization of the short-long terms are needed than the one assumed in this model.

Before to go to this goal, an old model, alternative to the CSM, is sketched here, because its theoretical interest is reviving currently.

2.4 Colour-evaporation model

To introduce the main features of this model we shall focus on charmonia production. Essentially this approach makes use of the parton-hadron duality hypothesis to relate the quarkonia cross section to the quark-antiquark one.

According to the CEM, the perturbative cross section for heavy quarkonia coincides with the open heavy quark pair production summed over all spin and colour states. All the information on the non perturbative transition of the $Q\overline{Q}$ pair to quarkonia state H of quantum numbers J^{PC} is contained in the non-perturbative factor $F_{nJ^{PC}}$ that in principle may depend on all quantum numbers. If $\tilde{\sigma}[Q\overline{Q}]$ denotes the total "hidden" cross section of the open heavy quark, calculated by integrating over (in the charmonia case) the $c\overline{c}$ pairs from the invariant mass range up to the mass of the lowest lying heavy-light meson (i.e. from $2m_c$ up to $2m_D$ in the charm case), then

$$\frac{d\sigma[H(J^{PC})](t)}{dt} = F_{nJ^{PC}} \frac{d\tilde{\sigma}[Q\overline{Q}](t)}{dt} \tag{2.11}$$

where $t \equiv x, p_T, ...$ For instance in hadronic collisions the dominant production mechanism is gluon fusion. Hence

$$\begin{aligned} \tilde{\sigma}[c\overline{c}](s) \; &= \; \int_{4m_c^2}^{4m_D^2} d\hat{s} \int dx_1 \; dx_2 f_{g/A}(x_1, m^2) \\ \times \; f_{g/B}(x_2, m^2) &\hat{\sigma}[gg \to (c\overline{c})X](\hat{s})\delta(\hat{s} \; - \; x_1 x_2 s) \end{aligned} \tag{2.12}$$

Notice that the heavy quark pair can be either colour-singlet or colour-octet state. Since we are focusing on gluon fusion, colour-octet is the dominant one. Once the quark pair is produced, the $c\overline{c}$ (in the charm case) configuration arranges itself by interacting with the collision-induced colour field (i.e. interacting with any parton on the neighbourhood). At the same time each member of the $c\overline{c}$ pair interact with others quarks or with its partner, forming charmed mesons or charmonia states, respectively.

In the CEM the essential prediction is that the dynamics of the quarkonium production is that of $\tilde{\sigma}[Q\overline{Q}]$: The energy dependence, x and p_T distributions of the hadrons and of the respective free $Q\overline{Q}$ pair are identical, and when the different states of quarkonia are compared, making ratios of the production cross sections, they should display the independence on p_T and x. This means that the non perturbative factors $F_{nJ^{PC}}$ are universal constants, though maybe depending on the heavy-quark mass. In other words, all the non perturbative effects that lead to the bound state formation cancel if inclusive final states are considered. It must be noticed that the time scale to form a quarkonium state is much larger than the one to produce the quark-pair [16].

Making ratios $\sigma(\chi_c)/\sigma(\psi)$ from this model and comparing with the data the agreement is very good; however there are several weak points:

The CEM does not allow predictions for low p_T quarkonia production [16], since there are different facts to consider (among others, the intrinsic transverse momentum of the initial partons). In addition, at larger p_T, there are higher order perturbative contributions. Thus, since there is no way to disentangle such effects in the low p_T region, the model cannot be predictive.

2.5 Colour-Octet Mechanism

As stressed previously, the CSM fails, on the one hand due to the presence of the infrared divergences in the P-waves that cannot be absorbed in its non perturbative term (see Eq. 2.3). This was previously solved by introducing, more or less by hand, some infrared cut-off as the kinetic energy of the heavy quark inside the meson. However there is a remaining unpleasant ambiguity in this theoretical framework. On the other hand, and more spectacular, the CSM underestimates by more than one order of magnitude the hadroproduction rates of J/ψ and ψ' resonances at Tevatron.

In order to resolve all these difficulties, it has been recently argued that the heavy quark pair not necessarily has to be produced in a colour-singlet state at the short-distance partonic process itself [17]. Alternatively, it can be produced in a colour-octet state evolving non-perturbatively into quarkonium in a specific final state with the correct quantum numbers according to some computable probabilities governed by the internal velocity of the heavy quark. This mechanism, usually named as the colour-octet model (COM) can be cast into the rigorous framework of an effective non-relativistic theory for the strong interactions (NRQCD) deriving from first principles [18, 19, 20]. Thus the NRQCD factorization expresses the cross section for quarkonium production as a sum of terms each of which contains a short-distance (perturbative) factor and a long-distance (non perturbative) matrix element, as we shall see.

2.5.1 NRQCD as an effective theory

Apart from the heavy quark mass scale m_Q, a quarkonium bound state involves (at least) three essential small (compared to m_Q) scales playing a role in the dynamics: Its typical three-momentum $m_Q v$ in the meson rest frame (v is the typical quark three-velocity inside the hadron), the typical kinetic energy $m_Q v^2$, and Λ_{QCD}. The size of the bound state is given by the inverse of the momentum $m_Q v$, while $m_Q v^2$ is the scale of energy splittings between radial excitations and orbital-angular momentum excitations. (Spin splittings are of order $m_Q v^4$ and thus play no significant role in the dynamics, at least up to the current precision of hadroproduction experiments). It is important to remark that v decreases as m_Q increases [18]: Indeed, if m_Q is large enough, v is proportional to the running coupling constant $\alpha_s(M)$, and therefore it decreases asymptotically like $1/ln(m_Q)$; if m_Q is large, then heavy (anti)quark is nonrelativistic, $v << 1$.

In this discussion, it must be assumed that the (anti)quark mass is heavy enough that these scales are well separated:

$$(m_Q v^2)^2 << (m_Q v)^2 << m_Q^2 \tag{2.13}$$

Early estimations showed that $v^2 \sim 0.3$ for charmonia and $v^2 \sim 0.1$ for bottomonia, justifying (at least for bottomonia) this assumption.

Λ_{QCD} is the scale associated with the non perturbative effects involving gluons and light quarks, for instance the long range behaviour of the potential quark-antiquark is approximately linear with a coefficient of $(450 MeV)^2$ [18]; usually, an estimate for the non perturbative scale could be $\Lambda_{QCD} \approx$

$150 - 300$ MeV. For charmonia and bottomonia the first radial excitation and the first orbital-angular-momentum excitation are both around 500 MeV above the ground state. These excitations work following the $m_Q v^2$ scale, then Λ_{QCD} and $m_Q v^2$ are comparable for those cases.

In constructing the NRQCD Lagrangian, starting from full QCD, heavy quarks are described by means of Dirac spinor fields. First an ultraviolet cutoff, Λ, of order m_Q, is introduced explicitly. The introduction of Λ allows to exclude relativistic heavy quarks from the theory, as well as gluons and light quarks with momenta of order m_Q. This recipe is appropriate since the non perturbative physics involves momenta of the order of $m_Q v$ or less.

In a second step, a Foldy-Wouthuysen transformation is used to block diagonalize the Dirac theory so as to decouple the heavy quark and antiquark degrees of freedom. The net effect is that the usual relativistic field theory is replaced by a nonrelativistic Schrödinger field theory, with separate two-component Pauli spinors fields for the heavy quarks and antiquarks. This field theory is NRQCD, its Lagrangian can be written as

$$\mathcal{L}_{NRQCD} = \ \mathcal{L}_{light} \ + \ \mathcal{L}_2 \ + \ \delta\mathcal{L}_2 \ + \ \mathcal{L}_4 \tag{2.14}$$

The gluons and the the n_f flavors of light quarks are described through the fully relativistic Lagrangian

$$\mathcal{L}_{ligth} = \ -\frac{1}{2} tr G_{\mu\nu} G^{\mu\nu} \ + \ \sum_{n_f} \overline{q} i D_\mu \gamma^\mu q \tag{2.15}$$

where $G_{\mu\nu}$ stands for the gluon field-strength tensor expressed in terms of $SU(3)$ matrix, q is the Dirac spinor, $D^\mu = \partial^\mu + ig\ T^a\ A^\mu$ is the usual gauge-covariant derivative ($A^\mu = (\phi, \mathbf{A})$), g the QCD coupling constant, and T^a are the usual $SU(3)_c$ generators. To leading order the heavy quarks and antiquarks are described by

$$\mathcal{L}_2 \ = \ \psi^\dagger \Big(iD_t + \frac{\mathbf{D}^2}{2m_Q} \Big) \psi \ + \ \chi^\dagger \Big(iD_t - \frac{\mathbf{D}^2}{2m_Q} \Big) \chi \tag{2.16}$$

Here ψ is the Pauli spinor field that annihilates a heavy quark, $\chi^\dagger$ is the Pauli spinor field that creates a heavy antiquark, D_t and $\mathbf{D}$ are the time and space components of D^μ respectively; colour indices are implied. The two first terms in the NRQCD Lagrangian describe ordinary QCD coupled to a Schroedinger field theory for the heavy quarks and antiquarks.

Relativistic effects as corrections to $\mathcal{L}_2$ are reproduced through new terms $\delta\mathcal{L}_2$ bilinear in the quark or antiquark field. However some processes need the addition of more terms; for instance, mixed two-fermions operators involving $\psi^\dagger$ and χ (or $\chi^\dagger$ and ψ) correspond to the creation (annihilation) of a $Q\overline{Q}$ pair. Such terms are excluded from the Lagrangian as part of the definition of NRQCD. If such an operator annihilates a $Q\overline{Q}$ pair, by energy conservation, it would have to create gluons (or light quarks) with energies of the order m_Q. In principle the amplitude of annihilation cannot be well described in a nonrelativistic theory as NRQCD; nevertheless the effects of such annihilation can be well described by adding four-fermion operators (as $\psi^\dagger\chi\chi^\dagger\psi$) to the effective Lagrangian in the $\mathcal{L}_4$ piece. The creation operators have the generic form

$$\begin{aligned} O_n^H &= \chi^\dagger\, \mathcal{P}_n\, \psi\, \left(a_H^\dagger a_H\right)\, \psi^\dagger\, \mathcal{P}'_n\, \chi \\ a_H^\dagger a_H &= \sum_{X,m_J} |H\, +\, X> < H\, +\, X| \end{aligned} \tag{2.17}$$

where $a_H^\dagger$ creates the quarkonium H in the out state. The factors $\mathcal{P}_n$ are products of colour matrices, spin matrices and polynomials in the covariant derivatives and fields. The local operator O_n^H creates a point-like $Q\overline{Q}$ pair in the state n, projects onto states that asymptotically include the quarkonium state H, and finally annihilates the $Q\overline{Q}$ pair at the creation point.

The most relevant (6-dimension) operators for heavy quarkonia production included in the $\mathcal{L}_4$ piece are:

$$\begin{aligned}
\mathcal{O}_1^H({}^1S_0) &= \chi^\dagger\psi\left(a_H^\dagger a_H\right)\psi^\dagger\chi, \\
\mathcal{O}_1^H({}^3S_1) &= \chi^\dagger\sigma^i\psi\left(a_H^\dagger a_H\right)\psi^\dagger\sigma^i\chi, \\
\mathcal{O}_8^H({}^1S_0) &= \chi^\dagger T^a\psi\left(a_H^\dagger a_H\right)\psi^\dagger T^a\chi, \\
\mathcal{O}_8^H({}^3S_1) &= \chi^\dagger\sigma^i T^a\psi\left(a_H^\dagger a_H\right)\psi^\dagger\sigma^i T^a\chi,
\end{aligned} \tag{2.18}$$

Besides NRQCD, there are other approaches in order to deal with the phenomenology of heavy quarks. Over the last decade of the century the heavy quark effective field theory (HQEFT) [21] was developed allowing important phenomenological applications in the heavy-light sector of the hadronic physics. Currently there is another attempt to extend this HQEFT deriving a tree level heavy quark effective Lagrangian keeping particle-antiparticle mixed sectors [22] allowing for heavy quark-antiquark creation and annihilation. Briefly, this approach suggests that the $\mathcal{L}_2$ piece of the effective Lagrangian can be written actually as

$$\mathcal{L}_2 = \mathcal{L}_2^{(++)} + \mathcal{L}_2^{(--)} + \mathcal{L}_2^{(+-)} + \mathcal{L}_2^{(-+)}$$

where superindices $(++), (--), (-+), (+-)$ indicate that the tree level QCD Lagrangian is explicitly split into four different pieces corresponding to the particle-particle antiparticle-antiparticle and both particle-antiparticle sectors. It must be noticed that thereby the heavy quark effective fields involved in the operators (2.18) are the same as those appearing in the $\mathcal{L}_2$ piece.

2.5.2 Velocity scaling rules

In order to reproduce full QCD, the NRQCD Lagrangian needs of infinite terms, but if a precision of any order in the typical heavy quark velocity v is required in the practice only a finite number of such terms are needed. The relative importance of a given term is "weighted" by using velocity scaling rules [23] derived by analyzing the equations of motion for the quantum field operators of NRQCD and the scale of momentum ($m_Q v$) and kinetic energy ($m_Q v^2$). Once the typical heavy quark velocity v is obtained (balancing kinetic and potential terms in the equation of motion for the heavy quark field), v can be used as an expansion parameter to analyze the importance of other terms[1]. Table 2.1 summarizes the estimates for the most relevant physical quantities and operators.

Table 2.1: Estimates for the most relevant physical quantities and operators using the velocity scaling rules.

Operator	Estimate
Quark-gluon coupling constant α_s	v
Heavy-quark annihilation field ψ	$(m_Q v)^{3/2}$
Heavy-antiquark creation field χ	$(m_Q v)^{3/2}$
Gauge covariant time derivative D_t	$(m_Q v)^2$
Gauge covariant spatial derivative $\mathbf{D}$	$m_Q v$
Chromoelectric field $g\mathbf{E}$	$m_Q^2 v^3$
Chromomagnetic field $g\mathbf{B}$	$m_Q^2 v^4$
Scalar potential (Coulomb Gauge) $g\phi$	$m_Q v^2$
Vector potential (Coulomb Gauge) $g\mathbf{A}$	$m_Q v^3$

These estimations will drive towards an estimation of the NRQCD matrix elements that are involved in the creation of the heavy quarkonia states (also in the annihilation case), since those elements, as will be seen, contain such operators.

---

[1] Recently, an alternative power counting was suggested in [24] based upon Λ_{QCD}/m instead of v as the expansion parameter

2.5.3 Quarkonium view from NRQCD

The most distinctive feature for the heavy quarkonia phenomenology is that the resonance states can be described as a first approach but quite accurately by means of the quark potential model, in which the quark and antiquark are bound by an instantaneous potential. The validity of this rests upon two assumptions: First, the dominant effect of the exchange of gluons between the quark pair is to produce an instantaneous potential. The most important gluons have momentum of order $m_Q v$ and energies of order $m_Q v^2$. Their off-shellness is thus of order $m_Q v$, which is much greater than the typical kinetic energy of the heavy quark; hence the interaction times are shorter by a factor $1/v$ than the time scale associated with the motion of the heavy quark. Second: The probability of finding dynamical gluons (those which are not part of the potential) is small though not negligible (as we shall argue below), otherwise they would undergo retardation effects.

In the case of heavy quarkonia, in principle, $Q\overline{Q}g$ states are suppressed by a factor v with respect the dominant $Q\overline{Q}$ state in the amplitude and v^2 in the probability. Therefore incorporating such Fock states amounts to a relativistic extension of a (first approximation) non-relativistic model for quarkonia.

Another important feature of the quarkonium structure is its approximate independence of the heavy quark spin, as it can be seen from the NRQCD Lagrangian, that exhibits an approximate spin independence. The leading-order term $\mathcal{L}_2$ is completely independent of the heavy quark spin. The spin dependence enters in the $\delta\mathcal{L}_2$ terms containing Pauli matrices, giving corrections of order v^2.

The total angular momentum J, the charge conjugation C and the parity P, are the exactly conserved numbers in NRQCD as well as in full QCD. then J^{PC} can be used to label the eigenstates $|H>$, as it was established the dominant component in the Fock state expansion of $|H>$ is a pure quark-antiquark state $|Q\overline{Q}>$. The Fock state $|Q\overline{Q}g>$ (with a dynamical gluon present in addition to the quark pair) has an amplitude of order v. Higher Fock states have order v^2 or higher. For a *general* Fock state the $Q\overline{Q}$ pair can be either in a colour singlet or in a colour octet state, its angular-momentum state can be denoted using ${}^{2S+1}L_J$ labels, with parity $P = (-1)^{L+1}$ and, if it is in a colour singlet state, the charge conjugation $C = (-1)^{L+S}$. In the Fock state $|Q\overline{Q}>$ the $Q\overline{Q}$ pair must be in a colour singlet state and in an angular-momentum state ${}^{2S+1}L_J$ that is consistent with the J^{PC} numbers of hadrons. Turning to the Fock $|Q\overline{Q}g>$ state of the meson, here the pair is in a colour octet state. It can be shown that if the $Q\overline{Q}$ is in the dominant Fock state $|Q\overline{Q}>$ with quantum numbers ${}^{2S+1}L_J$, the Fock state $|Q\overline{Q}g>$ has an amplitude of order v only if the $Q\overline{Q}$ pair has total spin S and angular-orbital momentum $L \pm 1$.

Therefore the dynamical gluons can be entered into a Fock state decomposition of physical heavy-quarkonium states following this scheme, grouping the contributions of the same order in v

$$\begin{aligned} |H = n^{2S+1}L_J > = \; & O(1)|Q\overline{Q}(n^{2S+1}L_J^{(1)})> & + \\ & O(v)|Q\overline{Q}(n^{2S+1}(L\pm 1)_{J'}^{(8)})g> & + \\ & O(v^2)|Q\overline{Q}(n^{2S+1}L_J^{(8)})gg> & +... \end{aligned} \tag{2.19}$$

where the superscript added in the spectroscopic notation indicates the colour state.

Now we shall focus on the production process from the NRQCD point of view. When a quarkonium state is produced in a process that involves a momentum transfer Q^2 of order m_Q^2 or larger, the production of the $Q\overline{Q}$ pair that forms the bound state takes place a short distance of order of $1/M$ or smaller. An example explaining this could be the parton process $e^+e^- \to Q\overline{Q}gg$ at leading order in QCD perturbation theory, Q and $\overline{Q}$

having momenta $P/2+p$ and $P/2-p$, where the relative three-momentum $\mathbf{p}$ must be of the order $m_Q v$ in the $\mathbf{P}=0$ frame in order for the $Q\overline{Q}$ pair to have a significant probability to form the bound state H. The amplitude for the production of the $Q\overline{Q}$ pair is insensitive to changes in the relative four-momentum p that are much less than m_Q, and therefore the quark and the antiquark are produced with a separation $1/m_Q$ or less. In the framework of the NRQCD the effect of the short distance (perturbative) part of a production amplitude is simply to create a $Q\overline{Q}$ pair at a space-time point. The formation of the quarkonium state H from the $Q\overline{Q}$ takes place over distances that are of order $1/m_Q v$ or larger in the quarkonium rest frame, and so it is described accurately by NRQCD. As it was explained above, in this theory the production (and annihilation) processes are described by means of the four fermions operators. Then given that the long distance (non perturbative) part of the production rate can be expressed in terms of the vacuum matrix elements of O_n^H operators, the *inclusive* cross section for quarkonium production in the quarkonium rest frame can be written as

$$\sigma(H) \;=\; \sum_n \frac{F_n(\Lambda)}{M^{d_n-4}} \;<0|\; O_n^H(\Lambda)\; |0> \qquad (2.20)$$

F_n are short distance coefficients calculated in perturbative QCD by expanding the production amplitude in powers of α_s and the relative momentum $\mathbf{p}$; Λ is a scale which separates the short and long distance effects. However the cross section is indeed independent of Λ as its dependence is compensated by the Λ dependence of its corresponding non perturbative matrix element $<0|O_n^H(\Lambda)|0>$. To extract the value of some relevant matrix elements in a phenomenological way is, precisely, one of the main goals in this work. Figures 2.3-c-d) illustrate the main gg colour-octet Feynman diagrams.

As pointed out previously, the NRQCD factorization approach is a systematic framework to analyze annihilation decay rates and inclusive production cross section for heavy quarkonia. However for the production case the level of rigor of these arguments is comparable to that in the proofs of factorization for the Drell-Yan process for lepton pair production in hadronic collisions [18].

On the other hand, one must be aware that this factorization formula has a double expansion: in α_s for the short distance term and in v for the long distance one, the relative importance of each non perturbative matrix element is determined by its order in v.

To finish this brief sketch, some additional results from this model, focusing on this work, are shown:

- The relevant quarkonia matrix elements in the colour singlet state can be expressed in terms of their corresponding squared radial wavefunctions (or their derivatives for the P waves)

$$< O_1^{\Upsilon(nS)}(^3S_1) > = \frac{9}{2\pi}|R_n(0)|^2 \tag{2.21}$$

$$< O_1^{\chi_{bJ(nP)}}(^3P_J) > = \frac{9}{2\pi}(2J+1)|R_n'(0)|^2 \tag{2.22}$$

- Heavy-quark spin symmetry implies approximate relations between matrix elements for the various spin states of a given radial and orbital excitation of heavy quarkonium. The leading violations of heavy-quark spin symmetry come from spin-flip terms in $\delta\mathcal{L}_2$, whose effects are of relative order v^2. Hence, the equalities that follow from heavy-quark spin symmetry hold only at leading order in v^2. The main advantage is that, using this symmetry, the number of independent matrix elements can be significantly reduced. For instance, up to corrections of relative order v^2 we have

$$< O_8^{\chi_{bJ}}(^3S_1) > = (2J+1) < O_8^{\chi_{b0}}(^3S_0) > \tag{2.23}$$

- Using the velocity scaling rules we can to establish “a priori” the scaling order of each matrix element, taking into account the estimation in v of each operator entering in the matrix element. The Table 2.2, from [25], summarizes the results for the most relevant ones in this work: $\Upsilon(nS)$ $(n = 1, 2, 3)$and $\chi_{bJ}(nP)$ $(n = 1, 2)$.

Table 2.2: Most relevant matrix elements using velocity scaling rules.

Matrix element	NRQCD scaling order
$< 0\|O_1^{\Upsilon(nS)}({}^3S_1)\|0 >$	$(m_b v)^3$
$< 0\|O_1^{\chi_{bJ}(nP)}({}^3P_1)\|0 >$	$(m_b v)^5$
$< 0\|O_8^{\Upsilon(nS)}({}^3S_1)\|0 >$	$m_b^3 v^7$
$< 0\|O_8^{\chi_{bJ}(nP)}({}^3P_1)\|0 >$	$m_b^3 v^5$

Chapter 3

The $\Upsilon(nS)$ parameters in the Generation.

In this chapter, a description of some characteristics of the bottomonia family below the open bottom production threshold is provided, including $\Upsilon(nS)$ (n=1,2,3) and $\chi_{bJ}(nP)$ resonances. They will play a role in the bottomonia inclusive decays when adjusting the values of the NRQCD matrix elements in the fit to the TEVATRON data [7]. Standard masses for resonances are set when running PYTHIA in order to have a realistic event generation, although in the derivation of the theoretical expression for the production amplitudes the approximate mass of the resonance $\simeq 2m_b$ was used. Branching Ratios, CSM (and also the COM) parameters used in such generations also will be shown. All of those settings put on the right track in fitting the NRQCD matrix elements. Then, a discussion follows about how the higher order QCD effects have been considered; a brief presentation of PYTHIA and JETSET environment and physical issues is also shown. The chapter ends with the explanation of how COM was implemented in PYTHIA, and a detailed discussion of the procedures to fit the experimental data.

3.1 The $\Upsilon(nS)$ family

The following resonances were generated, considering different production sources:

- $\boxed{\Upsilon(1S)}$

- CSM contribution:
  - $\Upsilon(1S)$ direct production
  - $\Upsilon(2S)$ and $\Upsilon(3S)$ followed by strong and electromagnetic decays
  - $\chi_{bJ}(1P)$ and $\chi_{bJ}(2P)$ followed by electromagnetic decays
- COM contribution:
  - $(^3S_1)_{COM}$ contribution: We consider gg, gq and qq as a partonic channels (see also section 3.4 and appendix A for more details).
    - $\Upsilon(1S)_{COM}$ direct production and $\Upsilon(2S)_{COM} + \Upsilon(3S)_{COM}$ decays
    - $\chi_{bJ}(1P)_{COM}$ and $\chi_{bJ}(2P)_{COM}$ decays
  - $(^1S_0)_{COM}$
  - $(^3P_J)_{COM}$

where $\Upsilon(nS)_{COM}$ denotes the resonance produced through the COM mechanism. Some of the above contributions will be ultimately dismissed in the fit to experimental data, as explained later.

- $\boxed{\Upsilon(2S)}$

- CSM contribution:
  - $\Upsilon(2S)$ direct production
  - $\Upsilon(3S)$ followed by strong and electromagnetic decay
  - $\chi_{bJ}(2P)$ followed by electromagnetic decay
- COM contribution. For these contributions, as above:
  - $({}^3S_1)_{COM}$ contribution: gg-gq-qq channels
    - $\Upsilon(2S)_{COM}$ direct production and $\Upsilon(3S)_{COM}$ decay
    - $\chi_{bJ}(2P)_{COM}$ decay
  - $({}^1S_0)_{COM}$
  - $({}^3P_J)_{COM}$

- $\boxed{\Upsilon(3S)}$

- CSM contribution:
  - $\Upsilon(3S)$ direct production
- COM contribution:
  - $({}^3S_1)_{COM}$ contribution: gg-gq-qq channels
    - $\Upsilon(3S)_{COM}$ direct production
  - $({}^1S_0)_{COM}$
  - $({}^3P_J)_{COM}$

As can be seen, $\chi_{bJ}(3P)$ resonances will not be taken into account in the generation, since currently there are no experimental evidences for their existence; nevertheless as a check this contribution was introduced in a preliminary study, turning out that if these feed-down sources were added to the fit, the CSM part by itself alone would stand clearly above the experimental points in the low and relatively low p_T region of the differential cross section (manifestly pointing out its unnecessary contribution).

In the $\Upsilon(1S)$ case, the diverse CSM sources are introduced separately in the generation, since there is experimental information about separated sources of the production of this resonance from Tevatron data [9]; hence a check can be performed in the generation, as explained later.

We can distinguish in the COM generation two main contributions: $(^3S_1)_8$ and $(^1S_0)_8 + (^3P_J)_8$. The reason to consider jointly the latest two sources is that the differences in shape between the $^1S_0^{(8)}$ and $^3P_J^{(8)}$ contributions were not sufficiently great to justify independent generations for them, as later explained.

For the $\Upsilon(2S)$ and $\Upsilon(3S)$ cases the procedure was the same as for the COM sources, whereas all the CSM channels were generated together since there is no experimental data about separated production sources so far.

3.2 Parameters

3.2.1 The Matrix Elements

Now we present the procedure followed in the choice for the "fixed" parameters used in our study and the determination of the set of values of the NRQCD matrix elements (MEs). As explained in the previous chapter, the $\Upsilon(nS)$ production cross sections are proportional to those MEs, so that it becomes possible to extract their values from the experimental data, being that one of the goals of this work.

The production differential cross section can be written as a sum of all contributions in the following way

$$\frac{d\sigma}{dp_t}|_{TOTAL} = A_1 \; < O_1^{\Upsilon(nS)}(^3S_1) > |_{tot} \; + \; A_2 \; < O_1^{\chi_{bJ}(nP)}(^3P_1) > |_{tot} \; + \\ B_1 \; < O_8(^3S_1) > |_{tot} \; + \; B_2 \; < O_8(^1S_0) > |_{tot} \; + \; B_3 \; < O_8(^3P_J) > |_{tot} \tag{3.1}$$

where the A_i, B_i factors include the short distance term and some other numerical factors belonging to the long distance part. The CSM MEs are considered as "fixed" parameters, while the COM parameters are taken as free to be adjusted from the fit.

Those MEs are taken as follows:

Colour-singlet parameters (from [26]):

- $< O_1^{\Upsilon(nS)}(^3S_1) > |_{tot}$, defined as

$$< O_1^{\Upsilon(nS)}(^3S_1) > |_{tot} \; = \; \sum_{m\geq n}^{3} \; < O_1^{\Upsilon(mS)}(^3S_1) > Br[\Upsilon(mS)\to\Upsilon(nS)X]$$

- $< O_1^{\chi_{bJ(nP)}}(^3P_J) > |_{tot}$, that for each J, defined as

$$< O_1^{\chi_{bJ(nP)}}(^3P_J) > |_{tot} \; = \; \sum_{m\geq n}^{2} \; < O_1^{\chi_{bJ(mP)}}(^3P_J) > Br[\chi_{bJ}(mP)\to\Upsilon(nS)X]$$

where Br stands for the Branching Ratio of those decay channels explicitly shown above. It is understood that $Br[n\to n] \; = \; 1$.

Actually, in the PYTHIA generation the inputs of the CSM parameters are the radial wave functions at the origin (or their derivatives), that can be related to the above matrix elements, as pointed out in the previous chapter,

$$< O_1^{\Upsilon(nS)}(^3S_1) > = \; \frac{9}{2\pi}|R_n(0)|^2 \tag{3.2}$$

$$< O_1^{\chi_{bJ(nP)}}(^3P_1) > = \; \frac{9}{2\pi}(2J+1)|R_n'(0)|^2 \tag{3.3}$$

whose numerical values were obtained from a Buchmüller-Tye potential model tabulated in [27].

Colour-octet long-distance parameters to be extracted from the fit:

- $< O_8^{\Upsilon(nS)}(^3S_1) > |_{tot}$, defined as

$$< O_8^{\Upsilon(nS)}(^3S_1) > |_{tot} \;=\; \sum_{m\geq n}^{3} < O_8^{\Upsilon(mS)}(^3S_1) > Br[\Upsilon(mS)\rightarrow\Upsilon(nS)X] + \sum_{m\geq n}^{2}\sum_{J=0}^{2} < O_8^{\chi_{bJ}(mP)}(^3S_1) > Br[\chi_{bJ}(mP)\rightarrow\Upsilon(nS)X] \tag{3.4}$$

- $< O_8^{\Upsilon(nS)}(^1S_0) > |_{tot}$, defined as

$$< O_8^{\Upsilon(nS)}(^1S_0) > |_{tot} \;=\; \sum_{m\geq n}^{3} < O_8^{\Upsilon(mS)}(^1S_0) > Br[\Upsilon(mS)\rightarrow\Upsilon(nS)X] \tag{3.5}$$

- $< O_8^{\Upsilon(nS)}(^3P_J) > |_{tot}$, defined as

$$< O_8^{\Upsilon(nS)}(^3P_J) > |_{tot} \;=\; \sum_{m\geq n}^{3} < O_8^{\Upsilon(mS)}(^3P_J) > Br[\Upsilon(mS)\rightarrow\Upsilon(nS)X] \tag{3.6}$$

On the other hand, as above mentioned, the differences in shape between the $^1S_0^{(8)}$ and $^3P_J^{(8)}$ contributions were not sufficiently great to justify independent generations for them. In fact, temporarily setting $< O_8^{\Upsilon(1S)}(^3P_0) >= m_b^2 < O_8^{\Upsilon(1S)}(^1S_0) >$ and defining the ratio

$$r(p_T) \;=\; \frac{\sum_{J=0}^{2}\frac{d\sigma}{dp_T}[^3P_J^{(8)}]}{\frac{d\sigma}{dp_T}[^1S_0^{(8)}]} \tag{3.7}$$

it is found $r \simeq 5$ as a mean value over the $[0,20]$ GeV p_T-range. Actually the above ratio is not steady as a function of the $\Upsilon(1S)$ transverse momentum. Therefore in the generation we split the p_T region into two domains: for $p_T \leq 6$ GeV we set $r = 6$ whereas for $p_T > 6$ GeV we set $r = 4$.

In summary, only the ${}^1S_0^{(8)}$ channel will be generated but rescaled by the factor r to incorporate the ${}^3P_J^{(8)}$ contribution. Consequently, in analogy to [25] we shall consider only the combination of the colour-octet matrix elements:

$$M_5 \; = \; 5 \times \left(\frac{< O_8^{\Upsilon(1S)}({}^1S_0) > |_{tot}}{5} + \frac{< O_8^{\Upsilon(1S)}({}^3P_0) > |_{tot}}{m_b^2} \right) \qquad (3.8)$$

3.2.2 More about $\Upsilon(nS)$ parameters: Masses and Branching ratios

First of all, it is worth to point out that the Tevatron data [7] present the measured cross sections as $(d^2\sigma/dp_T dy) \times Br(\Upsilon \to \mu^+\mu^-)$ for values of the Υ rapidity $|y| < 0.4$. In our study we will generate Υ's, and the following muonic branching ratios will be used

- $BR[\Upsilon(1S) \to \mu^+\mu^-] = 2.48$ % ([8])
- $BR[\Upsilon(2S) \to \mu^+\mu^-] = 1.31$ % ([8])
- $BR[\Upsilon(3S) \to \mu^+\mu^-] = 1.81$ % ([8])

Moreover, we shall impose the same kinematic constraint in the rapidity cut as in the experimental points. It is important to stress that PYTHIA provides the absolute normalization of the histograms, once all the parameters are set, allowing to apply a convenient "renormalization" factor to the total cross section provided by PYTHIA. Such a factor takes into account the rapidity cut, and the BR $\Upsilon \to \mu^\pm$, as we shall see in the next chapter.

On the other hand, there is also the problem of the masses: Usually in the literature on quarkonia production using the models mentioned before, the theoretical mass of the Υ and χ_b resonances is set as $2m_b$, twice the b-quark mass; nevertheless there is a kinematic dependence of the cross sections on the masses, forcing us to distinguish, depending on each case.

- $\Upsilon(1S)$

  As already explained, for this resonance there are contributions from direct production and decays from the $\Upsilon(2S)$, $\Upsilon(3S)$, $\chi_{bJ}(1P)$ and $\chi_{bJ}(2P)$.

  The mass value for $\Upsilon(1S)$ is 9.46 GeV [8], but putting $2m_b = 9.76$ GeV implies an error of $\sim 3\%$ w.r.t the former value, however the latter value is consistent with the formation of the coloured intermediate state. For the $\Upsilon(2S)$ and $\Upsilon(3S)$ cases, as their contributions are jointly generated, their common value could be set weighing their masses. Nevertheless their contribution in the decay to $\Upsilon(1S)$ is too low to justify their modification. Indeed, setting $2m_b$ yields an error less than 3% with respect to its averaged mass. A weighted mean of the $\chi_{bJ}(nP)$ is done for such resonances, taking into account the branching ratios of their decays.

- $\Upsilon(2S)$
  In this case there is direct $\Upsilon(2S)$ production in addition to the decays from the $\chi_{bJ}(2P)$ and $\Upsilon(3S)$. Their channels are generated separately, and standard masses [8] are set for each contribution.

- $\Upsilon(3S)$
  This case is the cleanest one since there is only direct production (there are not $\chi_{bJ}(3P)$ to consider) and its mass, from [8], can be used.

3.3 Higher Order QCD effects

The following higher order QCD effects on the partonic cross sections are considered:

- Intrinsic Fermi motion of partons inside hadrons.
- Multiple emission of gluons in the initial state following DGLAP evolution.
- Altarelli-Parisi evolution of the splitting gluon in the following channels
  $gg \rightarrow (g^* \rightarrow b\bar{b})g$
  $gq \rightarrow (g^* \rightarrow b\bar{b})q$

3.3.1 Intrinsic Fermi motion of partons inside the hadrons and gluon radiation

It is well-known for a long time that higher-order effects (K factors, standing for $K = \sigma_{NLO}/\sigma_{LO}$) play an important role in inclusive hadroproduction. In particular, beyond the primordial transverse momentum k_T of partons in hadrons related to Fermi motion relevant at small p_T, initial-state radiation of gluons by the interacting partons add up to yield an *effective* intrinsic transverse momentum which certainly has to be considered in hadroproduction at high p_T. If overlooked at all, the effect on the fit parameters (and ultimately on the colour-octet MEs) amounts to a *systematic* overestimate [28]. In fact this effect can be represented by a K factor depending on p_T, i.e. $K(p_T)$ parameterized as in [29].

Actually, one should distinguish the primordial transverse momentum of partons owing to their Fermi motion (a non-perturbative effect) from the perturbative contribution dynamically generated via gluon radiation, generally implemented in the event generators by means of a parton shower algorithm following DGLAP evolution. By *effective* k_T we merge both effects under a common name, though the former is actually overshadowed by the latter at high p_T. This effect causes that the predicted curve stands well above the experimental data, in accordance with the expected "k_T-kick" caused by the *effective* intrinsic transverse momentum of partons. Accordingly, keeping radiation effects in the theoretical analysis it will turn out that the values for the colour-octet MEs have to be lowered by a significant amount. Of course, the PYTHIA treatment of the effective k_T is not guaranteed to be perfect but, nevertheless, should give a reasonable estimate of such effects.

Although the discrepancies between the CSM and experimental cross sections on bottomonia hadroproduction are smaller than those found for charmonia, still some extra contribution should be invoked to account for the surplus observed at the Fermilab Tevatron. However, we find that, those matrix elements (MEs) determined from Tevatron data in other analysis [25] have to be lowered once initial-state radiation of gluons is taken into account. This is because of the raise of the (*effective*) intrinsic momentum (k_T) of the interacting partons enhancing the moderate and high-p_T tail of the differential cross section for heavy quarkonia production [28]. This effect, as generated by the appropriate PYTHIA algorithm [30, 31], is more pronounced - and likely more sound from a physical viewpoint - than a pure Gaussian smearing with a (required) large $< k_T >$ value. Besides PYTHIA, in smoothing the production cross section, endows us with the possibility of extending our analysis to the small p_T region of bottomonium production.

Aside, we will also include the final-state radiation mechanism in this study: It should be noted that initial-state radiation and final-state radiation have opposite effects in the p_T spectrum, the former enhancing the high p_T tail whereas the latter softens the distribution. Indeed, in considering the process $gg \to J/\psi g$ in PYTHIA only the gluon evolves in the final state, though the energy (and momentum) of quarkonium is modified as a consequence of the final-state machinery [30] are switched on.

3.3.2 Gaussian $< k_T >$ smearing

The smearing effect on the differential cross section caused by initial-state radiation of gluons can be roughly simulated by means of a gaussian intrinsic k_T distribution of the interacting partons inside hadrons, to be convoluted with the corresponding hard interaction cross sections:

$$D(\mathbf{k_T}) \ = \ \frac{1}{\pi\sigma^2} \exp\left(-\frac{k_T^2}{\sigma^2}\right) \tag{3.9}$$

with

$$< k_T > = \int k_T \ D(\mathbf{k_T}) \ d\mathbf{k_T} = \int_0^\infty k_T \ D(\mathbf{k_T}) 2\pi k_T \ dk_T = \frac{\sqrt{\pi}}{2} \ \sigma \tag{3.10}$$

The width of the gaussian can be viewed as an adjustable parameter [32]. In fact, as will be seen, PYTHIA incorporates as an option a gaussian primordial k_T smearing, whose width can be set by the user. Once the matrix elements will be obtained this possibility will be used to make a “new” fit of Tevatron data for the Υ resonances, employing the same matrix elements obtained activating the initial-state radiation PYTHIA algorithm, but with initial-state radiation off. Then the gaussian k_T smearing has to simulate the (this time missing) initial-state radiation. This feature will be employed in the discussion of the prospect to probe the gluon density using heavy quarkonia production.

3.3.3 Altarelli-Parisi evolution of the splitting gluon

According to the colour-octet mechanism, gluon fragmentation becomes the dominant source of heavy quarkonium direct production at high transverse momentum. On the other hand, Altarelli-Parisi (AP) evolution of the splitting gluon into $(Q\overline{Q})$ produces a depletion of its momentum and has to be properly taken into account. If not so, the resulting long-distance parameter for the ${}^3S_1^{(8)}$ channel would be underestimated from the fit [33].

The key idea is that the AP evolution of the fragmenting gluon is performed from the evolution of the *gluonic partner* of quarkonium in the final-state of the production channel

$$g\ +\ g \to g^{*}(\to(Q\overline{Q})[^{3}S_{1}^{(8)}])\ +\ g \tag{3.11}$$

Let us remark that, in fact, g^{*} is not generated in the new code . Final hadronization into a $(Q\overline{Q})$ bound state is taken into account by means of the colour-octet matrix elements multiplying the respective short-distance cross sections. Nevertheless, it is reasonable to assume that, on the average, the virtual g^{*} should evolve at high p_T similarly to the other final-state gluon - which actually is evolved by the PYTHIA machinery. We used this fact to simulate the (expected) evolution of the (ungenerated) g^{*} whose momentum was assumed to coincide with that of the resonance (neglecting the effect of emission/absorption of soft gluons by the intermediate coloured state bleeding off colour [34]).

Therefore, event by event we get a correcting factor to be applied to the transverse mass of the $(Q\overline{Q})$ state (for the $^{3}S_{1}^{(8)}$ channel only):

$$x_{AP}\ =\ \frac{\sqrt{p_T^{*2}+m_{(Q\overline{Q})}^{2}}}{\sqrt{p_T^{2}+m_{(Q\overline{Q})}^{2}}} \tag{3.12}$$

where p_T (p_T^{*}) denotes the transverse momentum of the final-state gluon without (with) AP evolution and $m_{(Q\overline{Q})}$ denotes the mass of the resonance. At high p_T,

$$p_T^{AP}\ =\ x_{AP}\times p_T \tag{3.13}$$

where p_T is the transverse momentum of the resonance as generated by PYTHIA (i.e. without AP evolution), whereas for $p_T \leq m_{(Q\overline{Q})}$ the effect becomes much less significant as it should be. Thus the interpolation between low and high p_T is smooth with the right asymptotic limits at both regimes. The above way to implement AP evolution may appear somewhat simple but it remains in the spirit of our whole analysis, i.e. using PYTHIA machinery whenever possible.

On the other hand there is the channel which also has to incorporate AP evolution:

$$g \;+\; q \to g^*(\to(Q\overline{Q})[^3S_1^{(8)}]) \;+\; q \tag{3.14}$$

Since here there is not a gluonic partner it cannot be used the procedure before employed to simulate the AP evolution - a quark does not evolves in the same way as a gluon-. Therefore the simplest way to simulate such evolution (holding the same spirit as above) is to consider the AP correction corresponding to the former case as a p_T dependent factor to be applied in this channel. Since the relative importance of this contribution is not very large, we expect that our approach is reliable enough.

In the following sections more details about the generation, PYTHIA routines, implementation of the COM in such routines, fit to the Tevatron data, etc, are presented.

3.4 Implementation of the COM in PYTHIA

Here we present the physics underlying the generation: Different channels, their cross sections, and the main lines of the code. More details can be found in the appendix A, when we give the main technical points regarding our event generation.

Originally, the event generator PYTHIA [30] produces direct J/ψ's and higher χ_{cJ} resonances in hadron-hadron collisions according to the CSM. For instance, its corresponding squared amplitude for the $^3S_1^{(1)}$ reads

$$\begin{aligned} \overline{\sum}\ |\mathcal{A}(gg\to[^3S_1^{(1)}]g)|^2 \ &= \ \frac{5\pi^2\alpha_s^3}{9M\hat{s}^2}\,\frac{M^2}{[(\hat{s}-M^2)(\hat{t}-M^2)(\hat{u}-M^2)]^2} \\ \times \ &\Big([\hat{s}^2(\hat{s}-M^2)^2] + \ [\hat{t}^2(\hat{t}-M^2)^2] + \ [\hat{u}^2(\hat{u}-M^2)^2]\Big)\ |R(0)|^2 \end{aligned} \tag{3.15}$$

where $|R(0)|^2$ stands for the squared wavefunction at the origin. The other CSM contributions can be also found in Ref. [35].

In principle the only thing to do is to redefine masses and other parameters, bringing these expressions in accordance with the bottomonia case. However, as already mentioned this model fails off to account for the bottomonia production rate at the Fermilab Tevatron. Consequently, a code is implemented in PYTHIA in order to include the colour-octet mechanism for Υ hadroproduction channels via the following α_s^3 partonic processes:

- $g + g \rightarrow \Upsilon + g$
- $g + q \rightarrow \Upsilon + q$
- $q + \bar{q} \rightarrow \Upsilon + g$

In the simulation the ${}^3S_1^{(8)}$, ${}^1S_0^{(8)}$ and ${}^3P_J^{(8)}$ $(J = 0, 1, 2)$ states in ${}^3S_1$ bottomonia hadroproduction according to the COM are included. The squared amplitudes, taken from Refs. [25, 36] are reproduced below. Firstly let us consider the ${}^3S_1^{(8)}$ intermediate state:

$$\begin{aligned}
\overline{\sum}|\mathcal{A}(gg\rightarrow\Upsilon g)|^2 &= -\frac{8\pi^3\alpha_s^3}{9M^3}\,\frac{27(\hat{s}\hat{t}+\hat{t}\hat{u}+\hat{u}\hat{s})-19M^4}{[(\hat{s}-M^2)(\hat{t}-M^2)(\hat{u}-M^2)]^2} \\
&\times\ [(\hat{t}^2+\hat{t}\hat{u}+\hat{u}^2)^2-M^2(\hat{t}+\hat{u})(2\hat{t}^2+\hat{t}\hat{u}+2\hat{u}^2) \\
&+\ M^4(\hat{t}^2+\hat{t}\hat{u}+\hat{u}^2)]\ <0|O_8^{\Upsilon}({}^3S_1)|0> \qquad (3.16)
\end{aligned}$$

$$\begin{aligned}
\overline{\sum}|\mathcal{A}(gq\rightarrow\Upsilon q)|^2 &= -\frac{16\pi^3\alpha_s^3}{27M^3}\,\frac{\hat{s}^2+\hat{u}^2+2M^2\hat{t}}{\hat{s}\hat{u}(\hat{t}-M^2)^2} \\
&\times\ [4(\hat{s}^2+\hat{u}^2)-\hat{s}\hat{u}]\ <0|O_8^{\Upsilon}({}^3S_1)|0>
\end{aligned} \qquad (3.17)$$

$$\begin{aligned}
\overline{\sum}|\mathcal{A}(q\bar{q}\rightarrow\Upsilon g)|^2 &= \frac{128\pi^3\alpha_s^3}{81M^3}\,\frac{\hat{t}^2+\hat{u}^2+2M^2\hat{s}}{\hat{t}\hat{u}(\hat{s}-M^2)^2} \\
&\times\ [4(\hat{t}^2+\hat{u}^2)-\hat{t}\hat{u}]\ <0|O_8^{\Upsilon}({}^3S_1)|0>
\end{aligned} \qquad (3.18)$$

where the barred summation symbol refers to an average over initial and final spins and colours; $\hat{s}$, $\hat{t}$ and $\hat{u}$ stand for the Mandelstam variables of the short-distance subprocesses. We shall set the masses for Υ resonances following the recipe commented before; these assumptions are in accordance with the non-relativistic nature of heavy quarkonium supposed in the theoretical calculation of these amplitudes, i.e. vanishing relative momentum of the quarks in the bound state. Moreover, they correspond to the degree of accuracy followed in our study.

The corresponding expressions for the ${}^1S_0^{(8)}$ contributions are:

$$\begin{aligned}\overline{\sum}|\mathcal{A}(gg\to\Upsilon g)|^2 &= \frac{20\pi^3\alpha_s^3}{M}\,\frac{(\hat{s}^2-M^2\hat{s}+M^4)^2-\hat{t}\hat{u}(2\hat{t}^2+3\hat{t}\hat{u}+2\hat{u}^2)}{\hat{s}\hat{t}\hat{u}[(\hat{s}-M^2)(\hat{t}-M^2)(\hat{u}-M^2)]^2}\\ &\times\ [\hat{s}^2(\hat{s}-M^2)^2+\hat{s}\hat{t}\hat{u}(M^2-2\hat{s})+(\hat{t}\hat{u})^2]\ <0|O_8^{\Upsilon}({}^1S_0)|0> \end{aligned} \tag{3.19}$$

$$\overline{\sum}|\mathcal{A}(gq\to\Upsilon q)|^2 = -\frac{40\pi^3\alpha_s^3}{9M}\,\frac{\hat{s}^2+\hat{u}^2}{\hat{t}(\hat{t}-M^2)^2}\ <0|O_8^{\Upsilon}({}^1S_0)|0> \tag{3.20}$$

$$\overline{\sum}|\mathcal{A}(q\bar{q}\to\Upsilon q)|^2 = \frac{320\pi^3\alpha_s^3}{27M}\,\frac{\hat{t}^2+\hat{u}^2}{\hat{s}(\hat{s}-M^2)^2}\ <0|O_8^{\Upsilon}({}^1S_0)|0> \tag{3.21}$$

With regard to the ${}^3P_J^{(8)}$ contributions, they display altogether a similar (i.e. degenerate) transverse momentum behaviour as the ${}^1S_0^{(8)}$ component for $p_t \geq 5$ GeV. Thus from a pragmatic point of view, the generation of bottomonia via intermediate P-wave coloured states becomes superfluous although their possible contribution must properly be taken into account in the computation of the overall cross section, as explained in section 3.2.1.

The differential cross sections of the $O(\alpha_s^3)$ scattering processes, considering the above-mentioned amplitudes, are obtained as

$$\frac{d\hat{\sigma}}{d\hat{t}}(ab\to\Upsilon c) = \frac{1}{16\pi\hat{s}^2}\,\overline{\sum}|\mathcal{A}(ab\to\Upsilon c)|^2 \tag{3.22}$$

All these implementations were included as new codes in the Pysigh routines: The COM $g + g \to \Upsilon + g$ was implemented as new code in the "old" PYTHIA routine for the colour-singlet production routine (previously modified to become CSM Υ production). The $g + q \to \Upsilon + q$ and

$q+\bar{q}\rightarrow\Upsilon+g$ channels will be reproduced deriving from an already existing routine, based on the Higgs production channels from partons (see Appendix A) redefining the Higgs mass to be the the resonance one, and including their corresponding cross sections according to the previous equations (3.17-3.18) and (3.20-3.21) considering only the muonic decay channel for this "fake" Higgs.

3.5 Strategy for the extraction of the NRQCD Matrix Elements

This section is devoted to the discussion of the method used in the fit of the $({}^3S_1)_8$ and $({}^1S_0)_8+({}^3P_J)_8$ MEs. Essentially a best χ^2 fit will be carried out. A procedure following from the definition of the χ^2 will be applied. Besides, a theoretical curve will be obtained from the histograms generated with the optimized parameters.

To perform those fits we used CTEQ4L and CTEQ2L PDFs; details and references about such PDFs can be found in Appendix C.

Whenever a Υ histogram is obtained (It must be noticed that such histograms are proportional to their corresponding NRQCD Matrix Elements), actually several contributions are considered; for example in the $\Upsilon(1S)$ case:

- CSM contribution ($\Upsilon(1S)_{direct}$, $\Upsilon(2S)$, $\Upsilon(3S)$ and $\chi_{bJ}(nP)$ feed-down), we will design the sum of these channels under a common label "c"; c_i stands for the CSM contribution at the i-th bin.

- COM contribution:

  - $({}^3S_1)_{COM}$ contribution: $gg-gq-qq$ channels whose sum is named as "q"; q_i stands for the $({}^3S_1)_8$ contribution at the i-th bin.

- $(^1S_0)_8 + (^3P_J)_8$ contribution: As will be discussed, this channel will not be needed in CTEQ4L fit, and their corresponding matrix elements in the CTEQ2L case are very small (near to zero). Therefore in the CTEQ4L case this contribution does not appear; in the CTEQ2L one this channel is named as "t"; t_i stands for its contribution at the i-th bin.

If H stands for the sum over all contributions (that is, the differential cross section × B. Ratio), and H_k corresponds to the value at the k-th bin, the latter can be written as

$$H_k = c_k \ + \ b\ q_k \ + \ a\ t_k \tag{3.23}$$

where "a" and "b" are the free parameters as we shall explain just below:

The key idea is to consider the CSM as a fixed contribution whereas the COM contributions have free parameters (a and b) that are "tuned" until the whole histogram would match the experimental points (i.e. best χ^2 fit, meaning χ^2 required to be minimal). The figure 3.1 illustrates a typical situation for the CTEQ2L case.

It is very important to emphasize that the $(^3S_1)_8$ contribution is definitely needed in the CTEQ4L case to fit the large p_T experimental points; on the contrary, as already mentioned, the $(^1S_0)_8 + (^3P_J)_8$ contributions lead to worse χ^2 values, so we dropped this channel "a posteriori" in our analysis (i.e. the a parameter is set to zero).

The χ^2/N_{df} definition is

$$\chi^2/N_{df} = \frac{1}{N_{df}} \sum_{k=1}^{N} \left(\frac{y^k_{theo} \ - \ P^k_{exp}}{\varepsilon(P^k_{exp})} \right)^2$$

where N_{df} means the number of degrees of freedom; the y^k_{theo} are the theoretical values depending on b, and P^k_{exp} are the experimental points from CDF data. Thus, we can modify the above expression as follows

$$\chi^2/N_{df} = \frac{1}{N_{df}} \sum_{k=1}^{N} \left(\frac{H_k \ - \ P^k_{exp}}{\varepsilon(P^k_{exp})} \right)^2$$

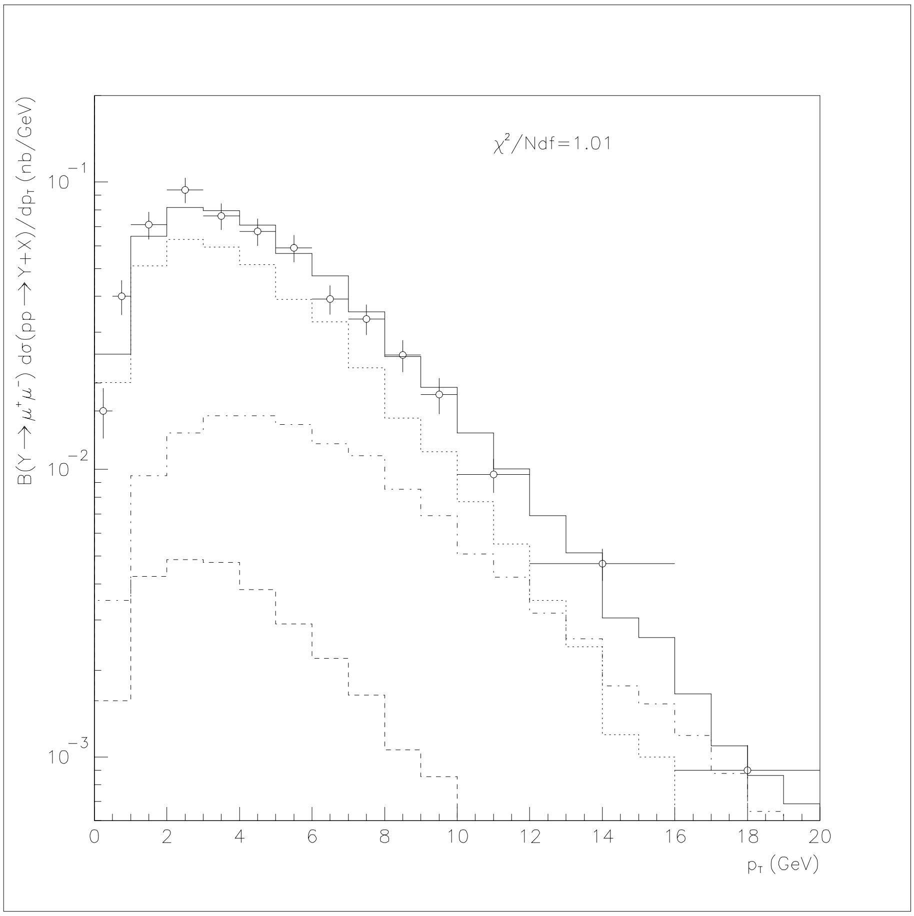

Figure 3.1: Histogram that illustrates the situation when fitting the NRQCD MEs for the CTEQ2L case: Solid line displays the whole histogram, dotted, dot-dashed, and dashed line shows the CSM, $(^3S_1)_8$, and $(^1S_0)_8 + (^3P_J)_8$ contribution, respectively.

N is the number of bins that corresponds to the number of experimental points one by one. However, as shown in figure 3.2, there are cases in which one experimental point corresponds to more than one bin; in those situations, previously, an average over those bins were performed, either for the whole and partial contributions. For instance, in the figure we can see that the 9-th experimental point, $p9$, embraces the 15-th up to the 20-th bin, i.e. from $M15$ to $M20$; whereas the 4-th experimental point amounts a single bin, $M4$.

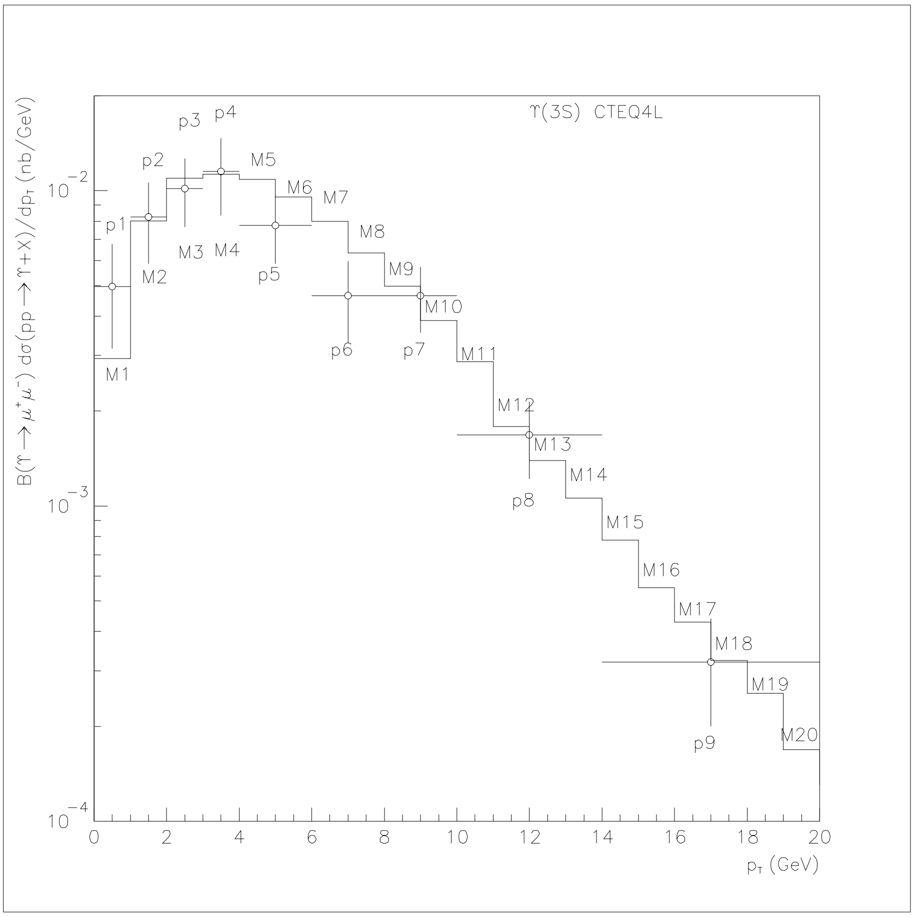

Figure 3.2: Histogram that illustrates the situation when fitting the NRQCD MEs. M_i corresponds to the result of the generation, and P_i represents the experimental points.

Regarding the requirement for a minimal χ^2; in the CTEQ4L case this search implies a one-parameter fit, whereas a two-parameter fit arises in the CTEQ2L one.

Further details about those fits and the calculation of their statistical errors can be found in Appendix B.

3.5.1 Theoretical curves from the histograms

The theoretical curves appearing in all plots corresponding to the fit (and extrapolations) of the differential cross sections have been obtained from histograms (filled with the corresponding PYTHIA output data) by means of the following four-parameter p_T function:

$$F[\alpha_1, \alpha_2, \alpha_3, \alpha_4; p_T] \ = \ \alpha_1 \, \frac{p_T^{\alpha_2}}{(\alpha_3 + p_T^2)^{\alpha_4}} \qquad (3.24)$$

Chapter 4

$\Upsilon(nS)$ hadroproduction at the Tevatron

Along this chapter, the results of the fits of the TEVATRON data are shown as well as some physical conclusions deriving from them. Basically, the analysis has been carried out using the CTEQ4L parton distribution function (PDF); however it will be instructive to present some results employing the (now outdated) CTEQ2L PDF as a complementary study. Moreover, CTEQ2L is still used in current applications of PYTHIA at LHC collaborations; this fact reinforces the motivation to include this PDF in this study.

We will base our analysis of bottomonia inclusive production on the results from Run IB of the CDF collaboration [7] at the Fermilab Tevatron. This means significantly more statistics than the data sample from Run IA, employed in a former analysis [25]. However, the different sources of prompt $\Upsilon(1S)$ production were not yet separated along the full accessible p_T-range. Hence we give the numerical values for some relevant combinations of long-distance MEs, including *direct* and *indirect* $\Upsilon(nS)$ inclusive production extracted from the fit to the CDF experimental points. (Prompt resonance production includes both direct and indirect channels, the latter referring to feeddown from higher $\Upsilon(nS)$ and $\chi_{bJ}(nP)$ states.) Nevertheless, we still are able to estimate some colour-octet MEs for *direct* $\Upsilon(1S)$ production from the measurements on different production sources at $p_T > 8$ GeV [9].

The following CSM parameters were employed, from [26], following the recipe explained in the previous chapter, in order to determine the radial wave functions at the origin (and their derivatives). The branching ratios for the $\chi_{bJ}(nP)$ decaying to Υ was taken from [8].

Colour-singlet parameters:

- $< O_1^{\Upsilon(1S)}(^3S_1) > |_{tot} = 11.1$ GeV^3
- $< O_1^{\Upsilon(2S)}(^3S_1) > |_{tot} = 5.01$ GeV^3
- $< O_1^{\Upsilon(3S)}(^3S_1) > |_{tot} = 3.54$ GeV^3
- $< O_1^{\chi_{b1(1P)}}(^3P_1) >= 6.09$ GeV^5
- $< O_1^{\chi_{b1(2P)}}(^3P_1) >= 7.10$ GeV^5

4.1 Fits to Tevatron data using CTEQ4L

We performed an analysis of bottomonia CDF data [7], incorporating both direct and indirect production in our generation through the CSM (as a "fixed" contribution which, in fact, is dominant at low and even moderate p_T) and the COM, adjusting the long distance parameters for different cut-offs from best $\chi^2_{DF} \equiv \chi^2/N_{DF}$ fits to the experimental points, as were explained in the previous chapter, using the CTEQ4L PDF.

4.1.1 Extraction of the colour-octet MEs

In Figures 4.1, 4.2 and 4.3 we show the theoretical curves obtained from our fits to CDF data. In general, nice fits, with χ^2_{DF} values not too far from unity were found, especially in the $\Upsilon(3S)$ case; instead, the $\Upsilon(2S)$ came out to be the worst one. Possibly this fact can be attached to the large uncertainties (up to $\sim$ 50%) in the branching ratios of the $\chi_{bJ}(2P)|_{CSM}$

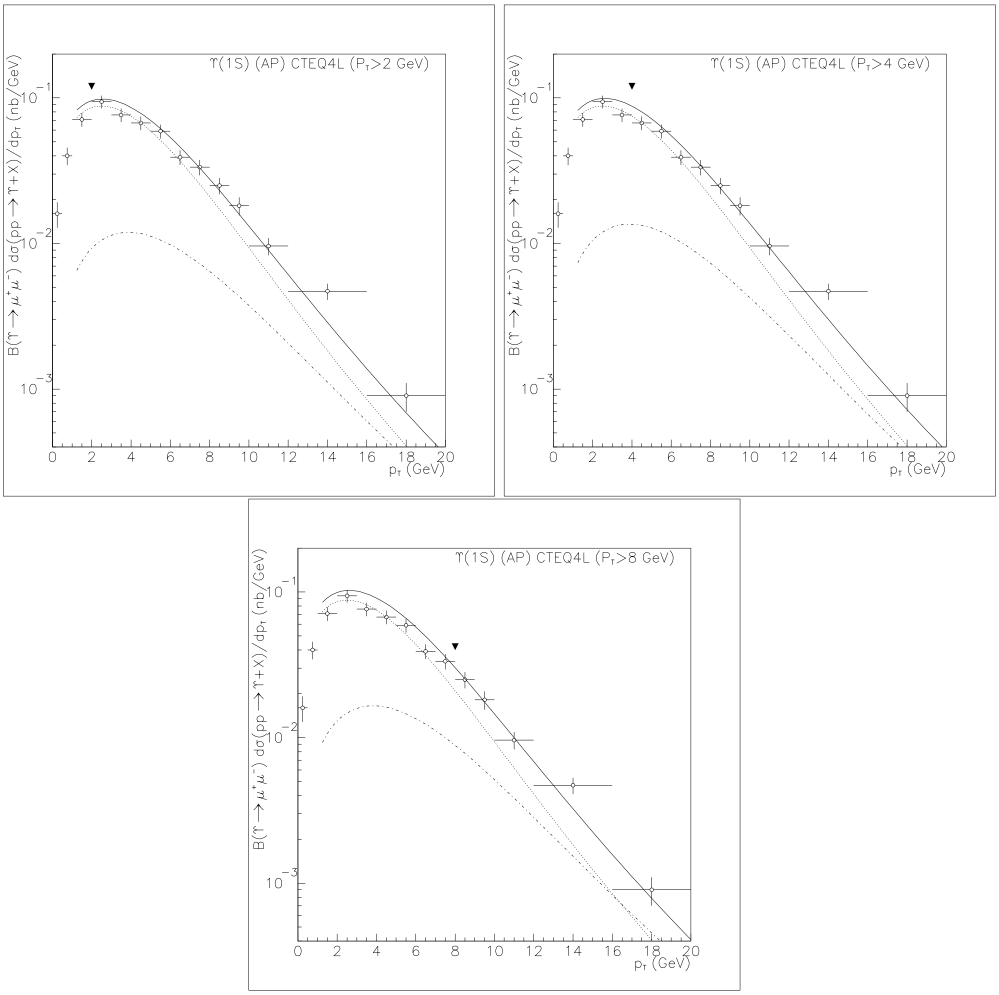

Figure 4.1: Different fits to the Tevatron data on $\Upsilon(1S)$ inclusive production in the rapidity interval $|y| < 0.4$ using CTEQ4L PDF and $m_b = 4.88$ GeV. Dot, dot-dash and solid lines correspond to the CSM, COM (${}^3S_1^{(8)}$ only) and all contributions, respectively. The triangle mark indicates the p_T lower cut-off used in the fit for each case: 2, 4 and 8 GeV. However, we plot the resulting curves extrapolating back over $p_T > 1$ GeV in all cases.

decay to $\Upsilon(2S)$. Thus the CSM is perhaps overestimated, since it almost saturates the differential cross section at the low p_T region; in addition, it happens that CTEQ4L tends to enhance the cross section values in the

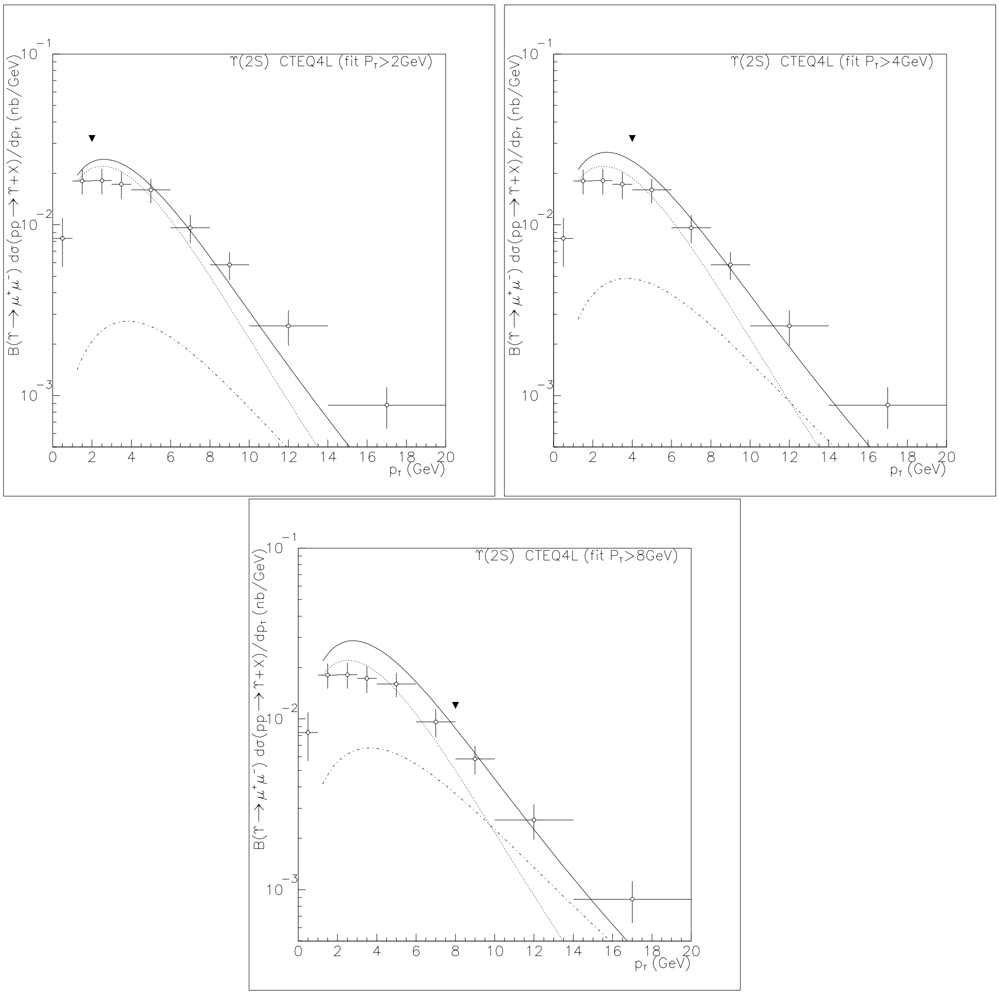

Figure 4.2: Different fits to the Tevatron data on $\Upsilon(2S)$ inclusive production in the rapidity interval $|y| < 0.4$ using CTEQ4L PDF and $m_b = 4.88$ GeV. Dot, dot-dash and solid lines correspond to the CSM, COM (${}^3S_1^{(8)}$ only) and all contributions, respectively. The triangle mark indicates the p_T lower cut-off used in the fit for each case: 2, 4 and 8 GeV. However, we plot the resulting curves extrapolating back over $p_T > 1$ GeV in all cases.

low p_T values, because of its BFKL style rise at low x, as we shall see. All those facts contribute to spoil the fit of the COM cross section in the p_T region of interest. Let us stress that in the fitting procedure we excluded any

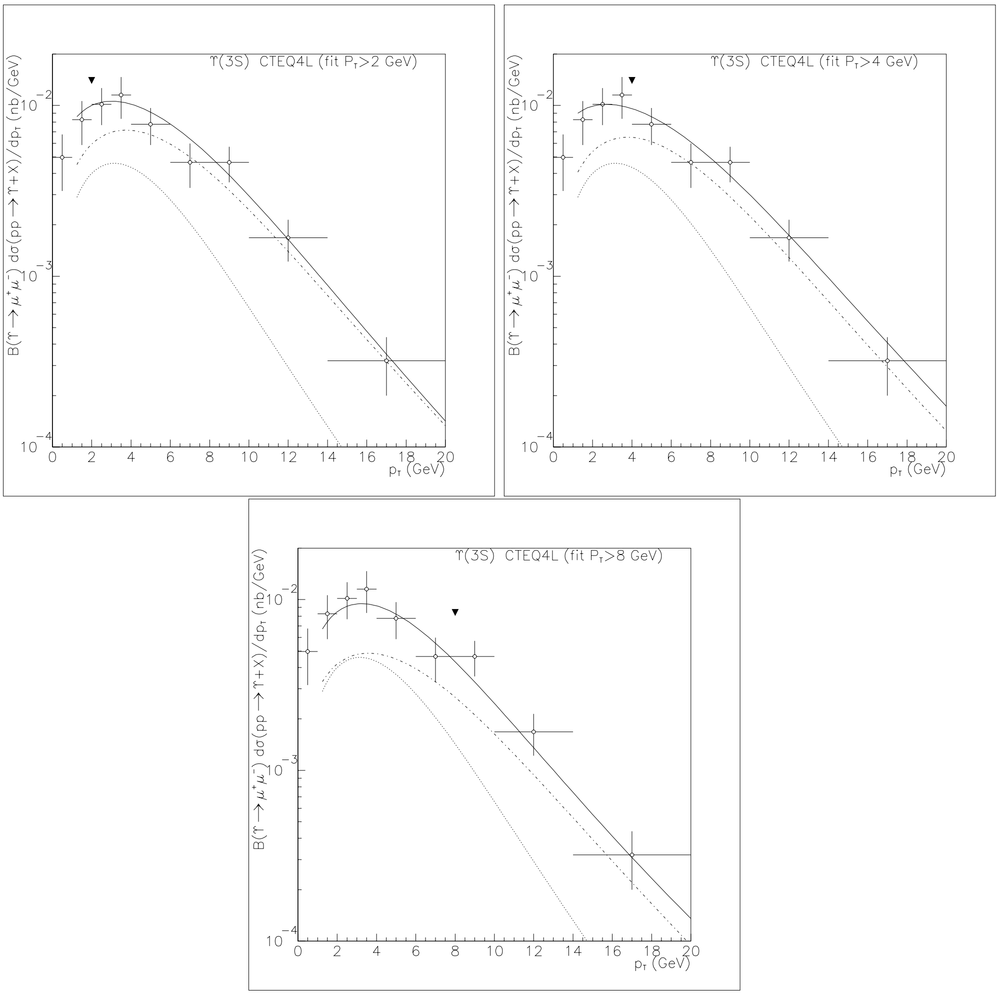

Figure 4.3: Different fits to the Tevatron data on $\Upsilon(3S)$ inclusive production in the rapidity interval $|y| < 0.4$ using CTEQ4L PDF and $m_b = 4.88$ GeV. Dot, dot-dash and solid lines correspond to the CSM, COM (${}^3S_1^{(8)}$ only) and all contributions, respectively. The triangle mark indicates the p_T lower cut-off used in the fit for each case: 2, 4 and 8 GeV. However, we plot the resulting curves extrapolating back over $p_T > 1$ GeV in all cases.

possible *negative* contribution from the different channels at the cross section level, in contrast to [37]. Hence we had to dismiss any contribution from the ${}^1S_0 + {}^3P_J$ channels or, in other words, we set the M_5 long-distance parameter (as defined in chapter 3) equal to zero, since any positive contribution from this channel would lead to a worse χ^2_{DF} value in all cases.

Table 4.1: Values of $< O_8^{\Upsilon(nS)}(^3S_1) > |_{tot}$; $n = 1, 2, 3$ (in units of 10^{-3} GeV^3) from the best fits to CDF data at the Tevatron on prompt $\Upsilon(nS)$ inclusive production for different p_T lower cuts. We also provide the χ^2_{DF} value in each case. The CTEQ4L PDF was used with initial-state and AP evolution activated in PYTHIA.

p_T cut-off:	2 GeV (χ^2_{DF})	4 GeV (χ^2_{DF})	8 GeV (χ^2_{DF})
$1S$	77±17 (1.74)	87±16 (1.53)	106±13 (1.00)
$2S$	40±29 (2.87)	73±18 (1.58)	103±27 (1.87)
$3S$	99±11 (1.00)	91±15 (1.00)	68±11 (1.00)

In Table 4.1 we show the values of $< O_8^{\Upsilon(nS)}(^3S_1) > |_{tot}$ $(n = 1, 2, 3)$, as defined in Eq. (3.4), for different p_T lower cut-offs, in correspondence with the plots of Figures 4.1-3. All values are roughly of the order of 10^{-1} GeV^3 and in agreement, within the errors, with the results obtained for $p_T > 8$ GeV by the authors of Ref. [37] using the CTEQ5L parton distribution function.

Nevertheless, let us stress that our numerical estimates for the colour-octet MEs have to be viewed with some caution because of the theoretical and "technical" (due to the Monte Carlo assumptions) uncertainties. For example our algorithm for AP evolution (see chapter 3) should be regarded as a way of reasonably steepening the high-p_T tail of the (leading-order) differential cross section, which otherwise would fall off too slowly as a function of p_T.

4.2 Fits to Tevatron data using CTEQ2L

In Table 4.2 we present the results of our fit to CDF data [7] using

CTEQ2L (both in 10^{-3} GeV^3 units); errors are only statistical. The statistical χ^2/Ndf are quite good. Let us remark that due to the p_T cut-off parameter set in the generation, only those experimental points for $p_T > 2$ GeV were used in the fit.

Table 4.2: Values of $< O_8^{\Upsilon(nS)}(^3S_1) > |_{tot}$; $n = 1, 2, 3$ (in units of 10^{-3} GeV^3) from the best fits to CDF data at the Tevatron on prompt $\Upsilon(nS)$ inclusive production for a p_T cut off equal to 2 GeV. The CTEQ2L PDF was used with initial-state and AP evolution activated in PYTHIA.

$\Upsilon(nS)$ [p_T cut-off 2 GeV]:	$< O_8^{\Upsilon(nS)}(^3S_1) > \|_{tot}$	χ^2_{DF}
$(1S)$	139±18	1.00
$(2S)$	80±20	1.53
$(3S)$	75±10	1.00

4.3 Separated production sources for $p_T > 8$ GeV

Current statistics does not permit to subtract indirect production sources to obtain the direct $\Upsilon(1S)$ production cross section along the full accessible p_T-range. Nevertheless, feeddown from higher states ($\Upsilon(nS)$, $\chi_{bJ}(nP)$) was experimentally separated out for $p_T > 8$ GeV [9]. We used this information to check our analysis *a posteriori* (rather than using it as a constraint in the generation) and to draw some important physical conclusions. To this end the relative fractions of the contributing channels for $p_T > 8$ GeV are reproduced in Table 4.3 from Ref. [9]. On the other hand, we show in Table 4.4 (which updates our older results presented in Ref. [38] using CTEQ2L) the fractions found in this work corresponding to the different generated channels for $p_T > 8$ GeV using CTEQ4L, following the notation introduced in chapter 3.

Table 4.3: Relative fractions (in %) of the different contributions to $\Upsilon(1S)$ production from CDF data at $p_T > 8$ GeV [9]. Statistical and systematic errors have been summed quadratically.

contribution	Tevatron results
direct $\Upsilon(1S)$	50.9±12.2
$\Upsilon(2S)+\Upsilon(3S)$	11.5±9.1
$\chi_b(1P)$	27.1±8.2
$\chi_b(2P)$	10.5±4.6

Table 4.4: Relative fractions (in %) of the different contributions to $\Upsilon(1S)$ production at the Tevatron for $p_T > 8$ GeV from our generation (CTEQ4L). Possible contributions from $\chi_{bJ}(3P)$ states were not generated.

contribution	our generation
$\Upsilon(1S)\vert_{^3S_1^{(8)}}$	36.8
$\Upsilon(1S)\vert_{CSM}$	19.5
$\Upsilon(2S)+\Upsilon(3S)\vert_{CSM}$	3.9
$\chi_b(1P)\vert_{CSM}$	24.1
$\chi_b(2P)\vert_{CSM}$	15.7

As an additional check, we compare the experimental integrated cross section with the one obtained by means of the generation: Tevatron data provides

$$\sigma_{exp}|_{p_T\geq 8GeV} \;=\; (84.64\;\pm\;5.57)\;pb$$

from the generation we obtain

$$\sigma_{gen}|_{p_T\geq 8GeV} \;=\; 84.7\;pb$$

As can be seen, both quantities are in excellent agreement.
By comparison between Tables 4.3 and 4.4 we can conclude that the $\Upsilon(1S)$ indirect production from χ_{bJ}'s decays is almost completely accounted for by

the CSM according to the assumptions and values of the parameters presented in the previous section. Indeed, experimentally 37.6±9.4% of $\Upsilon(1S)$ production is due to $\chi_{bJ}(1P)$ and $\chi_{bJ}(2P)$ decays [9] while from our generation we find a similar global value, namely 39.8%, coming exclusively from colour-singlet production! Moreover, assuming that a 7.6% from the 36.8% fraction (corresponding to the colour-octet ${}^3S_1^{(8)}$ contribution as expressed in Eq. (3.4)) can be attributed to the $\Upsilon(2S) + \Upsilon(3S)$ channel in addition to the colour-singlet contribution (3.9%), we obviously get the fraction 11.5% for the latter, bringing our theoretical result into agreement with the experimental value. This single assignment implies to reproduce quite well the experimental fraction ($\approx$ 51%) of direct $\Upsilon(1S)$ production by adding the remaining ${}^3S_1^{(8)}$ contribution to the $\Upsilon(1S)_{CSM}$ channels ($\approx$ 49%) in our generation.

Of course all the above counting was based on the central values from Table 4.3 and subject to rather large uncertainties. Nevertheless, apart from the consistency of our generation w.r.t. experimental results under minimal assumptions, we can conclude again as in [38] that there is almost *no need for* $\Upsilon(1S)$ *indirect production from feeddown of* χ_{bJ} *states produced through the colour-octet mechanism.* In other words, the relative contribution from P-wave states to $< O_8^{\Upsilon(1S)}({}^3S_1) > |_{tot}$ in Eq. (3.4) should be quite smaller than naïvely expected from NRQCD scaling rules compared to the charmonium sector, in agreement with some remarks made in [26] and recent results found in [37]. The underlying reason for this discrepancy w.r.t. other analysis [25] can be traced back to the dominant colour-singlet contribution to the cross section at p_T values as much large as $\simeq$ 18 GeV (see Figure 4.1) caused by the effective k_T smearing.

On the other hand the corresponding velocity scaling rule in the S-wave bottomonium sector is roughly verified as we can see. Defining the ratios of matrix elements:

$$R_v(n) \;=\; \frac{<O_8^{\Upsilon(nS)}(^3S_1)>|_{tot}}{<O_1^{\Upsilon(nS)}(^3S_1)>|_{tot}}\ , \tag{4.1}$$

its values, shown in Table 4.5, are in accordance with the expected order-of-magnitude $v^4 \approx 0.01$, where v is the relative velocity of the bottom quark inside bottomonium. Nevertheless we realize an increase of $R_v(n)$ for higher n values. Assuming that the $<O_8^{\Upsilon(nS)}(^3S_1)>|_{tot}$ matrix element could be interpreted as a (weighted) colour-octet wave function squared (in the same way as $<O_1^{\Upsilon(nS)}(^3S_1)>|_{tot}$ w.r.t. the colour-singlet state, see chapter 3) the ratio $R_v(n)$ of both squared wave functions in the origin comes out as not independent of the resonance state under consideration. Thus we conclude that this particular NRQCD velocity scaling rule, although valid as an order-of-magnitude estimate, retains a weak dependence on the principal quantum number n, not completely cancelling in the ratio (4.1).

Table 4.5: Values (in units of GeV^3) of different colour-singlet and colour-octet combinations of MEs according to Eqs. (3.2) and (3.4) and the ratios $R_v(n)$; $n = 1,2,3$. The best χ^2_{DF} values from Table 4.1 are displayed.

Resonance	$<O_1^{\Upsilon}(^3S_1)>|_{tot}$	$<O_8^{\Upsilon}(^3S_1)>|_{tot}$	$R_v(n)$
$\Upsilon(1S)$	11.1	0.106	0.0095
$\Upsilon(2S)$	5.01	0.073	0.0145
$\Upsilon(3S)$	3.54	0.099	0.028

4.4 Gaussian $< k_T >$ smearing

As outlined in chapter 3, the theoretical differential cross sections on inclusive production of bottomonia would stand above Tevatron experimental points for relatively high p_T if the set of long-distance parameters from [25] were "blindly" employed in the PYTHIA generation running with initial-state radiation on. This is the analogous conclusion reached to in the equivalent analysis performed on charmonia hadroproduction [34]. Indeed the smearing caused by multiple emission of gluons by the interacting partons is not limited to small p_T values as could be initially thought, but its influence spreads over a larger region of transverse momenta. In fact we have checked, from a fit to the $\Upsilon(3S)$ differential cross section, that actually this effect amounts to a pretty large value for the effective $< k_T >$ of about 2 GeV.

In Figure 4.4 we show the resulting histogram, corresponding to a value $\sigma = 2$ GeV, i.e. $< k_T >= 1.8$ GeV. This result updates the study performed in [39] using the colour-evaporation model, improving the equivalent fit with a similar value ($< k_T >= 2$ GeV).

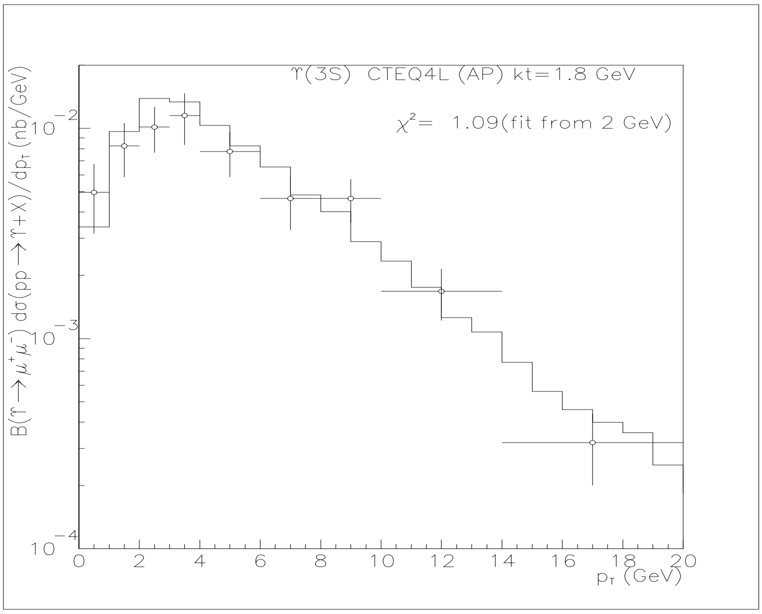

Figure 4.4: Fit to the Tevatron data on $\Upsilon(3S)$ hadroproduction using a gaussian smearing function with $\sigma = 2$ GeV, i.e. $< k_T >= 1.8$ GeV.

4.5 $gg - gq - qq$ and CSM contributions

As explained in chapter 3 and in appendix A, originally the event generator PYTHIA 5.7 produces direct J/ψ and higher χ_{cJ} resonances via the CSM only [30]. In our analysis we have besides implemented a code in the event generator to account for the colour-octet production mechanism via the following α_s^3 partonic processes:

$$g \ + \ g \rightarrow (Q\overline{Q})[^{2S+1}X_J] \ + \ g \tag{4.2}$$

$$g \ + \ q \rightarrow (Q\overline{Q})[^{2S+1}X_J] \ + \ q \tag{4.3}$$

$$q \ + \ \overline{q} \rightarrow (Q\overline{Q})[^{2S+1}X_J] \ + \ g \tag{4.4}$$

where $(Q\overline{Q})[^{2S+1}X_J]$ stands for a certain heavy quarkonium state denoted by its spectroscopic notation (see chapter 2 for more details). In particular we have considered the $^3S_1^{(8)}$, $^1S_0^{(8)}$ and $^3P_J^{(8)}$ contributions as leading-order intermediate coloured states. In addition we generated $\Upsilon(nS)$ $(n = 1, 2, 3)$ and $\chi_{bJ}(nP)$ $(n = 1, 2)$ resonances decaying into $\Upsilon(1S)$, according to the CSM as mentioned above.

A p_T lower cut-off was set equal to 1 GeV (by default in PYTHIA) throughout the generation since some of the contributing channels are singular at vanishing transverse momentum [40]. Furthermore, all fits of Tevatron data were performed using p_T values above 2 GeV.

Table 4.6 presents the values of the cross sections generated for each channel contributing to the $\Upsilon(1S)$ one, this values are obtained normalizing by a factor that takes into account the rapidity cut, the decay $\Upsilon \rightarrow \mu^{\pm}$, following the discussion done in chapter 3, and the value of the best χ^2 colour-octet MEs. In Table 4.7 we show the corresponding values for the $\Upsilon(2S)$ and $\Upsilon(3S)$ cases, here the different CSM contributions are not separated.

Table 4.6: Integrated cross sections ($p_T > 1$ GeV) of the different contributions to $\Upsilon(1S)$ at Tevatron

contribution	σ (pb)
$\Upsilon(1S)\|_{CSM}$	151.3
$\Upsilon(2S)+\Upsilon(3S)\|_{CSM}$	30.2
$\chi_b(1P)\|_{CSM}$	194.9
$\chi_b(2P)\|_{CSM}$	135.2
$\Upsilon(1S)\|^{gg}_{COM}$	90.2
$\Upsilon(1S)\|^{gq}_{COM}$	36.1
$\Upsilon(1S)\|^{qq}_{COM}$	2.9

Table 4.7: Integrated cross sections ($p_T > 1$ GeV) of the different contributions to $\Upsilon(2S)$ and $\Upsilon(3S)$ at Tevatron.

contribution	σ (pb) $(2S)$	σ (pb) $(3S)$
CSM	126.4	28.7
$COM - gg$	26.5	39.9
$COM - gq$	11.5	17.1
$COM - qq$	1.0	1.6

Since we are mainly interested in the relative high and high p_T region, we find from our simulation (see Table 4.8) that gluon-gluon scattering actually stands for the dominant process at large p_T as expected, gluon-quark scattering contributes appreciably however ($\simeq 20 - 30\%$ of the colour-octet production cross section) whereas the quark-antiquark scattering represents a quite small fraction ($\simeq 1\%$ at the Tevatron). In Figure 4.5 we plot the gluon-gluon and quark-gluon ${}^3S_1^{(8)}$ contributions as a function of the transverse momentum of the resonance obtained from our generation for the Tevatron. This kind of information could be particularly interesting for our discussion on the probe the gluon density in protons developed in chapter 6.

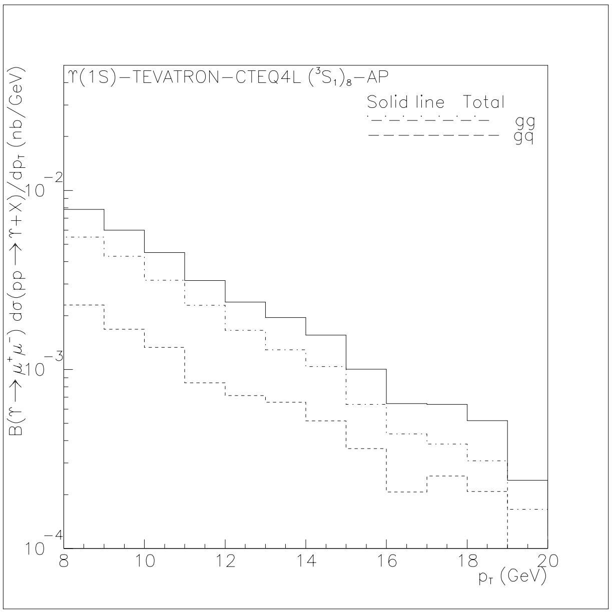

Figure 4.5: Gluon-gluon versus quark-gluon ${}^3S_1^{(8)}$ contributions from our $\Upsilon(1S)$ generation at the Tevatron for $p_T > 8$ GeV. The latter becomes more and more important at larger p_T as could be expected since higher Feynman x of protons are involved and the gq contribution becomes increasingly more significant w.r.t. the gg one.

Table 4.8: ${}^3S_1^{(8)}$ contributions to the $\Upsilon(nS)$ cross section at the Tevatron for $p_T > 8$ GeV

Contribution	%
gg	69
qg	30
$q\overline{q}$	1

On the other hand, regarding the cross sections obtained using CTEQ4L and comparing them with the previous ones obtained using CTEQ2L, we realize an increase in the “raw” cross sections, i.e. the ones obtained directly from PYTHIA generation without any kinematic cut. This discrepancy motivated the study that can be seen in appendix C. From this study one can conclude that the disagreement is "under control": It arises from the different behaviour when both PDFs are evolved to the energy scale of interest for us.

4.6 Altarelli-Parisi evolution

As yet explained, our Altarelli-Parisi (AP) mechanism provides an energy depletion of the (ungenerated) fragmenting gluon basing on the p_T of its gluonic partner. Here we can see the results, that are in agreement with previous work on charmonium hadroproduction [25, 40].

In Figure 4.6 the x_{AP} factor is plotted as a function of the transverse momentum of the resonance for the Tevatron event generation. We can realize that its main effect starts from about 10 GeV amounting to a factor of the order of $\simeq 1/2.5$ at high p_T.

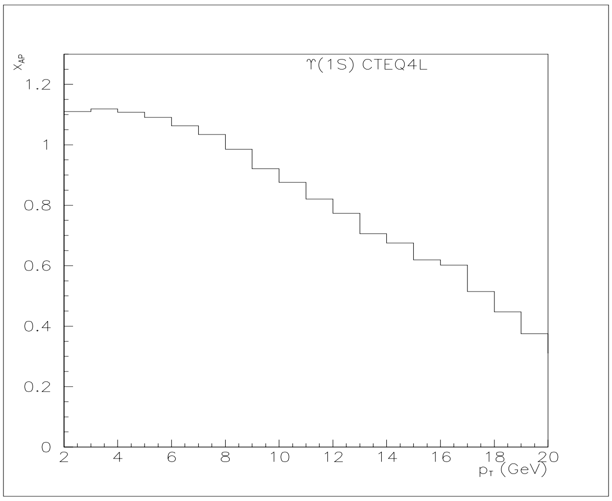

Figure 4.6: x_{AP} factor as a function of p_T for Tevatron energies obtained from our generation.

Moreover, in order to assess the effect of AP evolution on the fit parameters we show in Table 4.9 two sets of numerical values for the relevant colour-octet MEs obtained from a best χ^2 fit to Tevatron data [7] using the CTEQ4L PDF: (i) the first row corresponds to a generation *without* AP evolution; (ii) the second one does take it into account. Notice the increase of $<O_8^{\Upsilon(1S)}(^3S_1)>|_{tot}$ in the latter case w.r.t. AP off, but to a lesser extent than for charmonium [40].

Table 4.9: Colour-octet matrix elements (in units of 10^{-3} GeV^3) from the best fit to CDF data at the Tevatron on prompt $\Upsilon(1S)$ production. The CTEQ4L PDF was used with AP evolution off and on respectively.

ME:	$<O_8^{\Upsilon(1S)}(^3S_1)>|_{tot}$
AP off	70±15
AP on	77±17

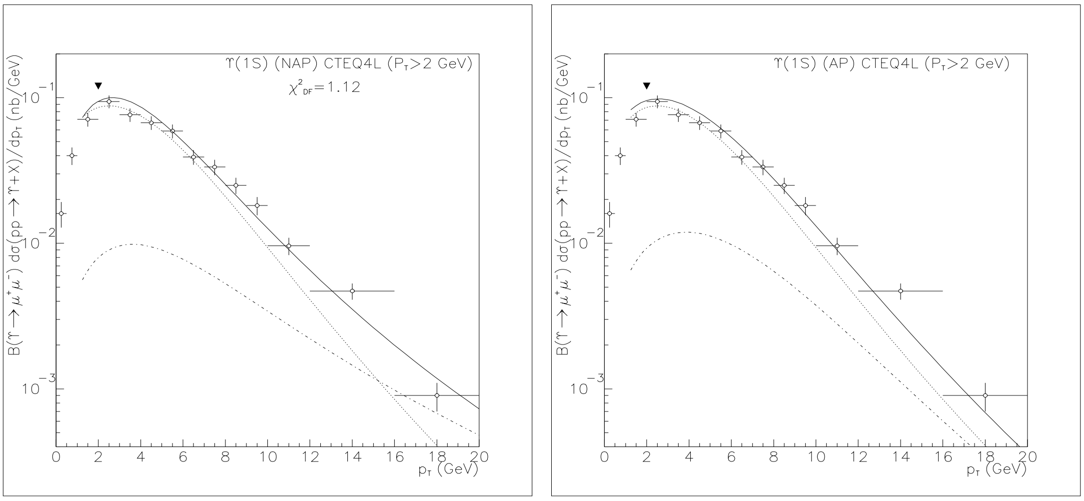

Figure 4.7: Theoretical curves obtained from a fit using PYTHIA including the colour-octet mechanism for prompt $\Upsilon(1S)$ production against CDF data at the Tevatron *a)* without AP evolution of the fragmenting gluon, *b)* with AP evolution of the fragmenting gluon. The CTEQ4L parton distribution function and $m_b =$ 4.88 GeV were employed in the fits; dotted line: CSM, dot-dashed line: $^3S_1^{(8)}$ contribution, solid line: all contributions.

It is worth noting that the effect of the AP evolution on the shape of the differential cross section over the [1,20] GeV p_T-range, though sizeable, is considerably less pronounced for bottomonium than for charmonium [40] likely because of the larger mass of the former. Nevertheless we can appreciate in Figure 4.7 that the plot corresponding to AP evolution is noticeably steeper at moderate and high p_T as could be expected. Let us finally remark that, although we can switch on/off AP evolution and initial-state radiation *at will* in the event generation, both next-to-leading order effects have to be incorporated for a realistic description of the hadronic dynamics of the process.

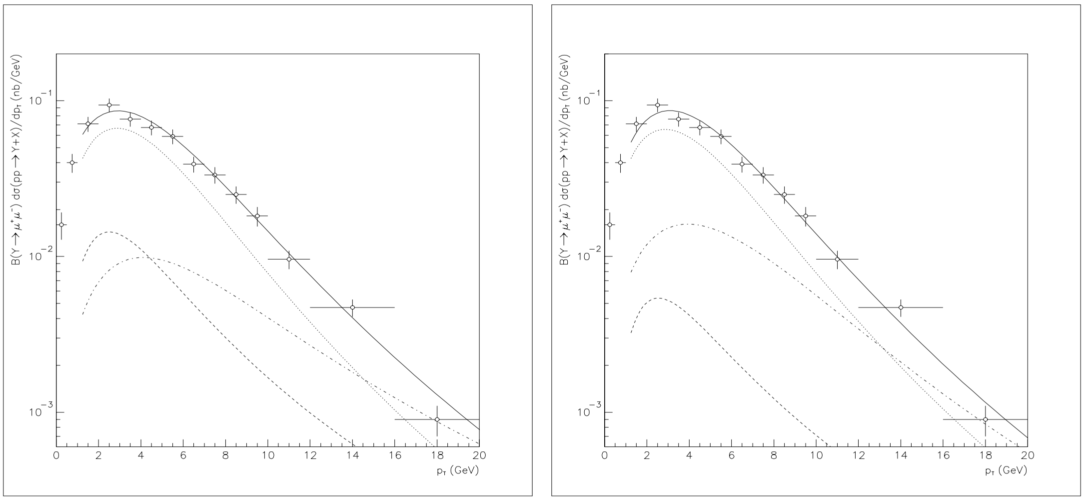

Figure 4.8: Theoretical curves obtained from a fit using PYTHIA including the colour-octet mechanism for prompt $\Upsilon(1S)$ production against CDF data at the Tevatron *a)* without AP evolution of the fragmenting gluon, *b)* with AP evolution of the fragmenting gluon using CTEQ2L PDF dotted line: CSM, dashed line: ${}^1S_0^{(8)} + {}^3P_J^{(8)}$ contribution, dot-dashed line: ${}^3S_1^{(8)}$ contribution, solid line: all contributions.

In Figure 4.8 and Table 4.10 we can see the corresponding results using CTEQ2L in the $\Upsilon(1S)$ case.

Table 4.10: Colour-octet matrix elements (in units of 10^{-3} GeV^3) from the best fit to CDF data at the Tevatron on prompt $\Upsilon(1S)$ production. The CTEQ2L PDF was used with initial-state radiation on, and AP evolution off and on respectively. $M_5^{\Upsilon(1S)}$ combination following the Eq. (3.8).

ME:	$< O_8^{\Upsilon(1S)}(^3S_1) >$	$M_5^{\Upsilon(1S)}$
AP off	93±12	17±20
AP on	139±18	6±5

4.7 CTEQ4L versus CTEQ2L

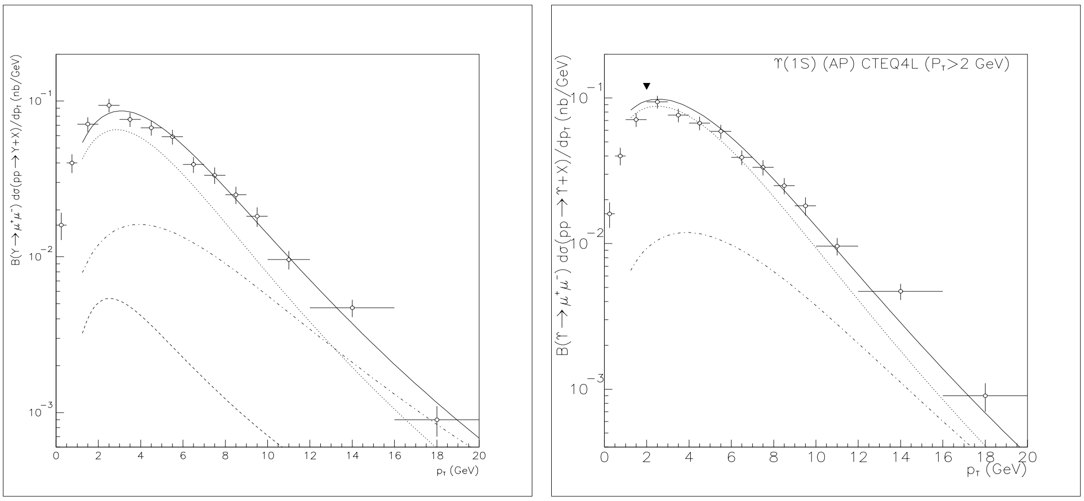

Figure 4.9: Fits to Tevatron $\Upsilon(1S)$ data using CTEQ2L *(left)* and CTEQ4L *(right)*; dotted line: CSM, dashed line $^1S_0 +^3 P_J$ contribution, dot-dashed line: $^3S_1^{(8)}$ contribution, solid line: all contributions.

In order to have a better comparison, Figure 4.9 presents together the two fits to the same Tevatron data [7] with both CTEQ2L and CTEQ4L PDFs. Notice that the $^1S_0 +^3 P_J$ contribution has been disregarded in the latter case.

The CTEQ4L PDF incorporates a BFKL style rise at small x, rather than a flat shape as in CTEQ2L. Therefore it is not surprising that we find smaller values for the colour-octet matrix elements in the former case, as can be seen from Tables 4.9 and 4.10.

Because of a different behaviour of AP that can be observed in CTEQ2L and CTEQ4L results, we show in Figure 4.10 a comparative plot that illustrates this difference generating $\Upsilon(1S)$-COM contribution using both PDFs with AP mechanism switched on.

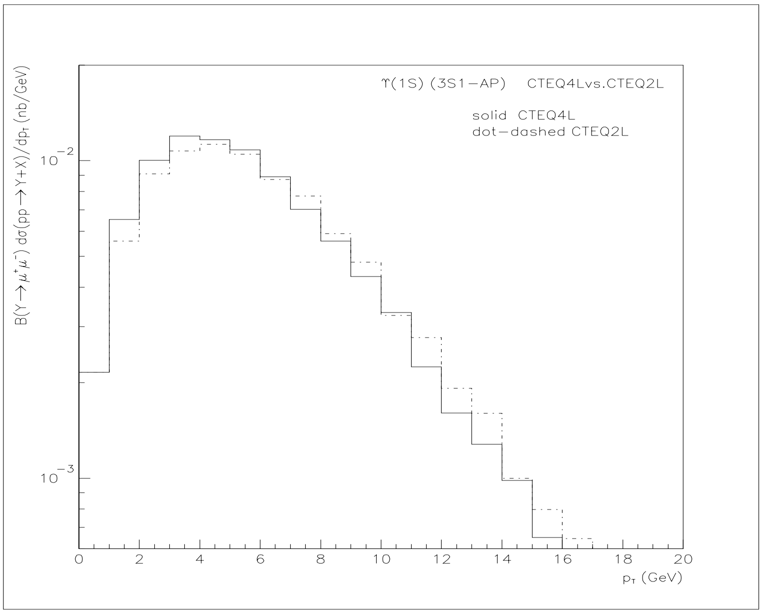

Figure 4.10: Comparative plot showing the result of the same COM contribution using the AP evolution mechanism with CTEQ2L and CTEQ4L PDFs.

From Figure 4.10, we can see that the COM cross section in the CTEQ4L case appears “sharper”, increasing the value of the differential cross section at lower p_T, than in the CTEQ2L one, according to the BFKL behaviour of the former.

To finish this comparison, in Table 4.11 we can see the cross sections obtained for each resonance, when the “normalization” factor is applied, using both PDFs CTEQ2L and CTEQ4L. The total cross section values obtained yield a 19%, 6%, 10% of variation for the $\Upsilon(1S),(2S),(3S)$ cases respectively.

Table 4.11: Cross sections (in pb) of the contributions to $\Upsilon(nS)$ at Tevatron, using CTEQ4L//CTEQ2L (left//right respectively) $p_T > 1$ GeV.

contribution	$\sigma_{CSM} 4L//2L$	$\sigma_{COM} 4L//2L$	$\sigma_{Total} 4L//2L$
$\Upsilon(1S)$	512//388	129//134	641//522
$\Upsilon(2S)$	126//115	39//40	165//155
$\Upsilon(3S)$	29//27	59//52	88//79

4.8 Ratios of cross sections

Taking the $\Upsilon(nS)$ total cross sections from the generation (Table 4.11), the ratios of the $\Upsilon(2S)$ and $\Upsilon(3S)$ w.r.t. $\Upsilon(1S)$ can be performed, later we can compare them with the ones using CDF data [7]. Table 4.12 shows the results. As we can see from Table 4.12, the generation agrees with the experiment. Also we realize that CTEQ4L generation reproduces better the data than CTEQ2L one. We will compare these ratios with the corresponding ones at LHC in the following chapter.

Table 4.12: Ratios of the cross sections at Tevatron from CDF data, CTEQ4L and CTEQ2L.

Ratio $\Upsilon(mS)/\Upsilon(1S)$	$Tevatron$	$CTEQ4L$	$CTEQ2L$
$(2S)/(1S)$	0.25 ± 0.02	0.26	0.30
$(3S)/(1S)$	0.14 ± 0.05	0.14	0.15

Chapter 5

$\Upsilon(nS)$ hadroproduction at the LHC

In this brief chapter the results concerning the predictions on bottomonia hadroproduction at LHC are shown. We already mentioned that bottomonium hadroproduction is especially interesting to check the validity of the colour-octet mechanism as often emphasized in the literature [41, 42]. This becomes particularly clear at the LHC since experimental data will spread over a wider p_T-range than at the Tevatron, allowing an overall study from low to very high p_T values. Therefore the expected transition of the different production mechanisms along the p_T region could be scrutinized in detail: from gluon gluon fusion at low p_T to the foreseen asymptotically dominant gluon fragmentation into bottomonium states.

5.1 Results using CTEQ4L

Keeping this interest in mind, our code was implemented in PYTHIA to generate prompt $\Upsilon(nS)$ resonances in proton-proton collisions at a center-of-mass energy of 14 TeV employing the best χ^2_{DF} colour-octet MEs shown in Table 4.1. In Figures 5.1, 5.2 and 5.3 the theoretical curves for the $\Upsilon(nS)$

($n = 1, 2, 3$) differential and integrated cross sections are exhibited as a function of p_T, including both direct production and feed-down from higher resonance states (except for the $\Upsilon(3S)$).

In Figures 5.4 we show our prediction for *direct* $\Upsilon(nS)$ production for both differential and integrated cross section. This is especially interesting if LHC detectors would be able to discriminate among those different sources of resonance production, as treated later.

Table 5.1: Predicted cross sections (in nb) of the different contributions to $\Upsilon(nS)$ and at LHC (p_T cut 1 GeV).

contribution	$\sigma\ (1S)$	$\sigma\ (1S)_{direct}$	$\sigma\ (2S)$	$\sigma\ (3S)$
CSM	27.4	6.9	6.9	1.2
$COM-gg$	6.1	4.8	1.9	2.9
$COM-gq$	1.5	1.2	0.5	0.7
$COM-q\overline{q}$	0.06	0.05	0.02	0.03
$TOTAL$	35.1	13.0	9.3	4.8

To this end we generated $\Upsilon(1S)$ events through both the CSM and COM making use of the following parameters

- $< O_1^{\Upsilon(1S)}(^3S_1) > |_{direct} = 9.28$ GeV^3 (from [26])
- $< O_8^{\Upsilon(1S)}(^3S_1) > |_{direct} = 0.084$ GeV^3

The first value corresponds to the CSM ME for direct production while the $< O_8^{\Upsilon(1S)}(^3S_1) > |_{dir}$ ME was obtained after removing the $\Upsilon(2S)+\Upsilon(3S)$ contribution according to the discussion made in the chapter 4- section 3, i.e. under the assumption that a fraction 7.6% from the 36.8% in Table 4.4 should be assigned to indirect production. Finally let us mention that we neglected any contribution from the $^1S_0^{(8)} +^3 P_J^{(8)}$ channels, in accordance with the analysis on Tevatron data made in the previous chapter.

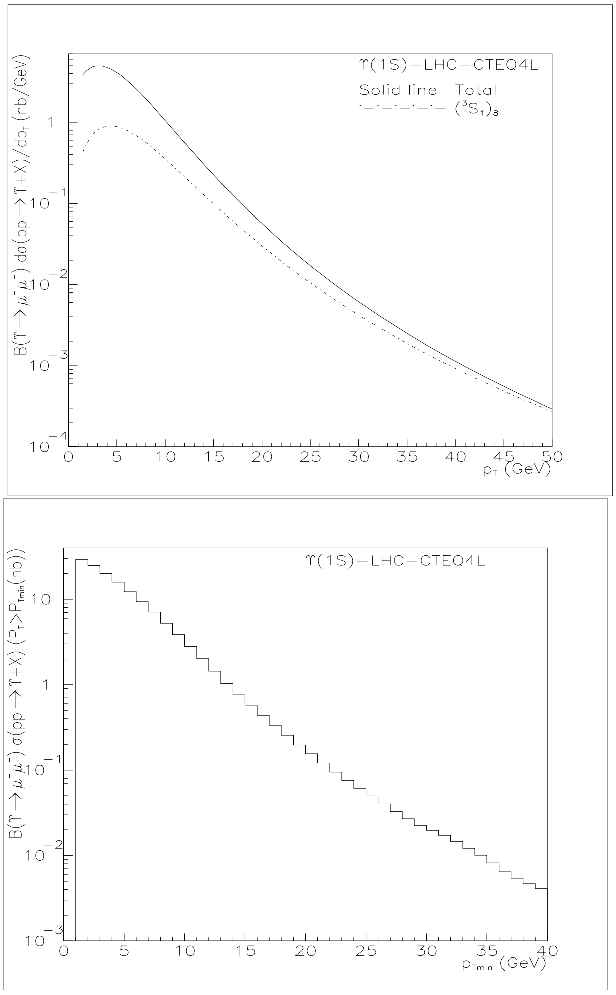

Figure 5.1: *Above* :Predicted prompt $\Upsilon(1S)$ differential cross section (multiplied by the muonic branching fraction) at the LHC using the CTEQ4L PDF and $m_b = 4.88$ GeV. A rapidity cut $|y| < 2.5$ was required. Dot-dashed line: $^3S_1^{(8)}$ contribution; solid line: all contributions. *Below :* Integrated cross section.

In Table 5.1 we can see a summary on the of the integrated cross sections results for each member of Υ family, providing also predictions for each source. These results were obtained from PYTHIA applying the normalization factor in the same way than in Tables 4.6 and 4.7. As a check, the values of these total cross sections are in agreement with the corresponding

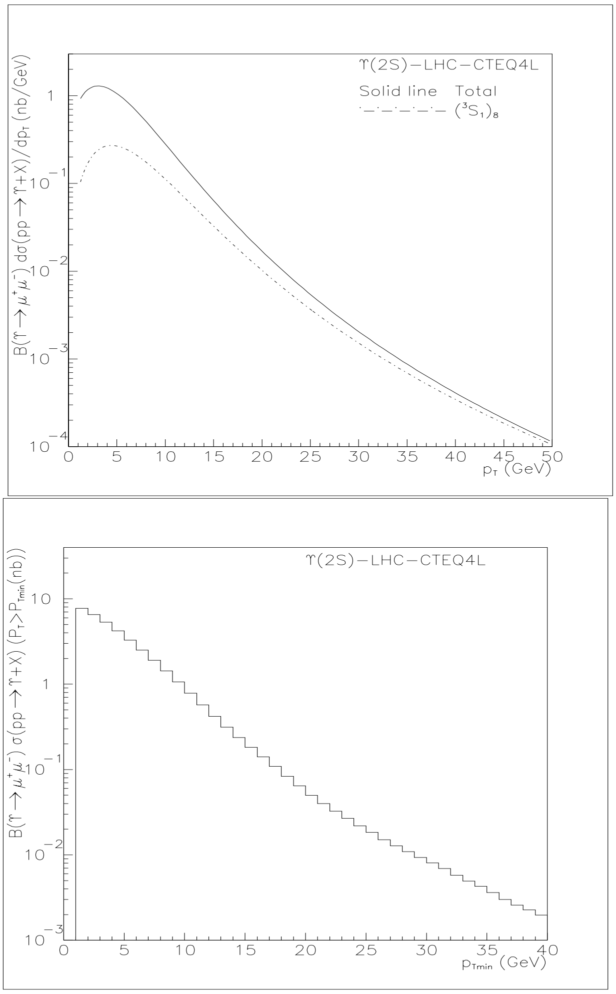

Figure 5.2: *Above* :Predicted prompt $\Upsilon(2S)$ differential cross section (multiplied by the muonic branching fraction) at the LHC using the CTEQ4L PDF and $m_b = 4.88$ GeV. A rapidity cut $|y| < 2.5$ was required. Dot-dashed line: ${}^3S_1^{(8)}$ contribution; solid line: all contributions. *Below :* Integrated cross section.

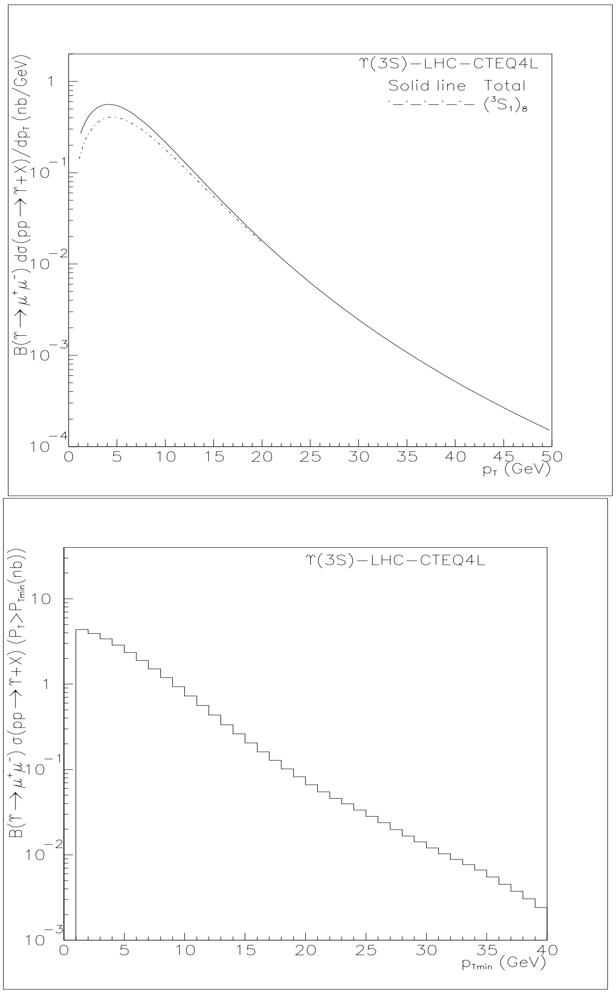

Figure 5.3: *Above :*Predicted prompt $\Upsilon(3S)$ differential cross section (multiplied by the muonic branching fraction) at the LHC using the CTEQ4L PDF and $m_b = 4.88$ GeV. A rapidity cut $|y| < 2.5$ was required. Dot-dashed line: ${}^3S_1^{(8)}$ contribution; solid line: all contributions. *Below :* Integrated cross section.

ones obtained in a independent way from Figures 5.1-5.3, integrating their corresponding differential cross sections for a $p_T - cut > 1$ GeV.

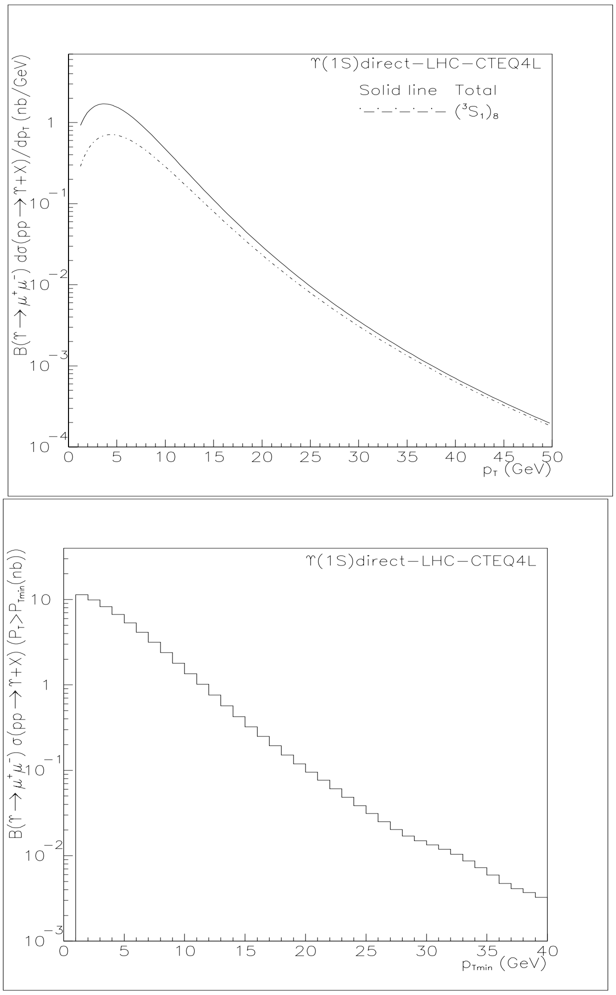

Figure 5.4: The same as in Figure 5.1 for *direct* $\Upsilon(1S)$ production at the LHC.

A p_T lower cut-off was set equal to 1 GeV (by default in PYTHIA) throughout the generation, since some of the contributing channels are singular at vanishing transverse momentum [40]. Furthermore, all fits of Tevatron

Table 5.2: ${}^3S_1^{(8)}$ contributions to the $\Upsilon(1S)$ cross section at the LHC for $p_T > 8$ GeV

Contribution	%
gg	80
qg	20
$q\bar{q}$	$\simeq 0$

data were performed using p_T values above 2 GeV.

We find from our simulation (see Table 5.2) that gluon-gluon scattering actually stands for the dominant process at high p_T as expected, gluon-quark scattering contributes appreciably however ($\simeq 20-30\%$ of the colour-octet production cross section), whereas the quark-antiquark scattering represents a quite small fraction ($\simeq 1\%$ at the Tevatron).

5.2 Results using CTEQ2L

Only in order to compare CTEQ4L versus CTEQ2L results, the corresponding theoretical curves for the $\Upsilon(1S)$ differential and integrated cross sections as a function of p_T are depicted in Figure 5.5, including both direct production and feed-down from higher resonance states for the CTEQ2L case, if we compare with the one obtained with CTEQ4L, we realize a slight decrease in the latter prediction with respect to the former, this fact is not surprising, since the value of the COM parameter has been lowered (see previous chapter) in changing from CTEQ2L to CTEQ4L.

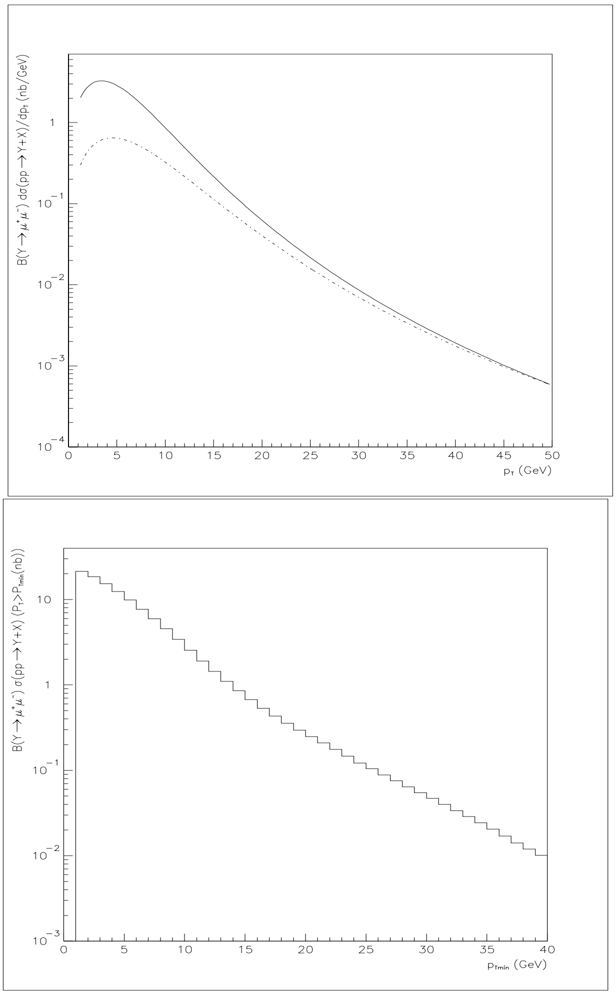

Figure 5.5: *Above:* Predicted prompt $\Upsilon(1S)$ differential cross section at the LHC using the CTEQ2L PDF and AP evolution incorporated in the generation. A rapidity cut $|y| < 2.5$ was required for bottomonium; dot-dashed line: ${}^3S_1^{(8)}$ contribution. Solid line: all contributions. *Below:* Integrated cross section.

5.3 Predicted ratios of the cross sections

Taking the $\Upsilon(nS)$ total cross sections from the generation (Table 5.1), a prediction of the ratios of the $\Upsilon(2S)$ and $\Upsilon(3S)$ w.r.t. $\Upsilon(1S)$ at LHC energies can be performed.

Table 5.3: Ratios of the Υ cross sections at LHC from the generation using CTEQ4L.

Ratio $\Upsilon(mS)/\Upsilon(1S)$	$LHC - value$
$(2S)/(1S)$	0.26
$(3S)/(1S)$	0.14

As we can see from Table 5.3 comparing results with the ones obtained from table 4.12 at Tevatron, the ratios are the same (actually they have a difference $\sim 1\%$), then we realize that phenomenologically there is a very weak kinematic dependence of the ratios. However from these tables, if we perform the same ratio $\sigma(\Upsilon(3S))/\sigma(\Upsilon(1S))$ but taking values $Tevatron/LHC$ or $LHC/Tevatron$ we obtain $\sim 10^{-3}$ and ~ 10, respectively; therefore this fact suggests that the weak dependence occurs when we consider similar kinematic conditions for both resonances. However we have put *the same* MEs in both cases. Then, taking similar kinematic conditions it seems that the quotient are sensitive, mainly, to the non perturbative part.

Chapter 6

Probing the gluon density in proton through Υ hadroproduction

In this chapter, we will focus on the possibility of probing the gluon density in protons using Υ hadroproduction, with the COM as the underlying framework.

As anticipated in chapter 1, the LHC machine can be viewed as a gluon-gluon collider to a large extent. Many signatures (and their backgrounds) of physics involve gluons in the initial state, and therefore an accurate knowledge of the gluon density in protons acquires a special relevance. So far, the most precise determinations of the gluon momentum distributions in the proton come from the analysis of the scaling violations of the structure function F_2. However, this represents an indirect method since it is the sea distribution which is actually measured and the gluon density is obtained by means of the QCD evolution equations. On the other hand, hadron-hadron scattering processes with direct photon production or jets in the final state will probably be extremely adequate to probe "directly" the gluon distribution in hadrons. Here, we shall examine the possibility of using heavy quarkonia inclusive production in proton-proton collisions at the LHC, in a complementary way to those studies. However, there are still many uncertainties and pending questions regarding quarkonia hadroproduction despite the existence of NRQCD [18], an effective theory coming from first principles, which should provide an adequate framework for this kind of processes involving both perturbative and non-perturbative aspects of the strong interaction dynamics. Likely, forthcoming experimental data - and their respective analysis - from Tevatron and other machines like HERA, should clarify the situation before LHC becomes operative.

6.1 Probing the gluon density in proton

In the following we shall focus on very high p_T production of bottomonia states. Therefore the main production mechanism according to the COM should be through the partonic subprocess:

$$g\ g \to g^*\ g \tag{6.1}$$

followed by the gluon fragmentation into a $\Upsilon(nS)$ state:

$$g^* \to \Upsilon(nS)\ X \qquad ;\ (n=1,2,3) \tag{6.2}$$

produced through a colour-octet mechanism. On the other hand, the bottom mass is large enough to justify the colour-octet mechanism applied to quarkonium hadroproduction (whether a similar approach could be applied to charmonium resonances has to be checked, for example analyzing the transverse polarization of the resonance).

Ideally, the final state gluon (g) in Eq. (6.1) will give rise to a recoiling jet ($g \to jet$), sharing, in principle, the same transverse momentum as the heavy resonance (this approach can be done in absence of higher order corrections; however we will include them in section 6.3).

Hence events would topologically consist of an almost isolated muon pair from the decay of the heavy resonance and a recoiling jet, as Figure 6.1 illustrates. Indeed one should expect a $\mu^+\mu^-$ pair almost isolated because the energy difference between the masses of the intermediate coloured and final states is assumed to be rather small (of the order of $m_b v^2 \simeq 500$ MeV) then allowing the emission of eventually a few light hadrons via soft gluon radiation at the final hadronization stage.

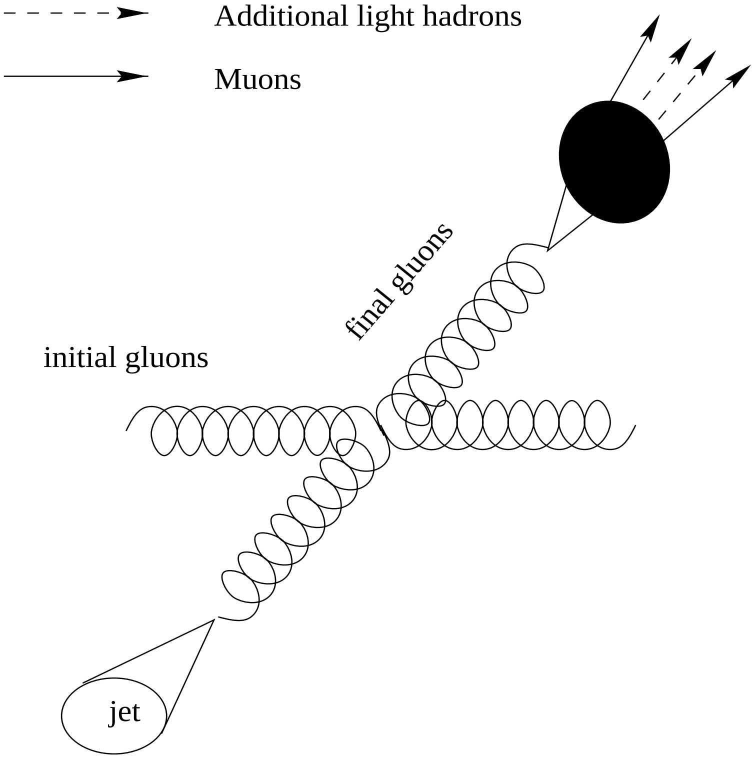

Figure 6.1: Graph corresponding to a gg process in bottomonia production.

Bottomonia production coming from fragmenting gluons in QCD jets (an alternative production mechanism, see [43]) should not exactly display the same signature as the hard α_s^3 processes. Indeed, the muon pair would be embedded in one of the two jets - not so much isolated as in the process (6.1-6.2) due to the production cascade - and its momentum should not balance the momentum of the other event jet to the same extent. In sum, the signature of an almost isolated muon pair recoiling against a jet with an approximate momentum balance in the transverse plane, should provide a suitable tag for the production mechanism represented in Eqs. (6.1-6.2).

We shall assume a tight kinematic cut in this approach: Both the rapidity of the heavy resonance and the rapidity associated to the recoiling jet should be around zero. However, in order to increase the foreseen statistics, one could dispense with this constraint by only requiring (within the experimental and theoretical uncertainties) back-to-back production. We shall come back to this issue at the section 3.

6.1.1 Developing the idea

In the absence of any intrinsic k_T effect, we can write the triple differential cross section for the inclusive production process $pp{\rightarrow}\Upsilon X$ as

$$\frac{d^3\sigma}{dy_{\Upsilon}dy_{jet}dp_T} = 2p_T \sum_{ab} x_a x_b f_{a/p}(x_a) f_{b/p}(x_b) \frac{d\hat{\sigma}_{ab}}{d\hat{t}} \tag{6.3}$$

where $f_{a/p}(x_a)$ denotes the parton-a density in the proton, and

$$\frac{d\hat{\sigma}_{ab}}{d\hat{t}} \equiv \frac{d\hat{\sigma}}{d\hat{t}}(ab{\rightarrow}\Upsilon c) = \frac{1}{16\pi\hat{s}^2}\ \overline{\sum}|\mathcal{A}(ab{\rightarrow}\Upsilon c)|^2 \tag{6.4}$$

stands for the partonic differential cross section (the barred summation denotes an average over initial and final spins and colours. See chapter 3, section 6) consisting of a short distance (and calculable) part and a long distance part which can be identified as a colour-octet matrix element according to NRQCD. This factorization of the cross section was established on solid grounds in Ref. [18] within the NRQCD framework, as explained in chapter 2.

defining the rapidity difference (not necessarily small) between the Υ and the recoiling jet as δy then x_a and x_b should satisfy the following leading-order kinematic constraints:

$$\delta y \;=\; ln\left(\frac{x_a}{x_b}\right)$$

where we have assumed that $\delta y = y_\Upsilon - y_{jet}$, and

$$x_a x_b \;= \frac{\hat{s}}{s}$$

Hence one can conclude that

$$x_a \;=\; \left(\frac{\hat{s}}{s}\right)^{1/2} e^{-\frac{\delta y}{2}} \;\; x_b \;=\; \left(\frac{\hat{s}}{s}\right)^{1/2} e^{\frac{\delta y}{2}}$$

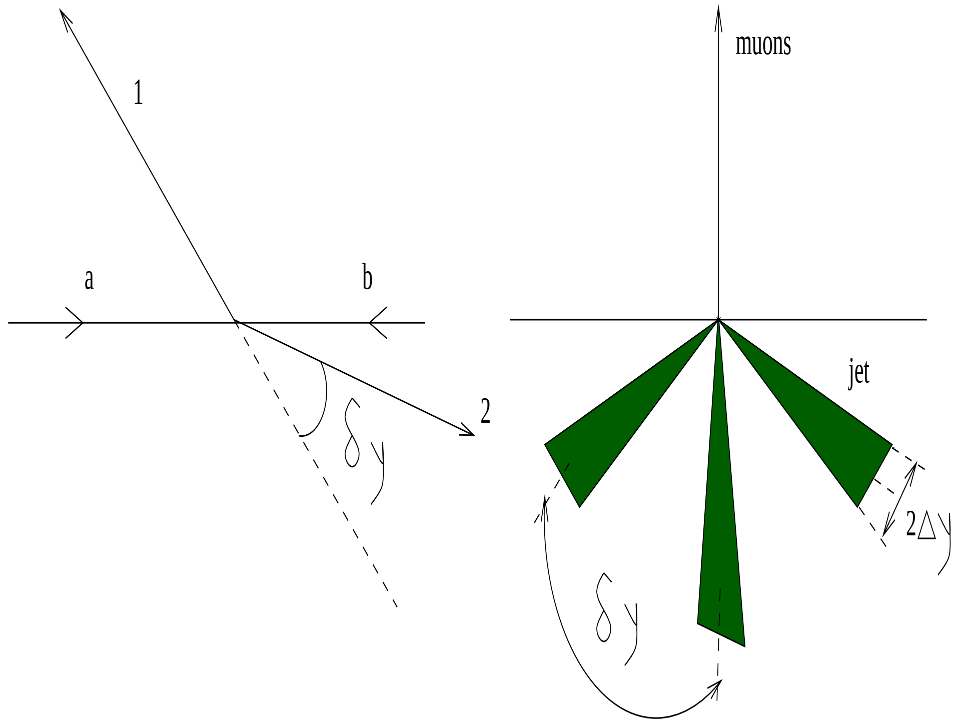

Figure 6.2: basic kinematics of the subprocess and variables used in the text.

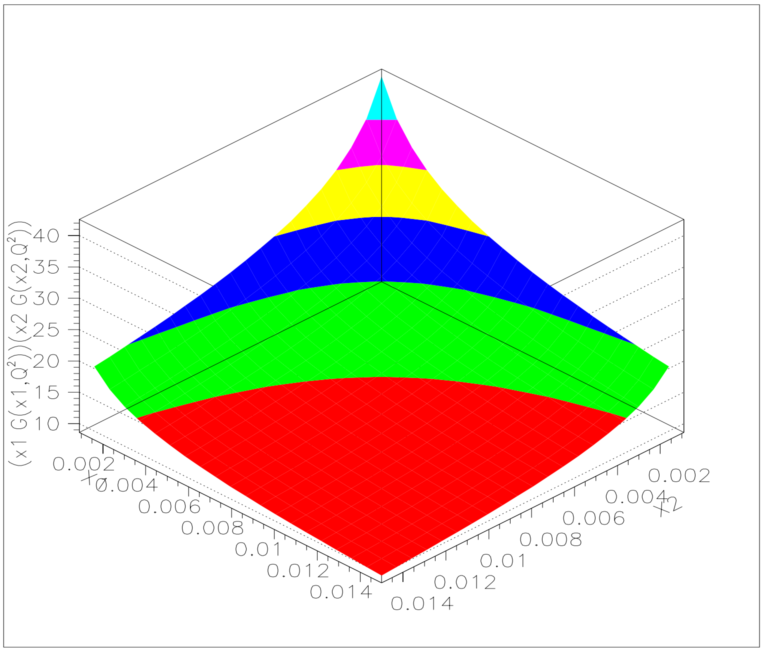

Figure 6.3: Two dimensional plot of $x_1 x_2 G(x_2, \mu_2^2)\ G(x_1, \mu_1^2)$.

In Figure 6.2 the basic kinematics of the subprocess and the variables used in the text are shown. At high p_T the dominant partonic subprocess should be the gluon-gluon interaction. The two dimensional plot of Figure 6.3 represents the product

$$x_1 x_2 G(x_2, \mu_2^2)\ G(x_1, \mu_1^2)$$

calculated at different scales μ_1^2, μ_2^2 In particular, setting $\delta y = 0$, i.e. restraining us to the diagonal $x_a = x_b = x$. Throughout this chapter we will assume this constraint.

As above-mentioned we shall require both rapidities (of the Υ and the recoiling jet) to be less than a common small value y_0: $|y_\Upsilon| < y_0$, $|y_{jet}| < y_0$. We could set $y_0 = 0.25$ for example, as discussed later.) Then $x_a \simeq x_b = x$, and

$$x^2 = \frac{\hat{s}}{s} \tag{6.5}$$

At high and very high p_T (i.e. $p_T^2 > 4m_b^2$) we can identify $\hat{s} \approx 4p_T^2$. (Hereafter we consider $p_T \geq 20$ GeV.) Therefore measuring the transverse momentum of the resonance should lead to the the knowledge of the momentum fraction x of the interacting partons, with a typical uncertainty

$$\frac{\Delta x}{x} = y_0 \tag{6.6}$$

Next, we will show that the (systematic) uncertainty associated to the determination of the Feynman x of the interacting partons in our proposed method, is given by the upper rapidity cut y_0 imposed on the resonance in all events, following the above expression: Assuming a gluon gluon scattering process into two final-state gluons, it is easy to see that any extra (longitudinal) rapidity amount Δy of any final-state parton, should be assigned to anyone of the two colliding partons, as a consequence of conservation of energy-momentum. (In this case the partonic reference frame would not longer coincide with the Lab frame.)

On the other hand, a parton carrying a fraction x of the total hadron momentum has a (longitudinal) rapidity

$$y = y_{hadron} - \log\frac{1}{x} \tag{6.7}$$

where y_{hadron} is the rapidity of the hadron in the Lab system.

Differentiating both sides of Eq.(6.7) and setting $\Delta y = y_0$, one gets easily the expression (6.6).

Let us observe that the rapidity cut $|y| < y_0$ binds us to a region of "allowed" transverse momentum, increasing with p_T since $x^2 s \simeq 4p_T^2$, and hence

$$\frac{\Delta p_T}{p_T} = y_0 \tag{6.8}$$

This means that as the transverse momentum grows, the p_T range compatible with the relative error, predetermined by choosing the value of y_0, grows too. If this value is set very low, the precision on the Feynman x increases but the price to be paid is probably reducing too much the statistics. Conversely, allowing y_0 to be *too large*, leads to larger statistics but spoiling the knowledge of x because of the uncertainty given by (6.6). As a compromise, we chose $y_0 = 0.25$ which, however, could be eventually varied depending on the size of the sample of collected events.

Now, turning back to the development of the idea, at high p_T the dominant partonic subprocess should be the gluon-gluon interaction. Thus the gluon density $G(x, \mu^2)$ in the proton will mainly be involved and we can write as a first approximation

$$\frac{d^3\sigma}{dy_\Upsilon dy_{jet} dp_T} = 2p_T \; x^2 \; G(x, \mu^2)^2 \; \frac{d\hat{\sigma}_{gg}}{d\hat{t}} \tag{6.9}$$

where we can choose, for example, $\mu^2 \; = \; \hat{s}$

6.1.2 The proposal

We propose [44] to study the ratios:

$$\frac{x_2^2 \; G(x_2, \mu_2^2)^2}{x_1^2 \; G(x_1, \mu_1^2)^2} \; = \; \left(\frac{d\hat{\sigma}_{gg}/d\hat{t}_1}{d\hat{\sigma}_{gg}/d\hat{t}_2} \right) \times \left(\frac{p_{T1}}{p_{T2}} \right) \times \left(\frac{d^3\sigma/dy_\Upsilon dy_{jet} dp_{T2}}{d^3\sigma/dy_\Upsilon dy_{jet} dp_{T1}} \right) \tag{6.10}$$

for a set of x_1, x_2 pairs and *different gluon distributions.* The number of pairs is basically limited by Δx, i.e. y_0, so this constraint cannot released too much.

Therefore the keypoint is to consider the left hand side (l.h.s) of the above equality (Eq. (6.10)) as an *input* corresponding to different sets of the gluon distribution for the proton, whose x dependence is hence assumed to be "known", and in fact would be tested. On the other hand the r.h.s. corresponds to an input from experimental data and some theoretical factors likely under control.

Let us remark that the x and μ^2 values are *not independent* in this proposal; indeed for each value of x, μ^2 is fixed by $\hat{s} = x^2 s$. However, notice that the scale can actually be varied by choosing a different assignment for μ^2, e.g. $\mu^2 = \hat{s}/4$.

Next we shall write expression (6.10) as

$$\frac{x_2^2 \; G(x_2, \mu_2^2)^2}{x_1^2 \; G(x_1, \mu_1^2)^2} \; = \; R_{theo} \times R_{exp} \tag{6.11}$$

where

$$R_{theo}(p_{t1}, p_{t2}, \mu_1^2, \mu_2^2) \;=\; f_{cor} \times \frac{d\hat{\sigma}_{gg}/d\hat{t}_1}{d\hat{\sigma}_{gg}/d\hat{t}_2} \tag{6.12}$$

notice that in this term we have incorporated some possible corrections through the f_{cor} factor - which could be calculated either analytically or by Monte Carlo methods - taking into account higher-order effects such as intrinsic k_T of the interacting gluons, AP evolution of the fragmenting gluons, etc.

Now, we evaluate

$$\frac{d\hat{\sigma}_{gg}/d\hat{t}_1}{d\hat{\sigma}_{gg}/d\hat{t}_2} \tag{6.13}$$

in the high p_T limit, taking Eq.(3.16) and the relations

$$\begin{aligned} \hat{t} \;&=\; -\frac{1}{2}(\hat{s} \;-\; M^2)\;(1 \;-\; cos\theta) \\ \hat{u} \;&=\; -\frac{1}{2}(\hat{s} \;-\; M^2)\;(1 \;+\; cos\theta) \end{aligned}$$

Requiring $|y| \simeq 0$, $(\theta \simeq \pi/2)$, in the high p_T region we have:

$$\hat{t} \simeq \; \hat{u} \simeq \; -\frac{1}{2}\hat{s} \tag{6.14}$$

then Eq. (3.16) reads

$$\overline{\sum}|\mathcal{A}(gg \to \Upsilon g)|^2 \;=\; \frac{162\;\pi^3\;\alpha_s^3}{M^3} < 0|O_8^{\Upsilon}(^3S_1)|0 > \tag{6.15}$$

and using Eq. (6.4) and $\hat{s} \approx 4p_T^2$ one obtains

$$R_{theo} \to f_{cor} \;\times\; \frac{\alpha_s^3(\mu_1^2)\;p_{T2}^4}{\alpha_s^3(\mu_2^2)\;p_{T1}^4} \tag{6.16}$$

explicitly showing that $\alpha_s(\mu^2)$ is entangled in the gluon density determination, and therefore must be consistent with the PDF parameters all together. On the other hand, note that the dependence on the NRQCD matrix elements does cancel in R_{theo}, but there is a dependence on the scales μ_1^2 and μ_2^2, which should match the same dependence in the l.h.s. of Eq. (6.11).

Aside, the experimental input reads as the ratio

$$R_{exp}(p_{T1},p_{T2},y_0) = \left(\frac{p_{T1}}{p_{T2}}\right) \times \left(\frac{d^3\sigma/dy_{\Upsilon}dy_{jet}dp_{T2}}{d^3\sigma/dy_{\Upsilon}dy_{jet}dp_{T1}}\right) \tag{6.17}$$

which can be obtained directly from experimental data.

6.1.3 Introducing the gluon quark contribution

Although expectedly dominant, the gluon gluon partonic subprocess is not the only α_s^3 contribution to the cross section yielding a fragmenting gluon into $\Upsilon(nS)$ at high p_T. Also gluon quark scattering $gq{\rightarrow}g^*q$ followed by $g^*{\rightarrow}\Upsilon(nS)X$, can give a sizeable contribution (about 20% at $p_T > 20$ GeV, see Table 5.2, chapter 5). Consequently, the expression (6.12) for the ratio of gluon densities has to be modified to include the quark distribution $q(x,\mu^2)$ in protons:

$$\frac{d^3\sigma}{dy_{\Upsilon}dy_{jet}dp_T} = 2p_T\left[x^2\ G(x,\mu^2)^2\ \frac{d\hat{\sigma}_{gg}}{d\hat{t}} + x\ G(x,\mu^2)x\ q(x,\mu^2)\frac{d\hat{\sigma}_{gq}}{d\hat{t}}\right] \tag{6.18}$$

putting $x^2\ G(x,\mu^2)^2$ in the l.h.s. and performing ratios at *different* p_T values, one easily obtains

$$\frac{x_2G(x_2,\mu_2^2)\ (x_2G(x_2,\mu_2^2)+k{\cdot}x_2q(x_2,\mu_2^2))}{x_1G(x_1,\mu_1^2)\ (x_1G(x_1,\mu_1^2)+k{\cdot}x_1q(x_1,\mu_1^2))}\ =\ R_{theo}\times R_{exp} \tag{6.19}$$

where R_{theo} is the same than in Eq.(6.12). Factor k takes into account the ratio of the gq and gg cross sections, both calculated at the same values of the Mandelstam variables $\hat{s}$ and $\hat{t}$ of the hard interaction, i.e.

$$k\ =\ \frac{d\hat{\sigma}_{gq}/d\hat{t}}{d\hat{\sigma}_{gg}/d\hat{t}} \tag{6.20}$$

becoming independent of x (and μ^2) at zero rapidity and large p_T: From Eq. (3.17) and making these assumptions

$$\overline{\sum}|\mathcal{A}(gq{\rightarrow}\Upsilon q)|^2\ =\ \frac{880\ \pi^3\ \alpha_s^3}{27\ M^3} < 0|O_8^{\Upsilon}(^3S_1)|0 > \tag{6.21}$$

Then, using the above equation and Eq. (6.15)

$$k \simeq 0.2$$

In order to control this factor we also calculated it in the region $p_T \sim M$: Taking the equations

$$\hat{t} \simeq \hat{u} \simeq -\frac{1}{2}(\hat{s} - M^2) \tag{6.22}$$

and using Eqs. (3.16-3.17), we found, for instance at $p_T = 20$ GeV a variation less than a 9% w.r.t. the massless limit.

Focusing on the k variations due to the rapidity uncertainties, we can compute this factor considering the highest allowed rapidity $|y| = 0.25$, i.e. $\theta \simeq 76^0$; then using

$$\begin{aligned} \hat{t} &= -\frac{1}{2}\hat{s}\,(1 - cos\theta) \\ \hat{u} &= -\frac{1}{2}\hat{s}\,(1 + cos\theta) \end{aligned}$$

in Eqs (3.16-3.17) one obtains a variation of $\simeq 10\%$ w.r.t. the one in the $|y| = 0$ case, i.e. $\theta = 90^0$.

Once controlled this k factor, one can write the density ratio (6.19) as

$$\frac{x_2^2\ G(x_2,\mu_2^2)^2(1 + k{\cdot}\lambda(x_2,\mu_2^2))}{x_1^2\ G(x_1,\mu_1^2)^2(1 + k{\cdot}\lambda(x_1,\mu_1^2))} \tag{6.23}$$

where

$$\lambda(x,\mu^2) = \frac{q(x,\mu^2)}{G(x,\mu^2)}$$

By Taylor expanding the above ratio, the leading term is

$$\frac{x_2^2\ G(x_2,\mu_2^2)^2}{x_1^2\ G(x_1,\mu_1^2)^2}\ (1 + r)$$

where

$$r = k\times\Big[\lambda(x_2,\mu_2^2) - \lambda(x_1,\mu_1^2)\Big]$$

should be a quite small quantity. We have checked with CTEQ4L that typically $r \approx 0.1$ for values between $x_1 = 3{\cdot}10^{-3}$ and $x_2 = 1.5{\cdot}10^{-3}$. Obviously, when a particular PDF would be tested its corresponding r factor calculation should be done.
Thereby, we can rewrite Eq. (6.19) as

$$\frac{x_2^2\ G(x_2,\mu_2^2)^2}{x_1^2\ G(x_1,\mu_1^2)^2}(1+r) = R_{theo} \times R_{exp} \tag{6.24}$$

Again the l.h.s. is an input from the PDF to be tested, while the r.h.s. comes from experimental data and some theoretical calculations without requiring the NRQCD MEs values.

6.2 Foreseen Statistics

From an experimental point of view it may happen that the discrimination among the different $\Upsilon(nS)$ states via mass reconstruction could become a difficult task, especially at very high p_T, because of the uncertainty on the measurement of the muons momenta [2]. Nevertheless, since we are proposing to study *ratios* of cross sections, we can consider the overall $\Upsilon(nS)$ inclusive production, without separating the different bottomonia sources - all the weighted matrix element canceling in the quotient if we neglect the mass differences between the different states. (Notice that at high p_T there is almost no contribution from the CSM.) In Figures 6.4 and 6.5 we show the combined differential cross section and integrated cross section production rate, respectively, at $p_T > 20$ GeV and $|y| < 0.25$ for the upper and lower values of the colour-octet matrix elements from Table 4.1, taking into account their errors. In Table 6.1 we show these values used together in the generation.

Assuming an integrated luminosity of 10 fb^{-1}, corresponding to one year running (10^7s) of LHC at “low” luminosity (10^{33} $\text{cm}^{-2}\text{s}^{-1}$) we can easily get the expected number of events from Figure 6.5, just by multiplying the ordinate by a factor 10^7. Thus we can see that the foreseen number of events

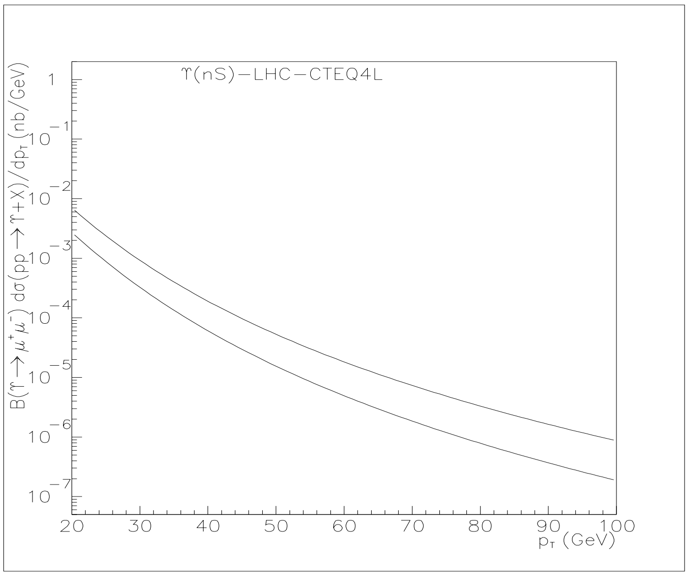

Figure 6.4: Predicted $\Upsilon(1S)+\Upsilon(2S)+\Upsilon(3S)$ weighted contributions to bottomonia inclusive production differential cross section at the LHC corresponding to the upper and lower MEs from Table 6.1, in the rapidity interval $|y| < 0.25$ and $p_T > 20$ GeV.

Table 6.1: Upper and lower values, including errors, of $< O_8^{\Upsilon(nS)}(^3S_1) > |_{tot}$; $n = 1, 2, 3$ (in units of 10^{-3} GeV^3) from the best fits to CDF data at the Tevatron on prompt $\Upsilon(nS)$ inclusive production.

Υ	Upper ME	Lower ME
$1S$	119	59
$2S$	130	11
$3S$	110	57

(aside efficiency reduction) at $p_T > 20$ GeV is about 10^5, whereas at $p_T > 40$ GeV is about 10^4. By extrapolation we get a meagre expected number of $\simeq 10^2$ events at $p_T > 100$ GeV. This makes unlikely any measurement for transverse momentum larger than 100 GeV, under the tight rapidity cut of 0.25 on the resonance which we are imposing.

In view of the foreseen rates of bottomonia production at the LHC we

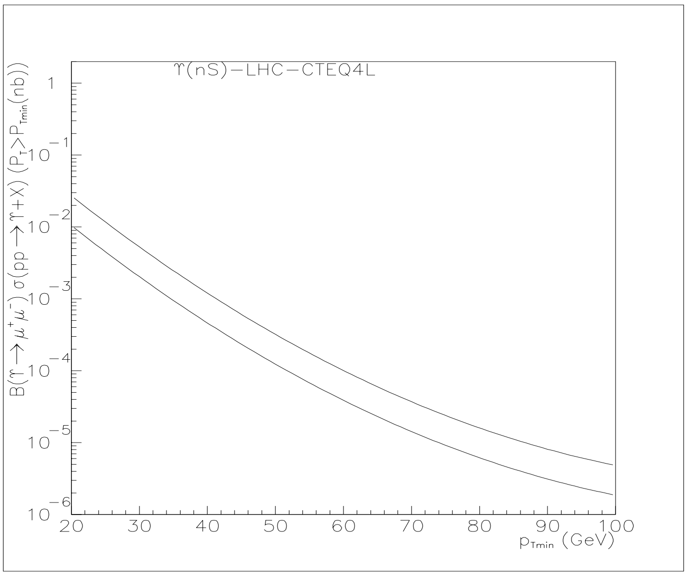

Figure 6.5: Predicted $\Upsilon(1S)+\Upsilon(2S)+\Upsilon(3S)$ weighted contributions to bottomonia inclusive production integrated cross section at the LHC corresponding to the upper and lower MEs from Table 6.1, in the rapidity interval $|y| < 0.25$ and $p_T > 20$ GeV.

propose testing the shape of the gluon density in protons for x values ranging in the interval: $3{\times}10^{-3}$ *to* $1.5{\times}10^{-2}$, using $x = \sqrt{\hat{s}/s}$ from $p_T = 20$ GeV up to $p_T = 100$ GeV, under the rapidity constraint $y < 0.25$.

Nevertheless, by removing the condition $|y| < 0.25$ statistics could considerably be enlarged. Since our proposal essentially relies on the determination of the Feynman x of the interacting partons by measuring the p_T of the final products of the reaction, there is still the possibility of requiring a back-to-back topology but sweeping the whole accessible rapidity region $|y| < 2.5$, instead of limiting ourselves to the central rapidity values. This goal can be achieved by selecting events with the muon pair and the recoiling jet (see Fig. 6.1) sharing common values of p_T and absolute rapidities, within the uncertainties. In other words, events could be accepted with both $\Upsilon(nS)$ and recoiling jet rapidities satisfying $||y_\Upsilon| - |y_{jet}|| < 0.25$; in such a way statistics should increase by a factor $\simeq 10$, possibly extending the allowed region of p_T up to higher values than 100 GeV, and hence reaching

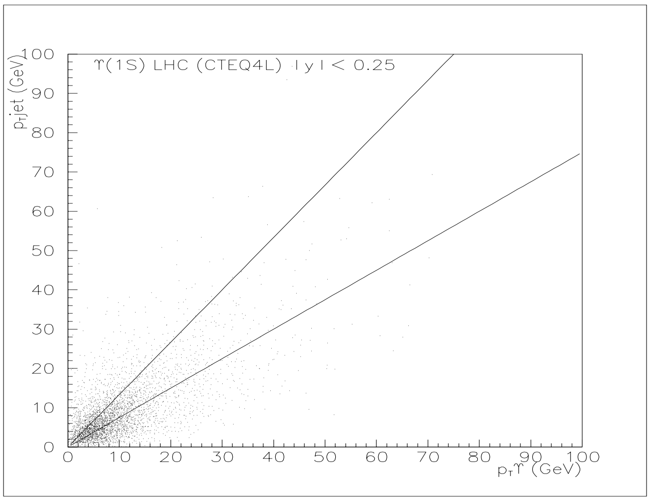

Figure 6.6: Plot of the jet transverse momentum versus the $\Upsilon(1S)$ resonance transverse momentum at LHC energy (parton/particle level simulation) using the PYTHIA algorithm to simulate initial-state radiation. The two straight lines indicate the allowed region according to the p_T uncertainty obtained from Eq. (6.8) for $y_0 = 0.25$.

larger values of the momentum fraction x.

As a final remark, if the colour-octet mechanism is confirmed and the corresponding MEs accurately and consistently extracted from other experiments like Tevatron or HERA - or theoretically computed - one can consider then the possibility of unfolding the gluon density from the measured cross section as proposed, for instance, in Ref. [45] by means of D^* meson production at HERA. In such a case, our proposal [44, 46, 47] would extend beyond the study of ratios, allowing the extraction of gluon and quark densities directly from heavy quarkonia production mechanisms.

6.3 Rapidity cut and azimuthal correlations

In order to get an idea of the expected impact of the intrinsic k_T on the topology of events, we show in Figures 6.6 and 6.7 several plots of the

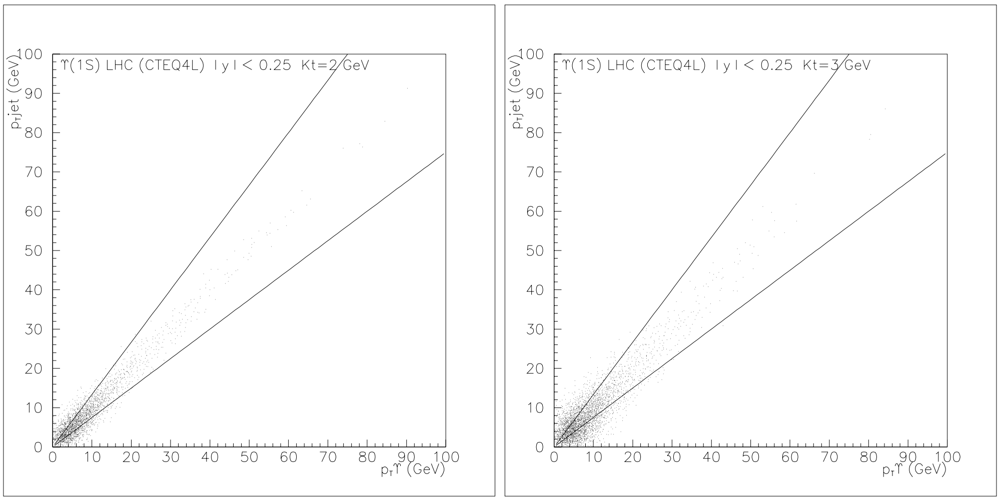

Figure 6.7: Plots of the jet transverse momentum versus the $\Upsilon(1S)$ resonance transverse momentum at LHC energy (parton/particle level simulation) using, from left to right: *a)* a gaussian smearing function with $< k_T >= 2$ GeV and *b)* $< k_T >= 3$ GeV. The two straight lines indicate the allowed region according to the p_T uncertainty obtained from Eq. (6.8) for $y_0 = 0.25$.

transverse momenta of the $\Upsilon(1S)$ resonance versus the recoiling jet. In the absence of any higher order QCD effect, events squeeze along the diagonal. However k_T smearing spreads events over a larger area in the plot, spoiling somehow a naive picture of a back-to-back topology coming from a collinear approximation to leading order; Figure 6.6 corresponds to initial-state radiation activated in the PYTHIA generation following the model developed in [31]. Alternatively, Figures 6.7-a) and 6.7-b) show the effect of a gaussian spread of $< k_T >= 2$ GeV and $< k_T >= 3$ GeV, respectively. The region inside the two straight lines corresponds to an uncertainty on p_T given by Eq. (6.8) for a rapidity value $y_0 = 0.25$. Although at small and moderate p_T (say, $p_T \leq 10$ GeV) all plots essentially agree, at higher p_T the former one, corresponding to a full simulation of gluon emission in the initial-state performed by PYTHIA, displays much more events outside the accepted region.

In Table 6.2 we show the fractions of events inside the allowed region

Table 6.2: Fraction (in %) of events inside the region defined by the two straight lines for different p_T lower cuts (in GeV) applied to the resonance, corresponding to Fig. 6.6, i.e. initial-radiation generated by PYTHIA.

p_T cut-off:	10	20	30	40	50
% “inside”	39 ± 1	38 ± 3	35 ± 5	38 ± 9	38 ± 15

between the two straight lines in the plot 6.4 (initial-state radiation on). We observe that about 40% of all events are “accepted”, remaining practically constant above $p_T = 10$ GeV. Finally we conclude that such reduction factor (of the order of 40%) does not represent in itself a dramatic loss of statistics regarding our proposed method to probe the gluon density in protons. On the other hand, for the gaussian smearing, the situation is even much more optimistic.

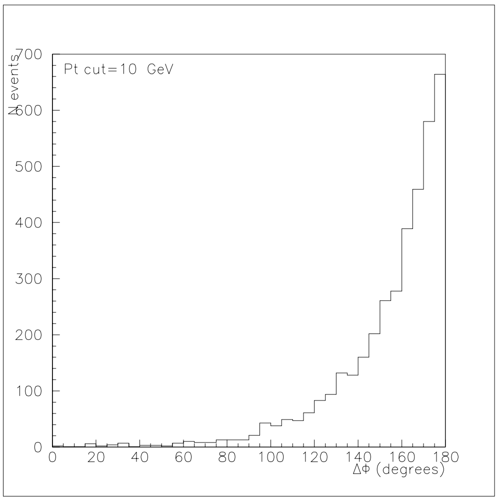

Figure 6.8: Azimuthal angle between the recoiling jet direction (defined by the parent gluon momentum) and the dimuon direction from $\Upsilon(1S)$ decays in the transverse plane using Initial-state radiation activated in PYTHIA. All plotted events were selected with $\Upsilon(1S)$ transverse momentum greater than 10 GeV.

In Figures 6.8 and 6.9 we show the azimuthal $\Delta\phi$ angle between the

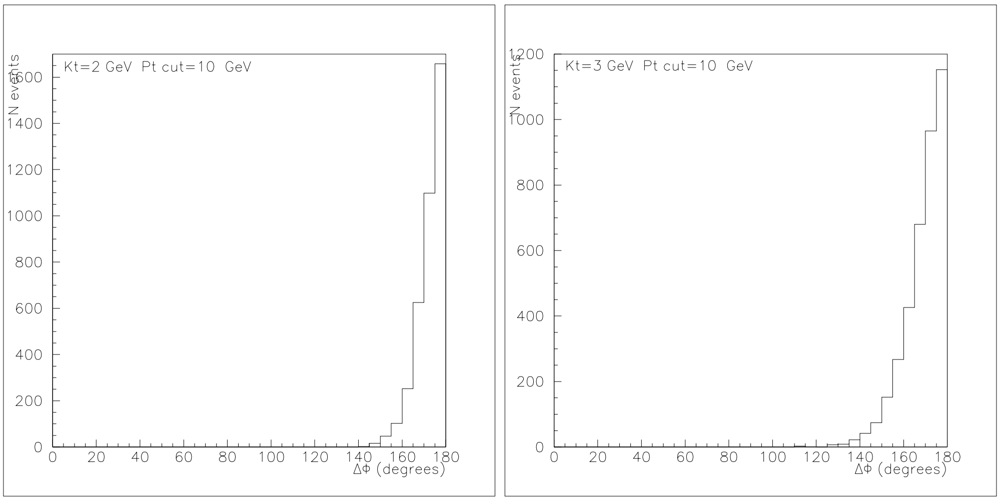

Figure 6.9: Azimuthal angle between the recoiling jet direction (defined by the parent gluon momentum) and the dimuon direction from $\Upsilon(1S)$ decays in the transverse plane, from left to right: *a)*: Using gaussian smearing with $< k_T >= 2$ GeV; *b)* The same with $< k_T >= 3$ GeV. All plotted events were selected with $\Upsilon(1S)$ transverse momentum greater than 10 GeV.

muon pair direction (defining the direction of the fragmenting gluon into bottomonium) and the recoiling jet generated by the final-state gluon, for different values of the effective k_T, in correspondence with Figures 6.6 and 6.7. In Fig. 6.8 we used the PYTHIA algorithm for initial-state radiation, whereas in Figures 6.9-a) and 6.9-b) we used a smearing gaussian with $< k_T >= 2$ GeV and $< k_T >= 3$ GeV, respectively. As expected, again we realize the sizeable effect of the effective k_T effect on the distribution, especially in the former case. Nevertheless, most events should display a clear enough back-to-back signature as regards the $\Delta\phi$ variable (in addition to the p_T balance), as indicated by the peak at 180 degrees in all plots of Figures 6.8 and 6.9.

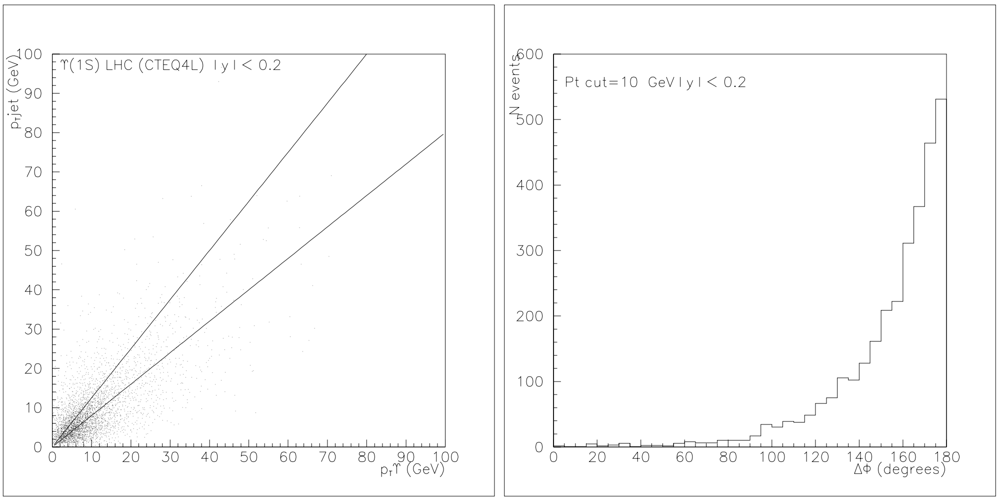

Figure 6.10: *a)* Plot of the jet transverse momentum versus the $\Upsilon(1S)$ resonance transverse momentum at LHC energy (parton/particle level simulation) using the PYTHIA algorithm to simulate initial-state radiation; *b)* Azimuthal angle between the recoiling jet direction (defined by the parent gluon momentum) and the dimuon direction from $\Upsilon(1S)$ decays in the transverse plane.

6.4 Difference in shape of several PDFs

This section is devoted to make more specific and go deeply into our proposal. First, in order to increase the number the experimental points to be tested, we reduce the the value of the rapidity interval to be $y_0 = 0.2$ (this means $\theta \simeq 79^0$), with this small reduction all the assumptions remain still valid; however we will repeat the above analysis for the most relevant features.

In order to get an idea, again, of the expected impact of the intrinsic k_T on the topology of events, we show in Figure 6.10-a) a plot of the transverse momenta of the $\Upsilon(1S)$ resonance versus the recoiling jet. This time the region inside the two straight lines corresponds to an uncertainty on p_T given by Eq.(6.8) for a rapidity value $y_0 = 0.2$.

In Table 6.3 we show the fractions of events inside the allowed region

Table 6.3: Fraction (in %) of events inside the region defined by the two straight lines for different p_T lower cuts (in GeV) applied to the resonance, corresponding to Fig. 6-10-a), i.e. initial-radiation generated by PYTHIA.

p_T cut-off:	10	20	30	40	50
% “inside”	36 ± 1	34 ± 2	32 ± 4	36 ± 7	38 ± 12

between the two straight lines in the plot 6.10-a) (initial-state radiation on). We observe that about 35% of all events are “accepted”, remaining practically constant above $p_T = 10$ GeV. Again, we conclude that such reduction factor does not represent in itself a dramatic loss of statistics regarding our proposed method to probe the gluon density in protons. On the other hand, if a gaussian smearing is used, the situation, is even much more optimistic, as in the former analysis. Figure 6.10-b) shows the azimuthal angle between the dimuon and jet directions, using the initial radiation mechanism.

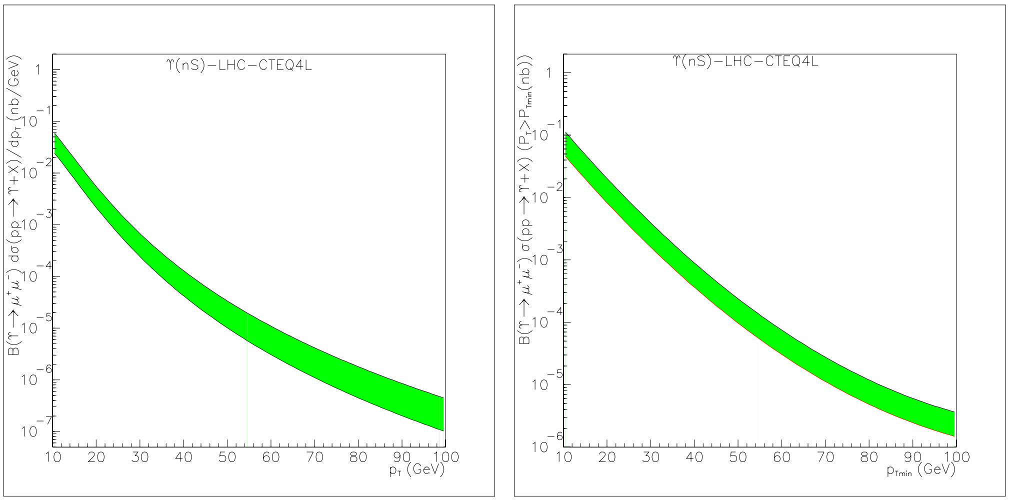

Figure 6.11: Predicted $\Upsilon(1S)+\Upsilon(2S)+\Upsilon(3S)$ weighted contributions to bottomonia inclusive production at the LHC in the rapidity interval $|y| < 0.2$ and $p_T > 10$ GeV. *a)*: differential cross section; *b)*: integrated cross section.

Concerning the overall $\Upsilon(nS)$ inclusive production, without separating the different bottomonia sources (see section 6.2), in Figure 6.11 we show the combined production rate at $p_T > 10$ GeV and $|y| < 0.2$ for the upper and lower values of the colour-octet matrix elements provided in Table 6.1.

6.4.1 Efficiencies, statistics and expected accuracy

Above, we have pointed out that, in order to determine x with the expected accuracy, we are required to reject events not satisfying the $\Delta p_T/p_T$ constraint. This meant a reduction factor of about 35%.

Besides, reconstruction of the $\Upsilon(nS)$ mass from the $\ell^+\ell^-$ pair implies another reduction factor of about 80% for the $\mu^+\mu^-$ channel and 50% for the e^+e^- channel [1]. These figures do not include the lepton trigger and identification efficiencies which altogether roughly amount to 0.85 for the triggering muon and 90% for the other one and 75% for each single electron [2]. This means that the electronic channel represents about 1.5 of the muonic one.

Therefore, the overall efficiency factor taking into account both the muonic and electronic channels can be estimated as

$$\epsilon_{reconst} \;=\; 0.8 \;\times\; 0.85 \;\times\; 0.95 \;\times\; 1.5 \simeq\; 1. \tag{6.25}$$

Jet reconstruction efficiency, ϵ_{jet}, amounts on the average to about 75% in the range under consideration. Moreover, since the probability to accept events according to $\Delta p_T/p_T$ is $\epsilon_p \simeq 35\%$, the reduction factor to be applied is

$$\epsilon_{tot} \;=\; \epsilon_{reconst} \times \epsilon_{jet} \times \epsilon_p \;=\; 1. \times 0.75 \times 0.35 \simeq 0.26 \tag{6.26}$$

Assuming an integrated luminosity of 10 fb^{-1}, corresponding to one year running (10^7s) of LHC at "low" luminosity (10^{33} $\text{cm}^{-2}\text{s}^{-1}$) we can easily

---

[1] These are values very close to J/ψ leptonic decay [2].

get the expected number of events per year from Figure 6.11-b), just by multiplying the ordinate by a factor 10^7. Thus we can see that the foreseen number of events at $p_T > 80$ GeV is slightly larger than 10^3 as a central value. Applying the total efficiency factor we get

$$260 \textit{ events per year run}$$

Hence, after three years running the accumulated statistics would amount to about 800 events, basically fixing the typical relative uncertainty of the order of 3.5% which essentially sets the "discrimination level" to be applied to different sets of PDFs, as we shall see in the next point.

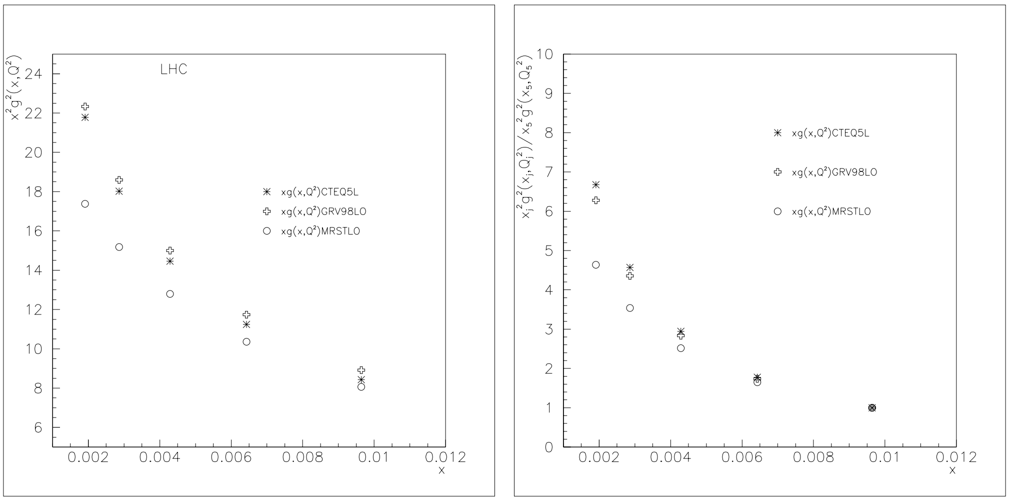

Figure 6.12: a) Values of $x_i G(x_i, \mu_i^2)$ for different leading order PDFs. b) Values of $x_i^2 G^2(x_i, \mu_i^2)/x_5^2 G^2(x_5, \mu_5^2)$, i.e. values of $x_i^2 G^2(x_i, \mu_i^2)$ normalized to the rightmost point ($i = 5$).

6.4.2 Discriminating among different PDFs

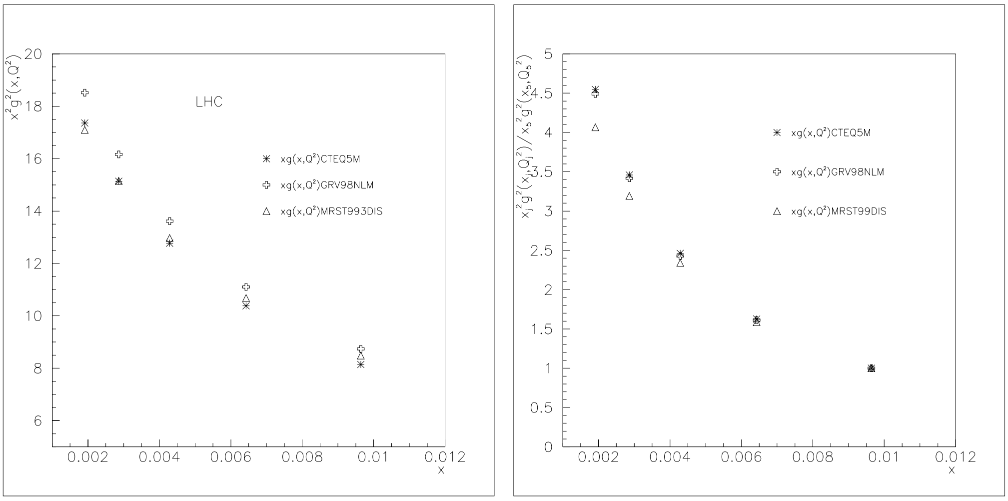

Figure 6.13: a) Values of $x_iG(x_i,\mu_i^2)$ for different next-to-leading order PDFs. b) Values of $x_i^2G^2(x_i,\mu_i^2)/x_5^2G^2(x_5,\mu_5^2)$, i.e. values of $x_i^2G^2(x_i,\mu_i^2)$ normalized to the rightmost point ($i=5$).

Now, we will get an idea about the difference in shape of the PDFs to be tested. This check is mandatory since, if such PDFs are squeezed in a "region" smaller than the one governed by the errorbars of the experiment, this test would be not possible; i.e. all PDFs would be compatible with experimental results. Currently , There are mainly three major groups - namely CTEQ, MRST and GRV - providing regular updates of the partonic structure of protons as new data and/or theoretical improvements become available.

In Figures 6.12-6.13 we show the expected shapes corresponding to different gluon densities of the proton, obtained from [48]. We have normalized all distributions to the rightest point, i.e. $x = 0.00964$ corresponding to $p_T \simeq 70$ GeV. Notice that from the behaviour of the gluons distribution in protons, the actual values are quite close even for different PDFs.

Figure 6.12 stands for leading-order PDFs. As one can see, at low x

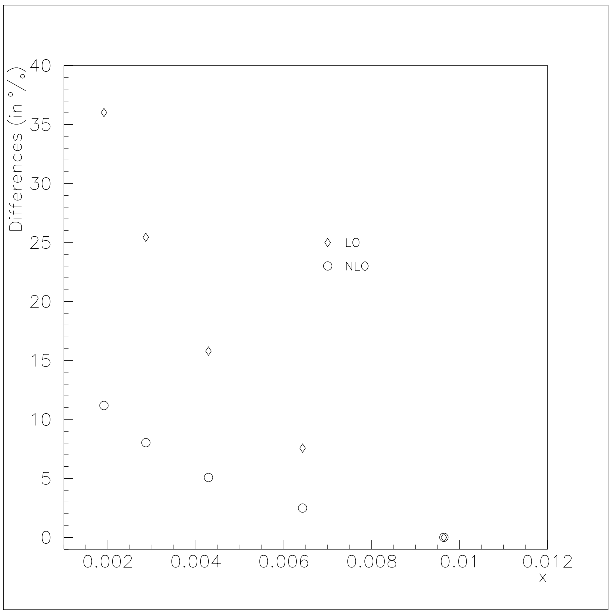

Figure 6.14: Differences (in %) between current "normalized" LO and NLO PDFs corresponding to the upper and lower values of figures 6.12-b and 6.13-b respectively.

($x \simeq 10^{-3}$) there are differences, between CTEQ and MRST PDFs, up to the order of 30% in the $x = 0.001$ region.

On the other hand Figure 6.13 corresponds to next-to-leading order PDFs. Now the differences, between CTEQ and MRST PDFs again, have stretched to values of the order of 6% at most for the $x = 0.001$ region. In Figure 6.14 we present the maximum difference for both LO and NLO PDFs from Figures 6.12-b) and 6.13-b).

Therefore with the foreseen precision level of 3.5% likely it will be possible to discriminate among LO PDFs, but somehow more difficult for NLO ones. However one might extend the analysis down to a lower x region. Even though, we conclude that this measurement seems feasible.

Conclusions

In this work, we have studied the main issues concerning the $\Upsilon(nS)$ hadroproduction. We have discussed the best way to determine the long-distance parameters related to bottomonia hadroproduction according to our Monte Carlo study. We have analyzed higher QCD effects in order to get an idea about the expected impact of such effects:

- **Tevatron Analysis**
- To this end we have studied the effects of the initial radiation and intrinsic Fermi motion of parton mechanisms provided by PYTHIA, using CTEQ4L PDF in our bottomonia scenario.
- We have analyzed the AP evolution mechanism of the fragmenting gluon into a hadron, providing in the original PYTHIA software a code to reproduce this feature in each $\Upsilon(nS)$ generation.
- We have investigated the Gaussian k_T smearing: using the PYTHIA primordial k_T smearing mechanism we compared such effect with the initial state radiation .
- We provided a new code to implement the COM in PYTHIA to take into account the full contribution in bottomonia hadroproduction i.e. COM $gg-gq-q\overline{q}$ contributions in Υ hadroproduction. We modified as well the "older" PYTHIA software to include CSM gg contribution in Υ hadroproduction. All these implementations were done respecting, as much as possible, the PYTHIA philosophy.

- Focusing on the analysis of the Υ hadroproduction from Tevatron data, we used CTEQ4L PDF (in order to make a comparison we also employed CTEQ2L) to extract some relevant NRQCD MEs for the bottomonia family: We payed attention to the cross section factorization problem. Since we were worried about this issue, we provided different MEs values at different p_T lower cut-offs. We realized that the shape of the fitted differential cross section becomes "steeper" in the low p_T region w.r.t. the fits using CTEQ2L, likely due to the BFKL style rise of CTEQ4L PDF at low x values versus CTEQ2L that follows a DGLAP evolution. The values of such MEs using CTEQ4L have been lowered w.r.t. the CTEQ2L case (we can roughly say that they lie around 10^{-1}). Therefore we can conclude that such values are still somewhat sensitive to the choice of the PDF. In spite of all this, we obtained generally good fits with χ^2/N_{df} near to one, excepting for the $\Upsilon(2S)$ case that comes out to be the worst one. The reason perhaps is that some branching ratios for $\chi_{bJ}(2P)$ contributions are overestimated, due to their big uncertainties. This feature jointly with the BFKL style rise, that "peaks" the CSM contribution in a way that almost saturates the low p_T region, bind us to lower likely too much the value of such $\Upsilon(2S)$ colour-octet ME.

- Concerning the $\Upsilon(1S)$, the ME values are consistent and their χ^2/N_{df} quite good, although in the low p_T region, the fit is slightly spoiled by the CSM feed-down source uncertainties, together again with the arguable behaviour of the PDF at low p_T.

- The best fit corresponds to the $\Upsilon(3S)$ case, since is the cleanest one, for expectedly it has no feed-down either from CSM or from COM sources. The fits are very good for all p_T cuts and COM contributions early becomes dominant.

- We realize that in all Υ fits the linear combination of matrix elements M_5 is not needed in the fit with CTEQ4L. This is consistent with the CTEQ2L case, in which case the M_5 value was near to zero too.

- Another important conclusion concerning the separated production sources, is that, using the Tevatron data for production sources at $p_T \geq 8$ GeV, we found that for the $\Upsilon(1S)$ case all the COM contribution comes from Υ's and, conversely, the $\chi_{bJ}|_{COM}$ contribution appears to be very small, in contrast to other authors' results.

- Even though we have been able to provide (from our generation) values of the separated contributions to the integrated cross sections (with a p_T-cut ≥ 1 GeV), we disentangled the sources for each Υ resonance: The CSM contribution becomes, for $p_T \geq 1$ GeV, $80, 76$, and 33% for Υ(1S), Υ(2S) and Υ(3S), respectively, but this contribution is mainly constrained at the low p_T region. Concerning the COM contributions, for all bottomonia resonances and for $p_T \geq 8$ GeV, we realize that the $gg - gq - q\bar{q}$ contributions are $69, 30$, and 1%, respectively.

- Regarding the NRQCD velocity rules, we realized that the particular NRQCD velocity scaling rule - the extraction of the v^4 value - studied in this work, although valid as an order-of-magnitude estimate, retains a weak dependence on the principal quantum number n. This can be easily understandable if looking at the MEs as squared wavefunctions at the origin.

- On the effects of the initial radiation state, we can conclude that, if they are taken into account, the values of the NRQCD have to be lowered with respect to the ones obtained without considering this feature. The reason is that a distribution generated taking into account this effect actually enhances the high p_T tail. Thus, in order to refit the former to the experimental points, the COM contribution has to be lowered. We have also studied the equivalence between PYTHIA initial-state radiation machinery and its corresponding (to our belief simpler but naive) gaussian $< k_T >$ smearing, finding a equivalence between the PYTHIA mechanism and a gaussian for $< k_T >= 1.8$ GeV.

- Another noticeable feature is the impact of AP evolution of the fragmenting gluon: We realized that, for the bottomonia case, its main effect starts from about 10 GeV amounting to a factor of the order of $\simeq 1/2.5$ at high p_T.

- **LHC Predictions**

- Stretching out energies and kinematic conditions of the analysis at Tevatron using CTEQ4L, we performed predictions at LHC on bottomonia hadroproduction, providing: The expected differential and integrated cross sections for each Υ resonance, as well as a prediction - extrapolating the available information on production sources at Tevatron - about direct $\Upsilon(1S)$ production. We can say that COM contributions to these cross sections are, at intermediate and high p_T, the dominant ones, as expected; this feature is especially noticeable for the $\Upsilon(3S)$ case. Concerning the COM contributions, for all bottomonia resonances and for $p_T \geq 8$ GeV, we realize that the $gg - gq - q\overline{q}$ contributions are $80, 20$, and $\sim 0\%$, respectively.

- We presented also predictions on total cross sections for $p_T \geq 1$ GeV, for all resonances; we also presented each single contribution in the generation.

- We showed the ratios between total cross sections of the resonances and, comparing them with the ones at Tevatron, these quotients suggest that the main dependence of their values (in similar kinematic conditions; i.e. taking either Tevatron or LHC conditions), is carried by the non-perturbative terms.

- **Gluon Density in Proton**

- It is universally recognized the importance of knowing the range of uncertainties of parton distributions, - especially in the case of the proton - with the advent of high energy, high luminosity proton colliders. The possibility of using different direct determinations of the gluon density by means of distinct processes, would allow the determination of systematic and theoretical errors as well as putting astringent constraints to global fits where DIS data play a central role.

- Taking into account this fact, we have presented a proposal to probe the gluon density in the proton using bottomonia hadroproduction at the LHC, providing the most relevant features needed in the proposal, as well as curves and statistics for $\Upsilon(nS)$ events. We also considered the possibility of to improve such statistics up to a factor 10 by sweeping the whole range of the rapidity by means the condition $||y_{\Upsilon}| - |y_{jet}|| <0.25$.

- In order to get an idea of the expected impact of the intrinsic k_T on the topology of events (loosing the idealistic back-to-back topology in the transverse plane), we have presented several plots of the transverse momenta of the $\Upsilon(1S)$ resonance versus the recoiling jet, over different conditions (initial radiation mechanism and gaussian smearing with different $< k_T >$ values), showing that such impact in itself does not imply a dramatic loss of statistics ($\simeq 40\%$), even in the worst case.

- A study on azimuthal correlations in order to discriminate the back-to-back topology has been also presented, over the different conditions above mentioned, seeming that this topology is adequate, without a dramatic loss of statistics again.

- Finally, to become more definite our proposal and going deeply into our proposal, we made the following study: First, in order to increase the number of experimental points along the total rapidity range, 2.5 for LHC, we reduce the value of the rapidity interval to be $y_0 = 0.2$. Later we provided a study on the most relevant, both LO and NLO PDFs, as well as an estimation on the detector effects,and therefore getting an idea of the final number of the expected number of events.

- In view of the foreseen rates of bottomonia production at the LHC, we propose testing the shape of the gluon density in protons for x values ranging in the interval: $2.1{\times}10^{-3}$ *to* $1.2{\times}10^{-2}$, using $x = \sqrt{\hat{s}/s}$ from $p_T \simeq 15$ GeV up to $p_T \simeq 85$ GeV.

- We have seen that the expected discrimination power for the foreseen statistics collected after three years of data-taking at the LHC (at "low" luminosity) should be enough to distinguish among different sets of PDFs. We have been rather conservative in our estimates of expected number of events and efficiencies. In spite of that, we conclude that our proposal can be useful as a direct probe of the gluon density in protons after several years of data taking at the LHC.

- On the other hand, although the universality of the colour-octet matrix elements is not definitely established, one could expect that MEs obtained in the same kind of hadronic process but at a different energy scale (i.e. hadroproduction at the Tevatron) should be reliable once used at LHC energies, under the same theoretical inputs (e.g. the charm mass, factorization scales, etc). This would mean the possibility of extracting PDFs be means of an unfolding procedure from heavy quarkonia hadroproduction at the LHC after a prior fit to Tevatron data. We are aware that such proposal requires a lot of additional work, constituting a first step where we study its feasibility in ATLAS experiment at the LHC.

Conclusiones

En esta memoria hemos estudiado las principales cuestiones acerca de la hadroproducción (HP) de las resonancias $\Upsilon(nS)$. Hemos discutido cómo determinar los parametros de larga distancia (no perturbativos) relacionados con el botomonio de acuerdo a nuestro estudio Monte Carlo. Además, se han analizado los efectos de orden superior de QCD con el fin de establecer su impacto en las simulaciones:

- **Estudio de los datos de Tevatron**

- Así, se han estudiado los efectos de la radiación inicial y del movimiento intrínseco de los partones de Fermi que PYTHIA incorpora.

- Mediante el estudio de la evolución AP del gluón fragmentándose en la resonancia Υ (más gluones adicionales) hemos añadido al programa original un nuevo código que lo capacita para reproducir este efecto (dentro de la filosofía de PYTHIA) en cada generación, siempre que se desee.

- Se ha investigado el efecto llamado de radiación mediante un k_T gaussiano, comparando éste con el mecanismo de radiación inicial.

- Hemos incorporado un nuevo código en PYTHIA que lo dota para evaluar la contribución del COM en la HP de bottomonia, además hemos modificado algunas rutinas de PYTHIA con el fin de reproducir la contribuciones gg del CSM y las $gq-q\overline{q}$ del COM. Estas adiciones y modificaciones han sido hechas respetando, en la medida de lo posible, la filosofía del generador original.

- Por lo que a la etapa de análisis se refiere, se ha investigado la HP de Υ empleando los datos de Tevatrón, y haciendo uso de la PDF CTEQ4L (y para comparar también CTEQ2L), hemos extraído los valores de los elementos de matriz de NRQCD más relevantes en la HP de Υ. Debido al problema que origina la imprecisión de la escala de factorización, se ha decidido ajustar dichos elementos de matriz escogiendo diferentes cortes inferiores de p_T. Se ha constatado, de los ajustes, que la forma de la secciones eficaces diferenciales es más pronunciada en el caso de CTEQ4L respecto a las de CTEQ2L, principalmente debido a que la PDF CTEQ4L sigue a bajo x una evolución del tipo BFKL, mientras que en caso de CTEQ2L se sigue un evolución DGLAP. Los valores de los elementos de matriz usando CTEQ4L bajan con respecto al caso CTEQ2L (pero diremos que siguen manteniendo el orden de magnitud, 10^{-1}) la razón de esta bajada es precisamente este comportamiento BFKL de la primera. Podemos concluir pues que los valores de los elementos de matriz son aún algo dependendientes de la elección de la PDF. Pero con todo, se obtienen unos buenos ajustes, con unas χ^2/N_{df} cerca de uno. La excepción está en el caso de $\Upsilon(2S)$ que resulta ser el peor. La razón es, quizás, la unión de dos efectos: por una parte se tiene que para algunas fuentes de producción de esta resonancia, como $\chi_{b0}(2P)$, las incertidumbres de la probabilidad de desintegración a $\Upsilon(2S)$ son grandes, esto ocasiona el que quizás se esté sobreestimando la contribución CSM, que es dominante en la zona de bajo p_T. A esto hay que unirle el comportamiento BFKL de la PDF en dicha zona, que amplifica el efecto "elevando" la distribución de forma que con el valor resultante casi satura la región de bajo p_T, obligando de esta forma a bajar, probablemente demasiado, el valor de los elementos de matriz de octete de color de $\Upsilon(2S)$.

- Por lo que a $\Upsilon(1S)$ atañe, los valores de los elementos de matriz ajustados son consistentes, y sus χ^2/N_{df} son bastante buenas a pesar que, a bajo p_T, el ajuste también se estropea algo debido a las incertidumbres de algunas fuentes de producción unido al discutible comportamiento de la PDF en la zona de bajo p_T.

- El mejor ajuste es para el caso de $\Upsilon(3S)$, debido a que es el más limpio por tratarse de producción directa, es decir no se esperan contribuciones de fuentes superiores (CSM o COM). Los ajustes son buenos para todos los cortes de p_T. También se constata que la contribución COM, incluso a bajo p_T, es la dominante.

- Por otra parte, hay que destacar que la combinación lineal de elementos de matriz M_5 no es necesaria para el caso del ajuste de CTEQ4L, y en el caso de CTEQ2L esa combinación tiene un valor muy bajo, cerca de cero tambien.

- Otra conclusión importante es que, usando la información disponible de Tevatrón para la separación de fuentes de producción de $\Upsilon(1S)$ para $p_T \geq 8$ GeV, encontramos que para esta resonancia la fuente del COM es producción directa de $\Upsilon(1S)$, y, por el contrario, la contribución $\chi_{bJ}|_{COM}$ resulta ser muy pequeña en contraste con los resultados ofrecidos por otros autores.

- Con todo, en este trabajo, se han dado valores (para un corte de $p_T \geq 1$ GeV) de las contribuciones a la seción eficaz total integrada, para cada resonancia. La contribución del CSM, para un $p_T \geq 1$ GeV, es $80, 76$, y 33% en Υ(1S), Υ(2S) y Υ(3S), respectivamente, situada mayormente en la zona de bajo p_T . Por lo que al COM se refiere, para un corte $p_T \geq 8$ GeV obtenemos que las contribuciones $gg - gq - q\overline{q}$ son $69, 30$, y 1%, respectivamente.

- Refiriéndonos a las reglas de escala de velocidades, diremos de la aquí estudiada (la extraccion del valor de v^4), que hemos comprobado su validez como una estimación del orden de magnitud, aunque constatamos que se mantiene una dependencia residual con el número cuántico principal n. Este hecho puede entenderse si se consideran los elementos de matriz como funciones de onda (al cuadrado, es decir probabilidades) en el origen.

- Sobre los efectos en este análisis de la radiación inicial, brevemente concluimos que si este efecto se tiene en cuenta en la generación de las resonancias, el valor de los elementos de matriz de NRQCD se deben bajar. La razón estriba en que la radiación inicial, realmente, eleva el valor de la distribución en la zona de alto p_T, por tanto, para reajustar la distribución se debe de bajar la contribución del COM. Por otra parte también hemos estudiado la equivalencia entre la maquinaria de radiación inicial de PYTHIA y su correspondiente (a nuestro parecer más simple pero menos elaborado) efecto del $< k_T >$ gaussiano: en el ajuste a los puntos experimentales hemos encontrado que la radiación inicial es equivalente a un $< k_T >$ gaussiano de valor $< k_T >= 1.8$ GeV.

- Otra característica notable es el impacto de la evolución AP del gluón fragmentándose en el hadrón: hemos constatado que, para el caso del botomonio, este efecto es patente a partir de unos 10 GeV, siendo un factor del orden de $\simeq 1/2.5$ en la zona de alto p_T.

- **Predicciones para LHC**

- En otro apartado, extrapolando los resultados de este análisis en Tevatrón a energías y condiciones cinemáticas de LHC, se han realizado predicciones acerca de la HP de Υ dando valores de las secciones eficaces diferenciales e integradas esperadas para cada resonancia. También se ha hecho una predicción - llevando el análisis hecho para Tevatrón a energías de LHC - de la producción directa de $\Upsilon(1S)$. Podemos decir que a medio y alto p_T la contribución COM es la dominante, como cabía esperar. Esta dominancia es especialmente notoria en el caso de $\Upsilon(3S)$. Centrándonos en el COM diremos que las contribuciones ($p_T \geq 8$ GeV) para $gg - gq - q\overline{q}$ son $80, 20$, y $\sim 0\%$, respectivamente.

- También damos predicciones de las secciones eficaces totales y contribuciones (para $p_T \geq 1$ GeV) para todas las resonancias.

- Se han calculado los cocientes de las secciones eficaces inclusivas, comparando éstas con las hechas en Tevatrón. Constatamos que los valores son prácticamente iguales, es decir que parece haber una muy débil dependencia de la parte cinemática en condiciones similares, es decir los cocientes hechos a energías de LHC, o bien hechos en el entorno de Tevatrón. En condiciones similares pues, los valores de dichos cocientes parecen estar determinados por la parte no perturbativa.

- **Sondeo de la Densidad de Gluones**

- Con el advenimiento de los aceleradores de protones de alta energia, y en régimen de alta luminosidad, es de reconocida importancia el conocimiento de las incertidumbres en las funciones de distribución de partones, especialmente en el caso del protón. La posibilidad de usar diferentes métodos directos en la medida de la densidad de gluones, permitiría el conocimiento de los errores teóricos y sistemáticos, así como elestablecimiento de test mas restrictivos en los llamados "ajustes globales" (Global fits) de las PDF's, en los cuales los procesos de dispersion profundamente inelástica (DIS) con protones juegan un papel esencial.

- Con este objetivo, hemos presentado una propuesta para investigar la densidad de gluones en el protón usando la HP de bottomonia en LHC, aportando la información más relevante para su desarrollo: se ha presentado las curvas y estadística para la familia Υ tomada en conjunto. Se ha considerado la posibilidad de aumentar la estadística, hasta un factor 10, introduciendo la condición $||y_\Upsilon| - |y_{jet}||$ <0.25.

- Para evaluar el impacto del k_T intrínseco en la topología de los eventos (con lo que se pierde la topologia ideal llamada "de retroceso" - back-to-back -), hemos estudiado, bajo diferentes condiciones (mecanismo de radiación inicial y, tambien, probando diferentes valores de $< k_T >$ con el mecanismo gaussiano de radiación), los momentos transversos de $\Upsilon(1S)$ versus el el jet procedente del otro gluón, mostrando que, incluso en el peor de los casos, este efecto no supone una pérdida dramática de estadística ($\simeq$ 40%) por sí mismo.

- Tras el estudio de las correlaciones azimutales del jet con respecto a $\Upsilon(1S)$, con el fin de ver si se puede discriminar esta topología de 180^0, teniendo en cuenta el efecto de k_T bajo las condiciones anteriores, podemos decir que esta condición parece adecuada, sin que suponga, de nuevo, una pérdida dramática de estadística.

- Profundizando y concretando más la propuesta, en primer lugar, y con el fin de incrementar el número de puntos experimentales en el intervalo total de "rapidez" (rapidity), 2.5 para LHC, reducimos los subintervalos de ésta a $y_0 = 0.2$. Después se hace un estudio de las PDF más relevantes a LO y NLO, así como una estimación de los efectos de detector, haciendonos una idea del número final de eventos esperados.

- Dadas las previstas tasas de producción de botomonio en el LHC, proponemos probar la forma de la densidad de gluones en el protón en el intervalo de valores de x: 2.1×10^{-3} hasta 1.2×10^{-2}, usando $x = \sqrt{\hat{s}/s}$ desde $p_T \simeq 15$ GeV hasta $p_T \simeq 85$ GeV.

- Hemos constatado que el poder de discriminación previsto con la estadística esperada, tras tres años de toma de datos a "baja" luminosidad en el LHC, debería ser suficiente para determinar la bondad de las diferentes PDF's. Hay que decir que hemos preferido ser conservadores en las estimaciones de las eficiencias de las medidas, y por tanto en el número esperado de eventos. No obstante concluimos que nuestra propuesta puede resultar útil en la medida de la densidad de gluones en el protón, tras unos pocos años de toma de datos en el LHC.

- Por otra parte, aunque la universalidad de los elementos de matriz de octete de color no está definitivamente establecida, se puede esperar razonablemente que los elementos de matriz obtenidos a través de la misma clase de proceso hadrónico pero a diferente escala de energia (HP en Tevatrón) son aplicables para el caso de LHC, tomando los mismos supuestos teóricos (masa del quark b, escala de factorización, etc.). Somos conscientes que esta propuesta requiere aún de mucho trabajo adicional, considerando pues esta propuesta como un primer paso en el estudio de su realización en el experimento ATLAS de LHC.

Appendix A

Generation, PYTHIA routines

In this section a general outlook about PYTHIA and JETSET routines, features and procedures in generating the processes of interest are shown. The reader must be warned that this discussion does not attempt to be a generation manual, but rather a guide about how the hadronic scenario has been reproduced from the available tools; further details can be found in references provided along this section.

Essentially what is done is to use available PYTHIA routines, modifying them in order to analyze bottomonia hadroproduction. Those changes were necessary since these resonances were not considered in the original software.

Organization

PYTHIA and JETSET routines [30] are inserted in a framework called CMZ [49] that allows through the Patchy language to control separately each feature of the process by means of the bunches of instructions so called "cards", each card is responsible of a particular aspect of the generation, physical constraints etc, and can be modified individually; a main card manages the others. Those programs are read and compiled in FORTRAN language. Follows, a brief list of the features for each card.

- *PYSIGH Routines*: These routines are available from PYTHIA, affording hundreds of subroutines (ISUB) each one specific for one physical process:$2 \to 1$, $2 \to 2$, $2 \to 3$, etc. Among these we shall focus on $2 \to 2$ processes and more specifically on:

  - Gluon fusion to charmonia: $gg \to J/\psi g$ (ISUB 86)
  - Gluon quark scattering to Higgs: $gq \to H_0 q$ (ISUB 112)
  - Quark scattering to Higgs $q\overline{q} \to H_0 g$ (ISUB 111)

  These subroutines have to be modified in order to reproduce the bottomonia hadroproduction, as explained later, at this moment it is enough to say that such routines carries the explicit calculation of the cross sections for the particular process.

- *UVAL Routine*: Among others functions, this routine has the control over the muon trigger, the rapidity cut, and the selection of the appropriate variables to fill the histograms (as p_T, angle, etc). In this routine is also implemented the Altarelli-Parisi evolution mechanism.

- *$USER-INIT$ Routine*: Its function, mainly, is to call the selected Pysigh routines. Here the size and dimension of the histograms is defined.

- *$FORCE-DECAYS$ Routine*: Switch on/off the decay channels of the J/ψ and Higgs. In this study only the muon decay channel is open, all others are switched off.

- *MAIN Routine*: It manages the others cards, compiling and calling them at the appropriate moment. But also drives the physical process, since here is where the features of the collision are fixed at will:

  - Beams and target particles: In this work either pp or $p\overline{p}$

- Center of Mass Energy (in GeV): We shall focus on TEVATRON and LHC energies.
- p_T cut for the process (through CKIN(3) master switch) defined in the rest frame of the hard interaction.
- Range of allowed pseudorapidities for partons (through CKIN(13,15) variables)
- Quark masses (in GeV) (QMASS variable), Higgs mass (HMASS) and $Q\overline{Q}$ mass (QQMAS): These master switches are very useful since it allows to change the particles under study redefining their masses and making some changes in the original PYTHIA routines, as it will be explained later.
- Initial and final state QED and QCD radiation: Master switches MSTP(61) and MSTP(71) allows to control those effects at will. Initial state radiation implies that each off two incoming partons has a non vanishing p_T when they interact. The hard scattering subsystem thus receives a net transverse boost, and is rotate with respect to the beam directions. In the process under study what typically happens is that one of the scattered partons receives an increased p_T while the p_T of the other is reduced. Since the initial-state radiation assigns space-like virtualities to the incoming partons the definition of x in terms of the energy fractions and in terms of momentum fractions no longer coincide, and so the interacting subsystem may receive a net longitudinal boost compared with the naïve expectations, as part of the parton shower machinery. Initial and Final State Radiation also give rise to additional jets. These features are treated more extensively in the Probe of the Gluon Density chapter.
- Switch on/off the primordial p_T distribution in hadrons: By means of the variable MSTP(91) is allowed to implement a p_T distribution following a Gaussian distribution, setting its

width through the variable PARP(91) and an upper cut-off through PARP(93).

- Choice of the Parton Distribution Function (PDF): Through the variable MSTP(52) it is possible to choice the PDF, either the internal from PYTHIA (in this version the CTEQ2L (LO) PDF) or from the external PDF library [50] CTEQ4L (LO), or many others PDFs available from this library package; the code that selects the PDF is inserted by means of the master switch MSTP(51).
- Choice of longitudinal fragmentation functions (MSTJ(11)): Can be selected following the Lund symmetric function, flavour dependent function or an hybrid scheme.
- Switch on/off Multiple interactions (MSTP(81))
- It has also control over Pile-up events, number of events to be processed, and from this routine it can be set the number of processes to be displayed in detail in order to analyze the chain of the jet production.

Appendix B

Statistical errors

In this appendix, we discuss the techniques used in computing the statistical errors in fitting NRQCD matrix elements at Tevatron. To this aim we employed the standard concepts of errors (as the differences between theoretical distributions -histograms- and the experimental points) and their propagation through theoretical expressions. It will be distinguished the case of CTEQ4L and the CTEQ2L one.

Setting the procedure

CTEQ4L

As it is explained in chapter 3, the whole histogram can be disentangled as

$$H = (CSM contribution)\ +\ b\ \times\ ([^3S_1]_{COM}\ contribution) \tag{B.1}$$

where b is the $(^3S_1)_8$ histogram fit factor, according to the explanation done in chapter 3 section 5.

$$H_k = c_k\ +\ b_k\ q_k \tag{B.2}$$

Keeping in mind that the error for each bin contribution is systematic since it comes from the generation, the statistical error of the

H_k arises from the b_k fit, then from Eq. (B.2) and according to error propagation

$$\begin{aligned} b_k &= \frac{H_k \; - \; c_k}{q_k} \\ \varepsilon(b_k)^2 &= \frac{\varepsilon(H_k)^2}{q_k^2} \end{aligned} \tag{B.3}$$

where $\varepsilon(H_k)$ is defined as

$$\varepsilon(H_k) \equiv \gamma_k \; H_k$$

where the index relates the error with its corresponding bin. Gamma is defined as the histogram error relative to the experimental point.

$$\gamma_k = \left| \frac{H_k \; - \; P^k_{exp}}{P^k_{exp}} \right|$$

On the other hand, if N is the number of bins that corresponds to the number of *experimental points one by one*, then the b factor

$$b \equiv \; \overline{b} = \frac{1}{N} \sum_{k=1}^{N} b_k \tag{B.4}$$

However, as in the χ^2 calculation case, there are cases where one experimental point corresponds to more than one bin (see Figure 3.2, chapter 3); in those situations, previously an average over those bins is performed.

From equation (B.4), the usual errors propagation yields

$$\varepsilon(\overline{b})^2 = \frac{1}{N^2} \sum_{k=1}^{N} \varepsilon(b_k)^2 \tag{B.5}$$

then, with the aid of the above equations, the error is found to be

$$\varepsilon(\overline{b})^2 = \frac{1}{N^2}\sum_{k}^{N} \frac{\left(\frac{H_k\ -\ P_{exp}^k}{P_{exp}^k}\right)^2 H_k^2}{q_k^2} \tag{B.6}$$

CTEQ2L

In this case the procedure is the same, but now we have to consider the $({}^1S_0)_8 + ({}^3P_J)_8$ contribution, that was quite small from the fit of the matrix element but not null. Therefore in fitting those histograms all contributions are considered

$$H_k = c_k\ +\ b_k\ q_k\ +\ a_k\ t_k \tag{B.7}$$

where the above-mentioned notation is followed: a_k stands for the $({}^1S_0)_8 + ({}^3P_J)_8$ histogram fit factor (see chapter 3). Hence, two free parameters are involved in the fit (i.e. a and b).

Now the process is split into two parts. First we focus on the region where the $({}^1S_0)_8 + ({}^3P_J)_8$ contribution is less important than the $({}^3S_1)_8$ contribution (i.e. the relative high and the high p_T region), say less than a 10% of the total rate (this constraint is verified checking over the corresponding bins). In this region (see Figure 3.1, chapter 3) the following approach is performed

$$H_k \simeq c_k\ +\ b_k\ q_k \tag{B.8}$$

then the error is computed as explained above. Notice that only the bins H_k are taken into account in this case in the region of interest.

Once this error is obtained (notice that now $b \pm \varepsilon(b)$ is assumed to be known), next step begins considering the low p_T region (where $({}^1S_0)_8 + ({}^3P_J)_8$ is important); in this region

$$a_k = \frac{H_k \ - \ c_k \ - \ b \, q_k}{t} \tag{B.9}$$

Hence making the same assumptions, error propagation yields as before

$$\varepsilon(a_k)^2 = \frac{1}{t_k^2} \, \varepsilon(H_k)^2 \ + \ \frac{q_k^2}{t_k^2} \, \varepsilon(b)^2 \tag{B.10}$$

where the error of H_k is obtained in the same way as above; the bins belonging to the region of interest are only considered. Finally the $\overline{a}$ error is obtained by means of

$$\varepsilon(\overline{a})^2 = \frac{1}{N^2} \sum_{k=1}^{N} \varepsilon(a_k)^2 \tag{B.11}$$

All these calculations were performed by means of an appropriate software.

Appendix C

Altarelli-Parisi evolution of PDFs

The main goal of this appendix is to analyze the difference between the $\Upsilon(nS)$ resonances (n = 1,2,3) production cross sections through both Color Singlet Model (CSM) and Color Octet Mechanism (COM) obtained by means of PYTHIA using the Parton Distribution Functions (PDFs) CTEQ4L and CTEQ2L; these PDFs follow a different behaviour. As pointed out in chapter 4, the ratios of the cross sections of the same process generated through both PDFs, without any kinematic cut, are $\sim 1.2 - 1.3$ (depending on what contribution is taken), as it can be seen in Table C.1.

Table C.1: Ratios of the cross sections from PYTHIA Generation, using CTEQ 4L and 2L PDFs.

$Channel$	$\frac{\sigma_{CTEQ4L}}{\sigma_{CTEQ2L}}$
gg_{CSM}	1.3
gg_{COM}	1.2

As an exercise, this factors are checked. AP Evolution equations are solved for each PDF and later the quotients are done. Such PDFs are parameterized by CTEQ Collaboration [51, 52]:

Developing the idea

The main idea is that, taking into account that the partonic cross section is proportional to $\alpha_s^3(Q^2) \times G(x,Q^2) \times G(x',Q^2)$, it can be calculated. Inserting the requirements of generation in PYTHIA machinery, the quotient is

$$\frac{\frac{d\sigma}{dp_t}|_{CTEQ4L}}{\frac{d\sigma}{dp_t}|_{CTEQ2L}} \simeq \frac{G^2(x,Q^2)_{4L}}{G^2(x,Q^2)_{2L}}$$

In order to explain the bias between these cross sections depending on the PDF choice, the partonic processes are analyzed in the framework of the different PDFs.

In the absence of any intrinsic k_t effects, we can write the triple differential cross section for the production process $pp{\rightarrow}\Upsilon X$ as

$$\frac{d^3\sigma}{dy_\Upsilon dy_X dp_T} = 2p_T \sum_{ab} x_a x_b f_{a/p}(x_a) f_{b/p}(x_b) \frac{d\hat{\sigma}}{d\hat{t}} \tag{C.1}$$

where $f_{a/p}(x_a)$, $f_{b/p}(x_b)$ denotes the parton-a density in the proton and the one for the parton-b, and

$$\frac{d\hat{\sigma}}{d\hat{t}} \equiv \frac{d\hat{\sigma}}{d\hat{t}}(ab{\rightarrow}\Upsilon c) = \frac{1}{16\pi\hat{s}^2} \overline{\sum} |\mathcal{A}(ab{\rightarrow}\Upsilon c)|^2 \tag{C.2}$$

stands for the partonic differential cross section that includes spin and colour summation. In the generation we set $y_0 < 0.4$ since Tevatron scenario were reproduced. Then, as explained in chapter 6, the Feynman x can be written as

$$x_a {\simeq} x_b = x, \text{ and}$$

$$x_a {\cdot} x_b = x^2 = \frac{\hat{s}}{s}$$

where

$$\hat{s} = Q^2 = \sqrt{P_T^2 + m^2_{(Q\overline{Q})}} + P_T$$

as usually is taken in PYHTIA generations.

The $gg \rightarrow \Upsilon g$ partonic process is considered here, so that the differential cross section can be disentangled as

$$\frac{d\sigma}{dp_t}|_{ggTOTAL} = \frac{d\sigma}{dp_t}|_{ggCSM} + \frac{d\sigma}{dp_t}|_{ggCOM} \tag{C.3}$$

integrating over all rapidities, and taking into account the form of the squared amplitudes the above contributions can be factorized as

$$\frac{d\sigma}{dp_t}|_{ggCSM} = K_{CSM}\ \alpha_s^3(Q^2)\ |R(0)|^2\ x^2\ G(x,Q^2)^2\ f_1(\hat{s},\hat{t},\hat{u},M) \tag{C.4}$$

where K_{CSM} stands for a numerical factor, $G(x,Q^2)$ is the gluon density in the proton, $f_1(\hat{s},\hat{t},\hat{u},M)$ is the kinematic part in terms of the Mandelstam variables, and $|R(0)|$ is the Υ squared wave function at the origin (see chapter 3). The second term in the sum can be expressed as

$$\frac{d\sigma}{dp_t}|_{ggCOM} = K_{COM}\ \alpha_s^3(Q^2)\ < O_8 >\ x^2\ G(x,Q^2)^2\ f_2(\hat{s},\hat{t},\hat{u},M) \tag{C.5}$$

again symbols mean the same, but corresponding to the COM contribution. $< O_8 >$ stands for the NRQCD matrix element.

Adding these two contributions, the whole contribution can be written as

$$\frac{d\sigma}{dp_t}|_{ggTOTAL} = \alpha_s^3(Q^2)\ x^2\ G(x,Q^2)^2 \tag{C.6}$$

$$\times\Big(\ K_{COM}\ f_2(\hat{s},\hat{t},\hat{u},M)\ < O_8 >\ +K_{CSM}\ f_1(\hat{s},\hat{t},\hat{u},M)\ |R(0)|^2\ \Big)$$

Since the kinematic requirements and matrix elements are set to be the same in both generations with CTEQ4L an CTEQ2L, then if the ratio between both differential cross sections are done one obtains

$$\frac{\frac{d\sigma}{dp_t}\big|^{4L}_{gg}}{\frac{d\sigma}{dp_t}\big|^{2L}_{gg}} = \frac{\alpha_s^3(Q^2)\big|^{4L}\ x^2G(x,Q^2)^2\big|^{4L}}{\alpha_s^3(Q^2)\big|^{2L}\ x^2G(x,Q^2)^2\big|^{2L}} \tag{C.7}$$

it must be observed that $\alpha_s(Q^2)$ is taken to be different in both PDFs, as we shall see.

The calculation is performed along the range of the Tevatron data for Υ production, viewing in detail the relative low p_T region since it gives the main contribution to the total cross section.

Getting ready the calculation

The CTEQ PDFs take the form:
gluon function

$$G(x,Q^2) = a_0\ x^{a_1}\ (1-x)^{a_2}\ (1+a_3x^{a_4}) \tag{C.8}$$

quark i functions $i = u_v, d_v, s\ ((\overline{s}),\ ((\overline{d}+\overline{u})/2)$

$$q(x,Q^2) = a_0^i\ x^{a_1^i}\ (1-x)^{a_2^i}\ (1+a_3^ix^{a_4^i}) \tag{C.9}$$

the $(\overline{d}-\overline{u})$ combination

$$(\overline{d}-\overline{u}) = a_0^-\ x^{a_1^-}\ (1-x)^{a_2^-}\ (1+a_3^-\sqrt{x}+a_4^-x) \tag{C.10}$$

where the CTEQ parameterization will followed.

The parameters are taken at $Q_0^2 = 2.56\,GeV^2$, therefore the Altarelli-Parisi evolution must be performed up to the Q^2 of interest, using the following expression [53, 54]:

$$Q^2 \frac{d}{dQ^2} G(x,Q^2) = \frac{\alpha_s(Q^2)}{2\pi} \int_x^1 \frac{dy}{y} (P_{Gq}(x/y)\, q(y,Q^2) + P_{GG}(x/y)\, G(y,Q^2)) \tag{C.11}$$

The first and the second term in the sum will be denoted as quark integral and gluon integral, respectively. $P_{Gq}(x)$ and $P_{GG}(x)$ are the probability functions that a quark radiates a gluon with a fraction x of the original and a gluon splits into two gluons, respectively.

$$P_{GG}(x/y) = 6 \left[\frac{\frac{x}{y}}{(1-\frac{x}{y})_+} + \frac{1-\frac{x}{y}}{\frac{x}{y}} + \frac{x}{y}(1-\frac{x}{y}) \right] + \frac{23}{6}\, \delta(1-\frac{x}{y}) \tag{C.12}$$

where the factor 23/6 is obtained for a number of flavours $N_f = 5$. Subindex + in the denominator of the first sum term indicates that the divergence in $\frac{x}{y} = 1$ disappears by means of the "+ prescription":

$$\int_0^1 dz\ f(z)\ [g(z)]_+ = \int_0^1 dz\ [f(z) - f(1)]\ g(z) \tag{C.13}$$

Making use of the identity $P_{Gq}(z) = P_{qq}(1-z)$ [54], where P_{qq} stands for the probability functions of the splitting of a quark.

$$P_{qq}(z) = C_F \left[\frac{1+z^2}{1-z} \right] \tag{C.14}$$

with $C_F = \frac{N^2-1}{2N}$. Thereby the above identity yields:

$$P_{Gq}(x/y) = \frac{8}{6} \left[\frac{x}{y} - \frac{2}{x}(x-y) \right] \tag{C.15}$$

The P_{Gq} term is included because the x values are moderate in the p_T region most significant for the cross sections, as we shall see, and hence there is a significant contribution from quarks distributions $q(x,Q^2)$.

Throughout of the integration over "y" values $x_0 \equiv x$ is fixed at the Q^2 of interest (notice that in our choice of Q^2 it is not independent from x, as discussed in the previous section), $G(y,Q^2) \equiv G(y,Q_0^2)$, idem $q(y,Q^2) \equiv q(y,Q_0^2)$ are taken, according to the CTEQ parameterization.

gluon integral calculation

First we shall focus on the second integral from the evolution equation (C.11), that corresponds to the $G(y,Q^2)$ contribution.

$$I = \int_x^1 \frac{dy}{y}\ P_{GG}(x/y)\ G(y,Q^2) \tag{C.16}$$

Taking the Eq. (C.12) the later expression can be disentangled as $I = I_a + I_b + I_c + I_d$, where:

$$I_a = 6\int_x^1 \frac{dy}{y}\ \left[\frac{\frac{x}{y}}{(1-\frac{x}{y})_+}\right]\ G(y,Q^2) \tag{C.17}$$

$$I_b = 6\int_x^1 \frac{dy}{y}\left[\frac{1-\frac{x}{y}}{\frac{x}{y}}\right]\ G(y,Q^2) \tag{C.18}$$

$$I_c = 6\int_x^1 \frac{dy}{y}\left(\frac{x}{y}\right)\left(1-\frac{x}{y}\right)G(y,Q^2) \tag{C.19}$$

$$I_d = \frac{23}{6}\int_x^1 \frac{dy}{y}\ G(y,Q^2)\ \delta(1-\frac{x}{y}) \tag{C.20}$$

Now a separated calculation can be performed

$\underline{I_d,\ I_b,\ I_c}$:

If one sets $z = x/y$, a direct calculations gives

$$I_d = \frac{23}{6}\ G(x,Q^2) \tag{C.21}$$

The separation of I_b and I_c yields:

$$I_b = \frac{6}{x}\int_x^1 dy\ G(y,Q^2) - 6\int_x^1 dy\ \frac{G(y,Q^2)}{y} \tag{C.22}$$

$$I_c = 6x\int_x^1 dy\frac{G(y,Q^2)}{y^2} - 6x^2\int_x^1 dy\frac{G(y,Q^2)}{y^3} \tag{C.23}$$

These integrals can be solved, taking into account the $G(y,Q^2)$ form, separating them in a sum of Euler Beta Functions and their complementary functions, as we shall see.

$\underline{I_a}$:

Making the change $z = x/y$ and using Eq. (C.17):

$$\frac{I_a}{6} = \int_x^1 \frac{G(\frac{x}{z},Q^2) - G(x,Q^2)}{1-z}dz \equiv \int_x^1 F(z)dz \tag{C.24}$$

In solving this integral, numerical methods are required (Simpson's method for instance), so that we will need the integrand limits; taking those limits from Eq. (C.8)

$$\begin{aligned}\lim_{z\to x} F(z) &= \frac{-G(x,Q^2)}{1-x}\\ \lim_{z\to 1} F(z) &= -G(x,Q^2)\Big[a_4\Big(\frac{1}{1+a_3x^{a_4}} - 1\Big) + a_2\frac{x}{1-x} - a_1\Big]\end{aligned} \tag{C.25}$$

therefore the integral is:

$$\frac{I_a}{6} = \int_{x+\epsilon}^{1-\epsilon} dz\ \frac{a_0\ x^{a_1}\ z^{-(a_1+a_2+a_4)}\ (z-x)^{a_2}\ (z^{a_4}+a_3x^{a_4}) - G(x,Q^2)}{1-z} \tag{C.26}$$

here, ϵ indicates the width of the interval. The integral runs from the interval after z=x up to before the z=1 interval. The solution of the whole integral is reached adding the values of the limits (C.25) to the later result, according to the Simpson's Rule.

quark integral calculation

To calculate this contribution from $q(y,Q^2)$, first integral from Eq. (C.11) are considered:

$$II = \int_x^1 \frac{dy}{y}\ P_{Gq}(x/y)\ q(y,Q^2) \tag{C.27}$$

By inserting Eq. (C.15) in the above expression one obtains directly:

$$II = C_F x \int_x^1 \frac{dy}{y^2} q(y,Q^2) - 2C_F \int_x^1 \frac{dy}{y} q(y,Q^2) + \frac{2C_F}{x} \int_x^1 dy\ q(y,Q^2) \tag{C.28}$$

Taking into account the form of the $q(y,Q^2)$ functions according to Eqs. (C.9) and (C.10), integrals of the following kind are considered

$$I_q^i = a_0 \int_x^1 y^{a_1 - i}\ f(a_2,a_3,a_4,y)\ dy\ [i=0,1,2] \tag{C.29}$$

the form of the $f(a_2,a_3,a_4,y)$ functions are the same for each quark contributions excepting for $(\overline{d} - \overline{u})$.

Hence we have

$$II = C_F\ a_0 \Big[\ \frac{2}{x} I_q^0\ -\ 2I_q^1\ +\ xI_q^2\ \Big] \tag{C.30}$$

where $q = u_v, d_v, s, (\overline{d} + \overline{u}), (\overline{d} - \overline{u})$. In each case they will be solved in an analytical way.

The numerical integration of Eq. (C.26) is performed according to the Simpson's Method [55], taking 1000 integration intervals from x up to 1, where preliminary test indicates that the result does not change until the 4-th decimal. this method is checked crossing the results with another methods as the rectangles method and others. the results are consistent, as it is expectable since both $G(x,Q^2)$ and $q(x,Q^2)$ are smooth functions in the range of interest.

Towards an analytical solution of the integrals of the form I_b, I_c and II, Euler Beta Functions, $B(p,q)$, and their complementary functions, $B_x(p,q)$, are used:

Quark and gluon integrals, once disentangled and arranged can be presented in the form

$$\begin{aligned}
I &= K \int_x^1 y^{p-1}(1-y)^{q-1} dy \\
I &= K\ (B(p,q) - B_x(p,q)) \\
I &= K \left[\frac{\Gamma(p)\,\Gamma(q)}{\Gamma(p+q)} - \frac{x^p}{p}\, F(p, 1-q, p+1; x) \right] \\
F(a,b,c;x) &= \frac{\Gamma(c)}{\Gamma(a)\,\Gamma(b)} \sum_{n=0}^{\infty} \frac{\Gamma(a+n)\,\Gamma(b+n)}{\Gamma(c+n)} \frac{x^n}{n!}
\end{aligned} \tag{C.31}$$

where K is a factor, and $F(p, 1-q, p+1; x)$ is the Hypergeometric Function [56]; Gamma function values are taken from the tables [57], in finding intermediate values from these tables, linear interpolation were carried out. It must be stressed that, when computing the Hypergeometric Function, one has to be careful about of its convergence.

Now using Eqs. (C.31), and after several manipulations, explicit form for each contribution can be done in a compact form, as can be seen just below: [1]

---

[1] $B(p,q) - B_x(p,q)$ can also be arranged as $B_{1-x}(q,p)$.

- gluon integral

$$
\begin{aligned}
I_g \;&=\; I_a + \frac{23}{6}\, G(x,Q^2) \;+\; 6\; a_0 \Big[\sum_{k=1}^{4} (-1)^{k-4} x^{3-k} \;\cdot \\
\cdot \;&\Big(\big(\; B(a_1+k-3, a_2+1) - B_x(a_1+k-3, a_2+1)\;\big) \\
+ \;& a_3 \;\big(\; B(a_1+a_4+k-3, a_2+1) - B_x(a_1+a_4+k-3, a_2+1)\;\big)\Big)\Big]
\end{aligned}
\tag{C.32}
$$

- quark i functions $i = u_v, d_v, s\ (\overline{s}),\ (\overline{d}+\overline{u})/2)$

$$
\begin{aligned}
I_q^i \;&=\; C_F\; a_0^i \Big[\sum_{k=1}^{3} (-1)^{k-2} \;(\; 1+\Theta(2-k)\;)\; x^{k-1} \;\cdot \\
\cdot \;&\Big(\big(\; B(a_1^i+2-k, a_2^i+1) - B_x(a_1^i+2-k, a_2^i+1)\;\big) \\
+ \;& a_3^i \;\big(\; B(a_1^i+a_4^i+2-k, a_2^i+1) - B_x(a_1^i+a_4^i+2-k, a_2^i+1)\;\big)\Big)\Big]
\end{aligned}
\tag{C.33}
$$

where $\Theta(1-k)$ is the step function, defined as: $1\ if\ 2-k \geq 0\ ;\ 0$ otherwise.

- $(\overline{d}-\overline{u})$ combination

$$
\begin{aligned}
I_q^- \;&=\; C_F\; a_0^- \Big[\sum_{k=1}^{3} (-1)^{k-1} \;(\; 1+\Theta(2-k)\;)\; x^{k-2} \;\cdot \\
\cdot \;&\Big(\big(\; B(a_1^-+2-k, a_2^-+1) - B_x(a_1^-+2-k, a_2^-+1)\;\big) \\
+ \;& a_3^- \;\big(\; B(a_1^-+5/2-k, a_2^-+1) - B_x(a_1^-+5/2-k, a_2^-+1)\;\big) \\
+ \;& a_4^- \;\big(\; B(a_1^-+3-k, a_2^-+1) - B_x(a_1^-+3-k, a_2^-+1)\;\big)\Big)\Big]
\end{aligned}
\tag{C.34}
$$

These expressions once developed can be reduced using recurrence formulas of the Gamma functions and the Hypergeometric functions.

Calculations were checked in solving at the same time numerically these integrals, that allows to fix that, including up to the quadratic term in the Confluent Hypergeometric Function, numerical and analytical results only differ in a few percent. The values of the parameters of the PDF are taken from [51, 52].

Q^2 evolution

The CTEQ collaboration affords the parameters at $Q_0^2 = 2.56\ GeV^2$, and the Λ_5 values (which corresponds to a number of flavours $N_f = 5$), setting $\alpha_s(Q_0^2)$ to be 0.376 and 0.339, for CTEQ 4L and 2L PDFs respectively (at LO). Those values can be obtained from

$$\alpha_s(Q_0^2) = \frac{2\pi}{-\beta_1\ ln\left(\frac{Q_0^2}{\Lambda^2}\right)} \tag{C.35}$$

where QCD β_1 is fixed according to [58, 59]

$$\beta_1 = \frac{2N_f - 11N_c}{6}$$

Once the integration over "y" in Eqs. (C-16) and (C-27) is performed, the evolution equation can be written as

$$Q^2 \frac{d}{dQ^2} G(x, Q^2) = \frac{\alpha_s(Q^2)}{2\pi} I_{kL}(k = 2, 4) \tag{C.36}$$

Where I_{kL} are the integral values (adding all contributions) at each p_T value and for each PDF (k=2,4) case. Now integration over Q^2 is performed in the following way:

Taking the well known LO evolution equation of $\alpha_s(Q^2)$

$$\alpha_s(Q'^2) = \frac{\alpha_s(Q_0^2)}{1 - \frac{\beta_1 \alpha_s(Q_0^2)}{2\pi} ln\left(\frac{Q'^2}{Q_0^2}\right)} \tag{C.37}$$

where primes are raised in order to distinguish. Using the equations (C.37-39) together with β_1, one obtains by means of a straightforward integration over the interval of interest, i.e. from Q_0^2 up to each Q^2 value:

$$G(x, Q^2) = G(x, Q_0^2) + \frac{6I_{kL}}{23}\Big[ln(1 + \frac{23\alpha_s(Q_0^2)}{12\pi} ln\Big(\frac{Q'^2}{Q_0^2}\Big))\Big](k = 2, 4) \tag{C.38}$$

Once each pair $G(x, Q^2)$ is obtained, the quotient between the squared values can be calculated. In Figure C.1 the results are summarized for p_T values at the Tevatron. Figure C.2 displays gluon densities for each PDF.

If we take the values of these quotients, R_i, in all the p_T range, weighing them with their corresponding p_T intervals, Δp_T, we found the mean value:

$$\overline{R} \;=\; \frac{\sum_i R_i\ \Delta p_T^i}{\sum_i \Delta p_T^i} = 1.337 \tag{C.39}$$

In agreement with the values afforded by PYTHIA.

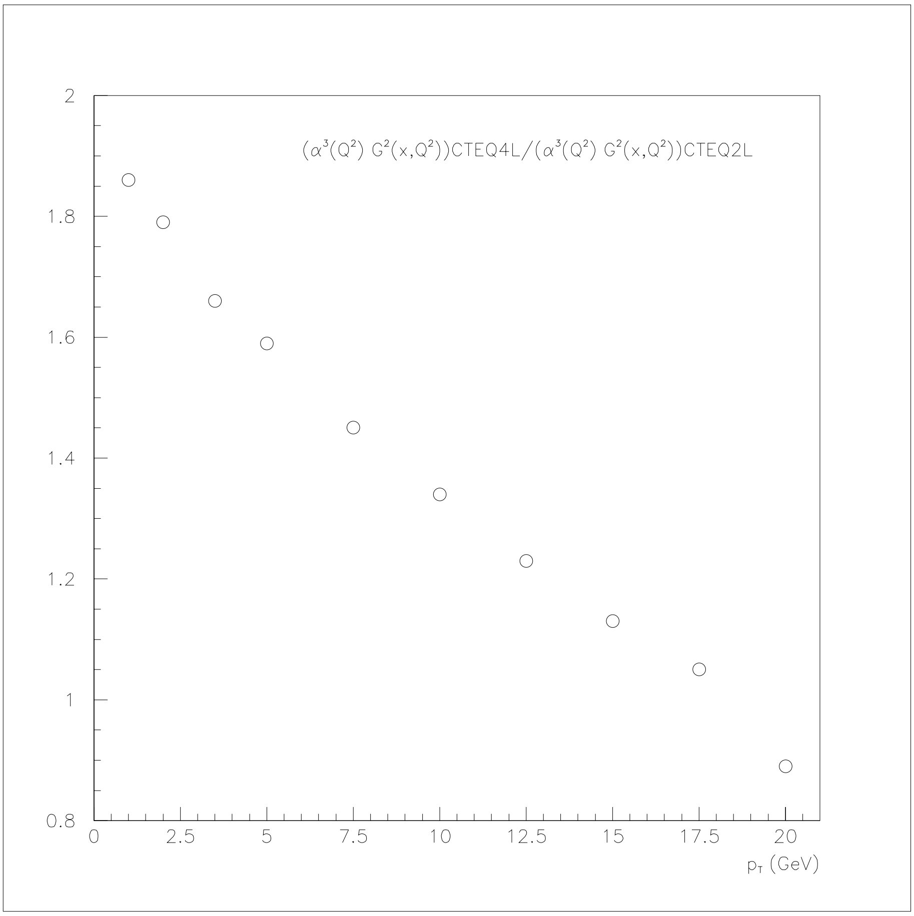

Figure C.1: Quotients vs. P_t. Weighed factor is 1.3 in the range of interest, in agreement with the values obtained in PYTHIA

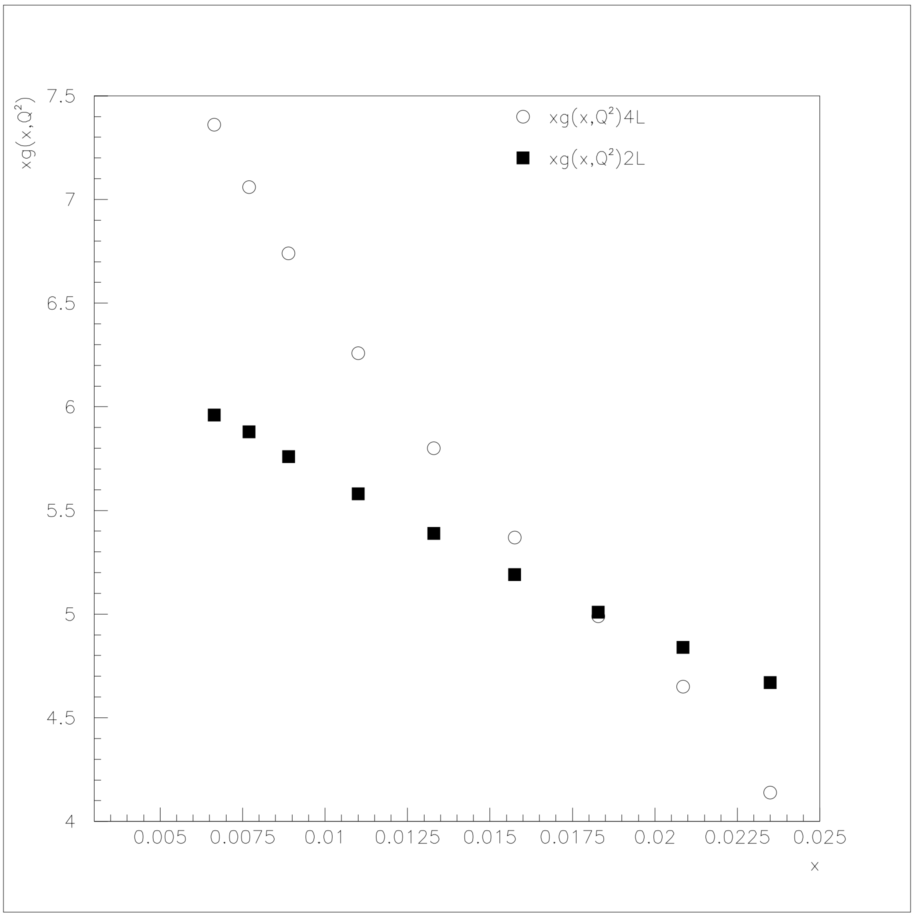

Figure C.2: Gluon densities vs. x.

Bibliography

[1] M. Krämer, hep-ph/0010137.

[2] ATLAS detector and physics performance Technical Design Report, CERN/LHCC/99-15.

[3] ATLAS *Technical proposal.* **CERN/LHCC 94-43.**

[4] ATLAS Collaboration *Tile Calorimeter Technical Design Report.***CERN/LHCC/96-42.**

[5] M. Dittmar *et al.* Phys. Rev. **D56**, 7284 (1997).

[6] E. Braaten and J. Lee, hep-ph/0012244.

[7] G. Feild *et al.*, **CDF note 5027.**

[8] D.E. Groom *et al.*, Particle Data Group, EPJ **C15** (2000) 1.

[9] CDF Collaboration, **FERMILAB-PUB-99/301-E.**

[10] E. Braaten *et al.* preprint UTPT-98-18 (1998).

[11] M.A. Sanchis-Lozano, Nucl. Phys. **B440** (1995) 251.

[12] B. Grinstein hep-ph/9811264, and references therein.

[13] E. Braaten, S. Fleming and T. Yuan, hep-ph/9602374.

[14] G. Schuler hep-ph/9504242 **CERN-TH/95-75**, and references therein.

[15] E. Braaten and T. Yuan, Phys. Rev. **D50**, 3176 (1994).

[16] R. Gavai *et al.* hep-ph/9502270 **CERN-TH.7526/94**, and references therein.

[17] E. Braaten and S. Fleming, Phys. Rev. Lett. **74** (1995) 3327

[18] G.T. Bodwin, E. Braaten, G.P. Lepage, Phys. Rev. **D51** (1995) 1125.

[19] E. Braaten hep-ph/9702225 and references therein.

[20] M. Beneke SLAC-PUB-7173 (May 1996), hep-ph/9605462 and references therein.

[21] M. Neubert, hep-ph/9604412 **CERN-TH/96-55**, and references therein.

[22] F. Bertó, J.L. Domenech-Garret, and M.A. Sanchis-Lozano, Nuov. Cim. **A112**, 1181 (1999).

[23] G.P. Lepage *et al.* Phys. Rev. **D46** (1992) 4052

[24] S. Fleming *et al.* hep-ph/0012062.

[25] P. Cho and A.K. Leibovich, Phys. Rev. **D53** (1996) 150.

[26] G. Schuler, Int. J. Mod. Phys. **A12** (1997) 3951.

[27] E.J. Eichten and C. Quigg, Phys. Rev. **D52** (1995) 1726.

[28] B. Cano-Coloma and M.A. Sanchis-Lozano, Nucl. Phys. **B508** (1997) 753, hep-ph/9706270.

[29] B.A. Kniehl and G. Kramer,**DESY** 98-023, hep-ph/9803256.

[30] T.Sjöstrand *PYTHIA 5.7 and JETSET 7.4* **CERN-TH. 7112.**

[31] T. Sjöstrand, Phys. Lett. **B157** (1985), 321.

[32] K. Sridhar, A.D. Martin, W.J. Stirling, Phys. Lett. **B438** (1998) 211.

[33] M.A. Sanchis-Lozano, Nucl. Phys. **B86** (Proc. Suppl.), 543, 2000, hep-ph/9907497.

[34] M.A. Sanchis-Lozano, Nucl. Phys. **B75B** (Proc. Suppl.), 191,1999, hep-ph/9810547.

[35] R. Baier and R. R*ü*ckl Z. Phys. **C19**,251 (1983).

[36] P. Cho and A.K. Leibovich, Phys. Rev. **D53** (1996) 6203.

[37] E. Braaten, S. Fleming and A. Leibovich, hep-ph/0008091.

[38] J.L. Domenech and M.A. Sanchis-Lozano, Phys. Lett. **B476** (2000) 65.

[39] G. Schuler and R Vogt, hep-ph/9606410.

[40] M.A. Sanchis-Lozano, Nucl. Phys. B (Proc. Suppl.) 86 (2000) 543 (hep-ph/99707497).

[41] M. Beneke and M. Krämer, Phys. Rev. **D55** (1997) 5269.

[42] A. Tkabladze, Phys. Lett. **B462** (1999) 319.

[43] S. Baranov, Nucl. Phys. **B86** (Proc. Suppl.), 220, (2001)

[44] J.L. Domenech-Garret and M.A. Sanchis-Lozano, hep-ph/0012296. Nucl. Phys. **B-601**,395 (2001).

[45] H1 Collaboration, Nucl. Phys. **B545** (1999) 21.

[46] *B* physics working group meetings of the ATLAS collaboration held at CERN in October, 2000 and February, 2001. Transparencies available under request to the authors.

[47] S. Frixione et al., to appear in the Proceedings of the UK Phenomenology Workshop on Heavy Flavour and CP Violation, Durham, 17-22 September 2000 (to be published in *Phys. Lett.* **G**).

[48] http://www-spires.dur.ac.uk/HEPDATA/

[49] *CERN Computer Program Library* available at www.cern.ch

[50] H. Plothow-Besch/CERN-PPE, PDFLIB: Nucleon, Pion and Photon Parton Density Functions Users manual version 7.08 **W5051**.

[51] CTEQ Collaboration *Phys. Rev.* **D51** *(1995) 4763*, hep-ph/9410404.

[52] CTEQ Collaboration *Phys. Rev.* **D55** *(1997) 1280*, hep-ph/9606399.

[53] G. Altarelli and G. Parisi, Nucl.Phys. **B126** (1977),298.

[54] A.Pich hep-ph/9505231.

[55] N. Bakhvalov *Métodos Numericos (Ed. Paraninfo, 1980)*

[56] I.S.Gradstein and I.M. Ryzhick,*Tables of integrals, series, and products (Academic Press, 1980).*

[57] M. Abramowitz , I. A. Stegun, *Handbook of mathematical functions (Ed. Dover P. 1972).*

[58] D.J.Gross and F.Wilczeck, Phys.Rev.Lett. 30(1973),1343.

[59] G. Sterman *et al.* (CTEQ Collaboration) *Handbook of perturbative QCD version 1.0* available at CTEQ web-page.

List of Figures

List of Tables